Report

Structural analysis and modelling of a reinforced concrete bridge based on full scale data

Þórunn Vala Jónasdóttir
Jónas Þór Snæbjörnsson

Department of Engineering, Reykjavik University

September, 2021

Disclaimer

The authors of the present report are responsible for its contents. The report and its findings should not be regarded as to reflect the Icelandic Road Authority's guidelines or policy, nor that of the respective author's institutions.

Preface

This report illustrates work done in connection with the research project "Structural analysis and modelling of a reinforced concrete bridge based on full scale data" that received funding from the Research fund of the Icelandic Road and Coastal Administration (IRCA) (grant no. 1800-788), which is gratefully acknowledged.

The preparatory work performed for this project was done in 2019, when the authors participated in a full-scale structural testing program at the old bridge over the Steinavötn river in south-east Iceland, organized by IRCA.

This report utilizes data gathered by the authors and supporting staff during the structural test campaigns in 2019. The analysis of the Steinavötn Bridge presented in this report were all performed by the authors: Þórunn Vala Jónasdóttir a master student at the Technical University of Denmark (DTU) and research assistant at Reykjavik University (RU) and Professor Jónas Þór Snæbjörnsson at RU.

The accelerometers used by RU-staff for the full-scale measurements were provided by Símon Ólafsson at the Earthquake Engineering Research Centre at the University of Iceland.

The velocity measurements on the ground near the bridge were done by Thomas J. Kennedy a visiting master student at the University of Iceland (UI) from Virginia Polytechnic Institute and State University, USA, in cooperation with Dr. Benedikt Halldorsson, at UI. The equipment used, was borrowed from LOKI, a portable seismic instrument bank operated by the Icelandic Meteorological Institute.

Professor Rune Brincker from the Department of Civil Engineering at DTU provided a Matlab toolbox for data analysis, in addition to insightful advice and access to the ARTeMIS software through his connection with Palle Andersen at Structural Vibration Solutions A/S.

Furthermore, Guðmundur Valur Guðmundsson, Ólafur Sveinn Haraldsson and Einar Óskarsson, staff members of IRCA have provided various drawings, photos and information related to the bridge structure and the full-scale experiments.

This work has also been published as a master thesis at DTU [1].

Abstract

This report evolves around structural modelling and analysis of full-scale monitoring data from an old single lane multi-span bridge over Steinavötn river in south-east Iceland. The bridge has now been demolished, but before its removal, the bridge was used as a full-scale test lab for dynamic and static experiments over a period of few months in the summer of 2019. During which period various data were sampled.

The purpose of the project is to study the structural characteristics and dynamic behaviour of a concrete bridge, using readily available analysis and modelling techniques. The objective is partly to improve the understanding of the bridge properties required for simulating the behaviour of concrete bridges in order to provide reliable estimates of response to various loading processes.

The bridge structure is described, the experiments performed introduced and the available data is presented. Special emphasis is placed on the acceleration response data gathered by RU-staff and the author. The project involves analysis of selected monitoring data from the full-scale tests, operational modal analysis of recorded ambient acceleration data using frequency domain methods and finite element-based modelling of the bridge structure. Two OMA tools are used, on one hand the ARTeMIS software and on the other MATLAB based frequency domain decomposition (FDD) toolbox provide by Professor Rune Brincker at DTU.

It is found that based on low amplitude ambient vibration data, the first four modes can be reliably estimated in terms of natural frequency and critical damping ratio, but the higher modes are more uncertain, and their identifiability varies depending on the dataset used. The lowest eigenfrequency of the bridge is found to be 5.7 Hz with a damping ratio of about 1% of critical. For the low amplitude ambient excitation analysed, the basic damping in the bridge is found to be between 1 and 2 percent for most of the modes identified.

For the finite element modelling of the bridge both a Beam-element model and a Shell element model is made. It is found that both models represent the measured data fairly well, as long as the material properties and especially the boundary conditions are properly defined. The Shell-element model is believed to be a more accurate representation of the structure as it better simulates the 3 dimensional properties of the bridge, especially the torsional influence on the higher modes of vibration. But both model types can be used to interpret and simulate the eigen vibrations, as well as static and dynamic response, at least for the lower modes of vibration.

Contents

List of Figures

List of Tables

1 Introduction

Traditionally various simplifications are routinely applied during the design and analysis of structures, when transferring theories to practice. Modern structural analysis computer software can provide probable structural response to a range of design loads, making it possible to study various reliable design alternatives. To verify and validate the applied analytical models and determine the actual load effect, field measurements are of key importance.

This report evolves around structural modelling and analysis of full-scale monitoring data, exploring available analysis and modelling techniques. The purpose of the project is to study the structural characteristics and dynamic behaviour of a concrete bridge. The case to be studied is the old bridge over Steinavötn river, in south-east Iceland, that has now been demolished. Before the bridge was removed in the fall of 2019, it was used as a full-scale lab for dynamic and static experiments. Finite element based modelling of the bridge structure and operational modal analysis of ambient acceleration data recorded on the bridge, comprise the core of this study. The objective is partly to improve the understanding of the required bridge properties to be able to better simulate the behaviour of concrete bridges to provide reliable estimates of response to various loading processes.

When the project application was written, the intention was to develop both linear and non-linear models of the bridge. Furthermore the plan was to consider not only data gathered by RU, but also data from other participants in the structural testing, such as the strain data collected by the OSMOS company. However, as the project was not fully funded and no additional data made available, the original plans changed and the focus has been on utilizing the data gathered by RU in connection with linear FE modelling of the bridge using SAP2000 to produce a 2D beam-element model and a 3D shell-element model. Non-linear simulation of the ultimate shear strength test and analysis of data from other participants awaits the next project.

1.1 The Steinavötn Bridge

The focus of this study is the old bridge over Steinavötn, shown in Figure 1.1 and Figure 1.2 which was a single lane, reinforced-concrete beam bridge built in 1964. The bridge was 102 m long and crossed the river Steinavötn, a glacial river in the South- East part of Iceland, see Figure 1.3. The river flows from Brókarjökull, a glacier tongue which is part of the largest glacier in Iceland, Vatnajökull, that has a catchment area of 150 km2.

The bridge is founded on a thick layer of sand and gravel which have been carried towards the coastal line by the Steinvötn river over the past thousands of years or since the last glacial age. The bridge surroundings and its foundation are described and discussed further in Chapter 2.

Figure 1.1: The Steinavötn bridge in July 2019, view from southeast.

Figure 1.2: The Steinavötn bridge in August 2019, view from southeast.

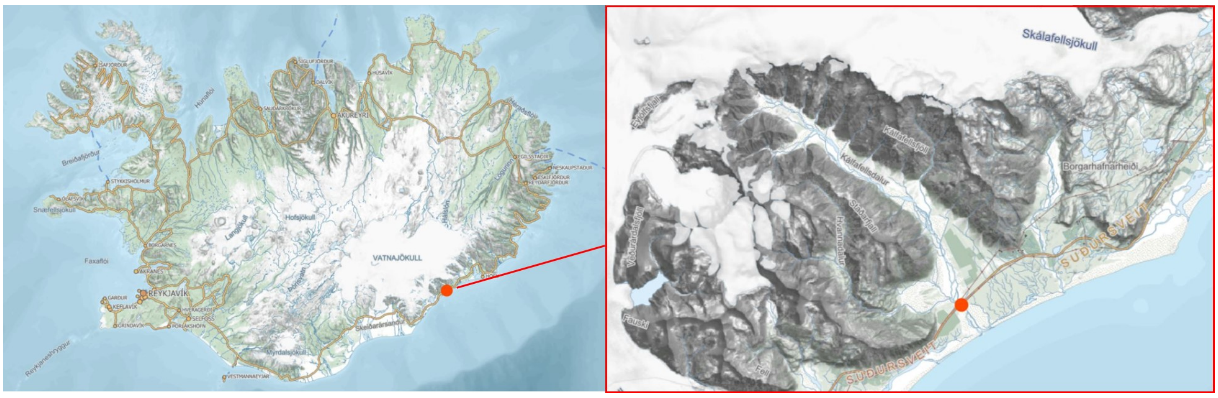

Figure 1.3: Location of the bridge, ca. 400 km from Reykjavik. (Loftmyndir ehf, 2021).

As can be seen in Figure 1.4, the old bridge at Steinavötn, was supported by five pillars and two end supports, dividing the bridge into six continuous spans. All the pillars are founded on wooden piles (8" in diameter), that were driven 5 m into the gravel. The structural system of the bridge can be reviewed through the original design drawings included in Appendix A.

In September 2017, the bridge was damaged during a flood caused by heavy rain in addition with the seasonal ablation. During the flood one of the piers was affected by scouring (see the circled pier in Figure 1.4), which caused it to tilt and subside which resulted in plastic hinges to form at the two adjacent piers, nr. 1 and 3 from west.

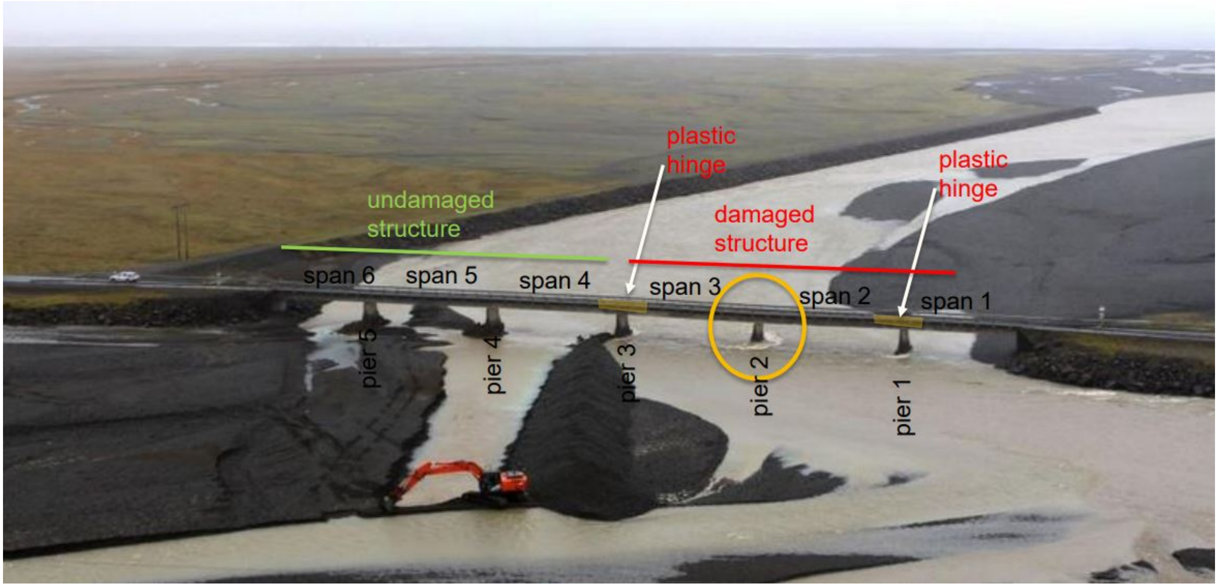

Figure 1.4: The identified damage of the Steinavötn bridge in 2017, view from north (IRCA, 2019).

Due to the observed damage, the bridge was considered unsafe and was consequently closed for traffic. However, the Steinavötn bridge is part of the national highway system which circles the country and an important route of transport to the East-fjords from the capital, Reykjavik, in the south-west of Iceland. Therefore a temporary bridge was built only one week later, right next to the old one. This temporary bridge was in operation until late 2020 when a new bridge was opened for traffic.

1.2 Scope and project formulation

As stated in the previous section, the project involves an analysis of an old single lane multi-span reinforced concrete bridge in Iceland, that was damaged in a flooding event in September 2017 and later demolished in September 2019. Before it was demolished, a full-scale structural testing project was initiated and undertaken in the summer of 2019, by the author of this thesis and staff from Reykjavik University. Various data were sampled during these experiments that have not been analysed or published until now. The project involves analysis of selected monitoring data from the full scale tests, system identification using operational modal analysis and structural FE modelling.

The objectives of the project are to:

- Describe the bridge structure, the experiments, and available data.
- Study the dynamic characteristics of the bridge based on recorded ambient acceleration data using the FDD method.
- Create a finite element model of the bridge that represents the measured data and can be used to interpret and simulate eigen vibrations, as well as static and dynamic response.

The aim is to answer the following questions:

- What are the eigenfrequencies and critical damping ratios for a reinforced concrete bridge of this type?
- How well can finite element models reflect those dynamic properties?
- Is there a difference in performance between a shell element model and beam element model?

1.3 The structure of the report

The report is divided into five main chapters, in addition to references and appendixes related to the study. The subjects covered in each chapter are clarified as follows.

The first chapter introduces the project along with its aim, objective and outlines the organization of the report.

Chapter two addresses bridge monitoring in general and gives an overview of the Steinavötn Bridge structural monitoring and the recorded data. It introduces the bridge and the installed monitoring system. Overview of the sampled data is given along with preliminary processing of the data, focusing especially on static and dynamic measurement data sampled by Reykjavik University staff. Showing both time-series of acceleration and power spectral frequency plots.

The third chapter deals with dynamic analysis of structures, operational modal analysis (OMA) and system identification. The recorded acceleration data is used for identification of the bridge system, giving natural frequencies, and damping ratios for the key modes of vibration.

Chapter four deals with finite element modelling of the bridge. Two different types of finite element models were made, on one hand using Beam elements and on the other using Shell elements. The models were calibrated against the system identification results from chapter three to give correct eigenfrequencies and mode shapes characterizing the dynamic behaviour of the bridge.

In chapter five the key results from chapters three and four are summarized, compared and discussed. Then some key conclusions are deducted from the results. In addition, there are some suggestions for future research based on the available experimental data.

2 Monitoring of Steinavötn Bridge

Civil infrastructure is integral for the functionality of modern-day society. It includes buildings, bridges, roads, tunnels, factories, power plants, offshore installations, heritage structures, port facilities, and geotechnical structures, such as dams and foundations.

Bridges have for a long time been a key part of every society's infrastructure and have the potential of affecting various social, ecological, economic, cultural, and aesthetic aspects. The life of a concrete bridge starts with construction – the pouring of concrete. Followed by curing of concrete, then testing of the bridge and then finally, and the most important, the service period. During service, the structure might need refurbishing, strengthening or to be enlarged, according to necessities. At the end of service, the bridge can be dismantled. Monitoring a structure during each period of its lifespan is important and provides essential information for a better understanding of the structural behaviour and consequently a better planned and less expensive management [2].

From the establishment of experimental stress analysis in the 1940s up to the present time, experimental dynamic analysis has been incorporated in civil engineering applications. Consolidation of testing techniques, technical improvements of sensors and data acquisition systems, increased storage, and data transmission capacities in addition to the development of modern algorithms for structural and modal analysis has continuously increased the understanding of structural behaviour of both simple and complex structures [3].

Bridge monitoring programs have historically been implemented for the purpose of understanding and eventually calibrating models of the load-structure-response chain. Their monitoring, therefore, generally falls into the category of a feedback loop to improve future design, based on experience, or in some cases to verify new systems of construction [4] [5].

Bridge monitoring systems also provide ideal opportunities to implement and study structural health monitoring (SHM) techniques [6]. In the last decade, permanent bridge monitoring programs implemented in major bridge projects have often evolved into structural health monitoring systems [7].

Inaudi and Glisic [8], divided the purpose of monitoring into three categories: Structural management; increase of safety, and knowledge improvement:

Structural Management aims for operating safe and durable structures. Regular or continuous monitoring has an essential role in quality structural management. The monitoring data can be used to optimize the operation and all operational decisions regarding maintenance, repair and replacing of the structure can be based on reliable and objective data. The available information can both be used to discover structural deficiencies and structural aptness. Which may either lead to decisions to take immediate repair actions or to delay actions and increase safety margins for those structures that are in better conditions than otherwise excepted.

Increased safety of civil structures is as important as the consequences of their failure can be serious. Even when there are no fatalities, infrastructure out of service due to failure usually cause economic losses and even have ecological consequences.

Knowledge improvement will result in a better understanding of the currently existing structures as well as in better design of structures for the future. This should lead to more economical and more durable structures with increased reliability, performance, and safety. Monitoring the behaviour of structures and enlarging the knowledge of structural performance is important in this regard, as there are no two identical structures. The inherent structural diversity caused by factors such as geographical region, environmental influences, soil properties, loading etc., makes absolute behavioural knowledge impossible. Theories based on generalized simple models need to be tested and the real behaviour of structures built of new or unusual materials needs to be understood for possible refinement of structural theories. That is why lifelong structural monitoring, from construction to the end of service, is of interest from a theoretical point of view.

Traditional structural health monitoring (SHM) serves all three categories. The Steinvötn River monitoring project, however, does not really fall under the definition of SHM, since the monitoring only occurred after the failure of the bridge. But its purpose is certainly to improve knowledge and understanding of the behaviour of simple old reinforced concrete multi-span bridges, that can still be found in various locations in Iceland.

2.1 Overview of Experiments

This section provides a general overview on the monitoring experiments, undertaken on the old Bridge over Steinavötn, in the summer and fall of 2019, before it was demolished.

The Icelandic Road and Coastal Administration (IRCA) decided to use the bridge as a learning tool before it was demolished, and initiated full-scale experiments on the bridge in cooperation with several Icelandic and international parties. Various experiments were conducted on the bridge where acceleration, deflection, strain and static loading was measured [9].

Researchers from ETH in Zürich measured vertical acceleration response using single axis accelerometers. The sensors were installed during the summer to measure long term ambient background vibrations. Then they did a measurement campaign in September, where they conducted damage detection experiments on the bridge.

Figure 2.1: Accelerometers from ETH and RU distributed along the deck of the bridge.

The OSMOS Group set up real time strain measurements using Fibre Bragg sensors. The system consisted of OSMOS Optical Strands, Thermal Probe and the OSMOS Expert Data Acquisition System. The OSMOS Optical Strands are high-precision strain sensors based on fibre-optic technology that measures deformations between two points with micrometric resolution on a long-gage of 1 m. The sensors were installed in early July 2019 on the beams of the bridge in the span chosen for a full-scale load to failure test by IRCA. They recorded strain and temperature, from which the bridge deformation can be evaluated, through remote activation until the bridge was demolished in September 2019.

Figure 2.2: The OSMOS strain sensors installed on the girder and the LVDT differential displacement sensors on a timber platform.

Reykjavik University (RU) did two measurement campaigns on the bridge, using five 3-axial accelerometers and two LVDT displacement sensors, to monitor ambient and forced vibrations and low intensity static testing. The data from those measurements will be used in this project to analyse the response of the bridge. The details of the experiments and measurements will be discussed further in the following sub-chapters, 2.2 and 2.3.

Finally IRCA in cooperation with RU executed a shear capacity test on one span of the bridge in September. The bridge was loaded until failure and the force applied, the strain and displacement was monitored [10].

The measurements undertaken in 2019 were extensive and, in many ways, unique on a global scale, as relatively few concrete bridges have been tested in the same way, combining accelerometers and fiber optic strain sensors for dynamic measurements, as well as LVDT displacement sensors and fiber optic strain sensors for static measurements. The data sampled were time series of acceleration and strain measured for both ambient and forced loading on the bridge, such as vehicle loading, static loading, impact loading both direct from a mass dropped on the deck and indirect from pile driving close to the bridge. The bridge was also systematically damaged and finally jacked to a shear failure under ultimate loading conditions.

Full-scale testing of this type is important, considering that various design rules for concrete structures are based on results from tests on small concrete elements in laboratories that do not necessarily give an accurate picture of the overall behavior of real structures. IRCA plans to establish a data repository where the data from these campaigns will be made available.

First to all participants, then later perhaps to other interested parties. This has however not been realized yet, and the data available for this project is only the data collected directly by RU staff.

2.2 Phase I - Recordings in July 2019

The first sets of experiments took place on 4^{th}-5^{th} of July 2019. The objective of this phase was to install five accelerometers on the bridge deck and two LVDT sensors under the deck and then induce movement in the bridge by various methods. For example driving vehicles of different weights on to the testing-span and loading the span with concrete blocks for static testing. Table 2.1 provides a rough timeline of events during the day of testing.

The acceleration was measured using five Etna II instruments from Kinemetrics Inc. They are based on a tri-axial Epi sensor, which has good accuracy and very-low self-noise, resulting in 155 dB dynamic range. The two displacements sensors used were industrial LVDT transducers from Applied Measurements Limited with a stroke range of 0 – 100 mm. They had different mechanical configurations, one was spring loaded with a ball end and the other had a rod end bearing.

Table 2.1: Timeline of experiments in July.

Time	Test	Activities
		- Installation of measurement devices.
14:20	Set I	- Nissan Patrol jeep drove over a 50mm timber beam.
		- The jeep backed off the bridge again
		- This was repeated 3x over a period of 6-7 min.
14:28		- A Mercedes Sprinter repeated this process again 3x over 6-7 min.
14:48	Set II	- The sprinter repeated the process again 2x over a 75mm beam.
15:00	Set III	- The 75mm beam was moved to the middle of the next span.
		- The sprinter passed over the timber in same way as before.
		- The process repeated a few min. later.
15:23	Set IV	- The previous action repeated.
16:14	Static tests	- First concrete block lifted onto the main span.
16:45		- Second block lifted onto the span.
17:25		- Four additional blocks added.
18:10		- Unloading blocks started.
18:27		- The final block is dropped from ca. 25 cm height.
		- The previous process repeated 1 min later.
18:35/40		- Truck drove onto the bridge
18:43		- Truck backed off the bridge
-		- Truck drove onto the bridge
18:50		- Truck backed off the bridge

The LVDT sensors and 3D accelerometers were installed on the eastern half of the bridge, or over spans 4-6 according to the numbering in Figure 1.4. The accelerometers were placed along the side beams of the bridge deck, the first three on the northern beam and the last two on the southern beam as seen in Figure 2.3 and 2.4 and drawing in Appendix B.1 where a more detailed position is shown. The LVDT sensors were placed under the side beams, one on each side, in the middle of span 5, the second span from the east, as seen in Figure 2.5.

Figure 2.3: Position of the accelerometers in July.

Figure 2.4: Setup of the 3D accelerometers (from left: battery, accelerometer and gps).

Figure 2.5: LVDT sensors below the bridge deck (left: rod end bearing, right: spring loaded with a ball end).

During *Set I* a 50mm thick timber beam was placed on the middle of the first span from east and the Nissan Patrol jeep drove onto the bridge, over the beam, and back off the bridge again. A Mercedes sprinter then repeated the process. Each driving onto the bridge and back 3 times. In *Set II* the 50mm timber beam was replaced by a 75mm beam and the Mercedes sprinter repeated the process two times. For *Set III and IV* the 75mm beam was moved to the next span, second from the east, which was of main interest and the Mercedes sprinter repeated the process two times in each set.

Then the *static tests* begun. In total 6 concrete roadblocks were lifted onto the middle of the second span from east, one by one, and placed as seen in Figure 2.6 and 2.7. They were then removed again one by one but as the final block was being lifted off it was dropped twice from a height of ca. 25cm.

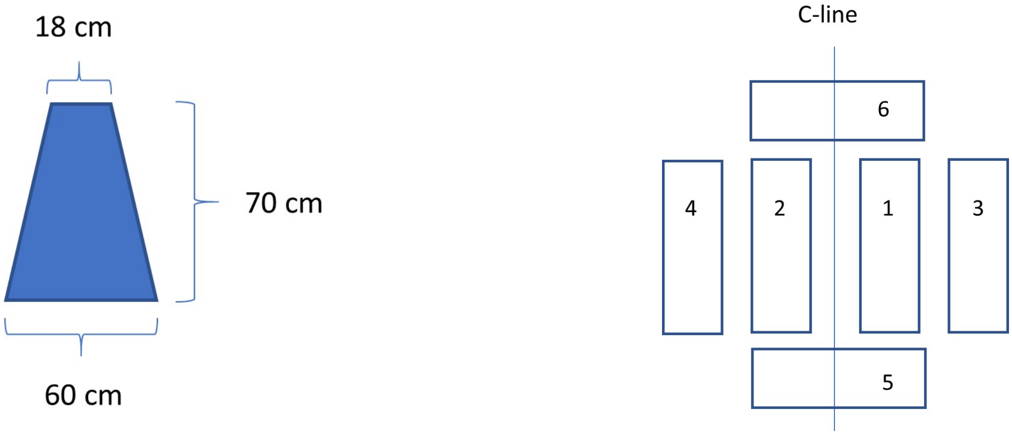

(a) Geometry ($l = 1.9m$).

(b) Placement.

Figure 2.6: The geometry and placement of the concrete blocks. The numbering indicates in which order the blocks were placed and corresponds to Table 2.2.

Figure 2.7: The concrete blocks on the bridge span during static testing.

Figure 2.8: The Roto Merlo truck on the bridge span during static testing.

Since the 6 concrete blocks had a relatively small impact on the deflection of the span it was decided to drive the Roto Merlo truck on to the bridge, see Figure 2.8. And as it drove onto the main span it drove over both the 50mm and 75mm beams.

An overview of all loads applied in both the dynamic and static tests is provided in Table 2.2. It should be noted that the concrete blocks were weighted by the Roto Merlo truck and the results are suspect to criticism as it is inconceivable that standard blocks can have 25% variation in mass.

Table 2.2: Applied loads during testing.

Load type	Mass [kg]
Nissan Patrol Jeep	>1500
Mercedes Benz Sprinter	>2480
Concr. block 1	1020
Concr. block 2	990
Concr. block 3	990
Concr. block 4	820
Concr. block 5	770
Concr. block 6	760
Roto Merlo Truck	14750

In addition to the aforementioned activities that day the modulus of elasticity of the concrete was measured. To verify the modulus of elasticity of the concrete, ultrasonic pulse velocity measurements were carried out. To perform the measurements an instrument called "PUNDIT", (Portable Ultrasonic Non-destructive Digital Indicating Tester) manufactured by CNS Instruments Ltd., was used. As the name suggests, it is particularly suitable to explore the properties of concrete in a buildings serviceability state as it has no damaging impact on the concrete. The instrument emits ultrasonic pulse wave of 54 kHz from a transmitter, through the material being tested, to a receiver and measures the travelling time of the wave. The instrument and an example of the basic method of its use is shown in Figure 2.9

Knowing the travelling time and length between the transmitter and receiver allows for the calculation of the longitudinal pulse velocity, V_L. Then the modulus of elasticity, E, of the concrete can be calculated by the following equation:

$$E = \frac{V_L^2 \rho (1+v)(1-2v)}{(1-v)} \tag{2.1}$$

The concrete is assumed to have a density, ρ, of 2500 kg/m3 and a Poisson ratio, ν, of 0.2. The measurements were performed on the first two pillars from the eastern end and on the side beams of the deck cross section where each of the accelerometers were placed.

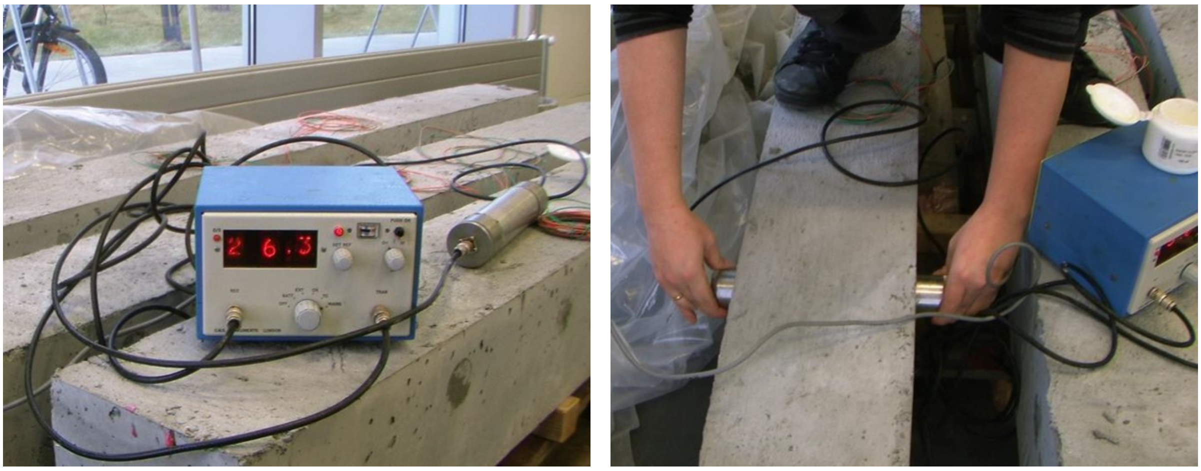

Figure 2.9: An example of the Pundit instrument in use.

The results from the measurements are shown in Table C.1 and then summarized in Table C.2 in Appendix C. The combined average value of the modulus of elasticity, E, is found to be 39 GPa, which is considerably higher than the previously anticipated value by IRCA of about 30 GPa, corresponding to concrete quality C25 [11]. It is also seen that the pillars tend to give somewhat higher values (E=43 GPa) than measured for the deck (E = 37 GPa).

It should be noted that the values measured represent the dynamic elasticity modulus, which is generally about 20% higher than the static one [12]. Also, the concrete surfaces were very rough, which could affect the results to some degree, but that should mainly increase the variance of the measured values rather than influencing the average.

2.3 Phase II - Recordings in August 2019

The second phase of measurements took place from 27^{th}-28^{th} of August 2019. The objective this time was to monitor both the ambient noise and the response when piles were driven into the sand next to the first bridge span from east. The purpose of the pile driving was to create a reaction-foundation, with 5 concrete piles in the sand on each side of the bridge, for a shear failure test, which would be performed by IRCA in September 2019 (see [10] and [9]).

The accelerometers were positioned in a similar way as in the first phase except that two of the devices, nr. 2 and 3 in Figure 2.3, were moved down to the piers, as shown on a layout drawing in Appendix B.2. The plan was to try to get an input–output measurement by placing two accelerometers at the bottom of the pillars, and keeping three on the deck. However, due to the high water level in the river at the time it was not considered save to put the accelerometers on the pillar foundation, so they were placed on the upper side of the two pillars supporting span no. 2 from east as seen in Figure 2.10.

Figure 2.10: The placement of the accelerometers on the pillars.

Related to the activities on the bridge, the data can be split into three groups.

1. The first data group is comprised of eleven one-hour records of ambient acceleration response from 21:00 on August 27th, to 08:00 August 28th.
2. After 8:00 preparations for the pile driving started and lasted until the first pile was erected between 14:00 and 15:00 so the second data group can be considered linked to the preparation period between 8:00 and 14:00 on August 28th.
3. The third data group can then be considered linked to the pile driving period between 14:00 and 19:00.

After 19.00 the battery driven instruments gradually started to lose power, so effectively the measurements are considered to stop at 19:00 on the 28th.

Additionally microtremor recordings were performed overnight close to the bridge, using a tri-directional Lennartz LE-3D/5s seismometer and REF TEK 130-01 broadband seismic data acquisition system. Each axis had the same set parameters. The sensor was collecting data at a rate of 100 Hz with high gain. The seismometers were placed on top of the surface of interest and covered with nearby shovelled soil to minimize any wind effects. The seismometer recorded the ambient vibrations in the sand from 20:00 on August 27 until 11:00 an August 28. The instrument was removed before the pile-driving started. In section 2.4.4 this data will be used to estimate the response properties of the site and the thickness of the gravel layer.

2.4 Recorded time series and PSD plots

In this section examples of the measured data will be given such as displacement recordings, acceleration time-series, Power Spectral Density plots and HSVR analysis based on ambient noise measurements of surface velocity.

2.4.1 Displacement measurements in July 2019

The displacement signals were sampled at 10 Hz, although the sensors are not dynamic instruments by nature. Spectral analysis using their signals did also not show any dynamic response, which is as expected since the lowest natural mode of vibration of the structure was found to have a natural frequency of about 5.6 Hz, which is above the Nyquist frequency of 5 Hz. The sampling frequency of 10 Hz was more intended to be able to follow the quasi-static behaviour of the bridge deck. At the time of preparation for the measurements, the type of loading and its intensity was also not fully known, nor the exact response characteristics of the bridge.

The signals presented in the following figures were "smoothed" using a MATLAB [13] function “smoothdata” with the option of running a moving median average over every 20 consecutive points. Figure 2.11 gives an overview of the monitoring sessions on the 4^{th} of July. The figure shows the displacement values with the starting offset, which is controlled by the positioning of the measurement instruments, which have a stroke of ± 50 mm.

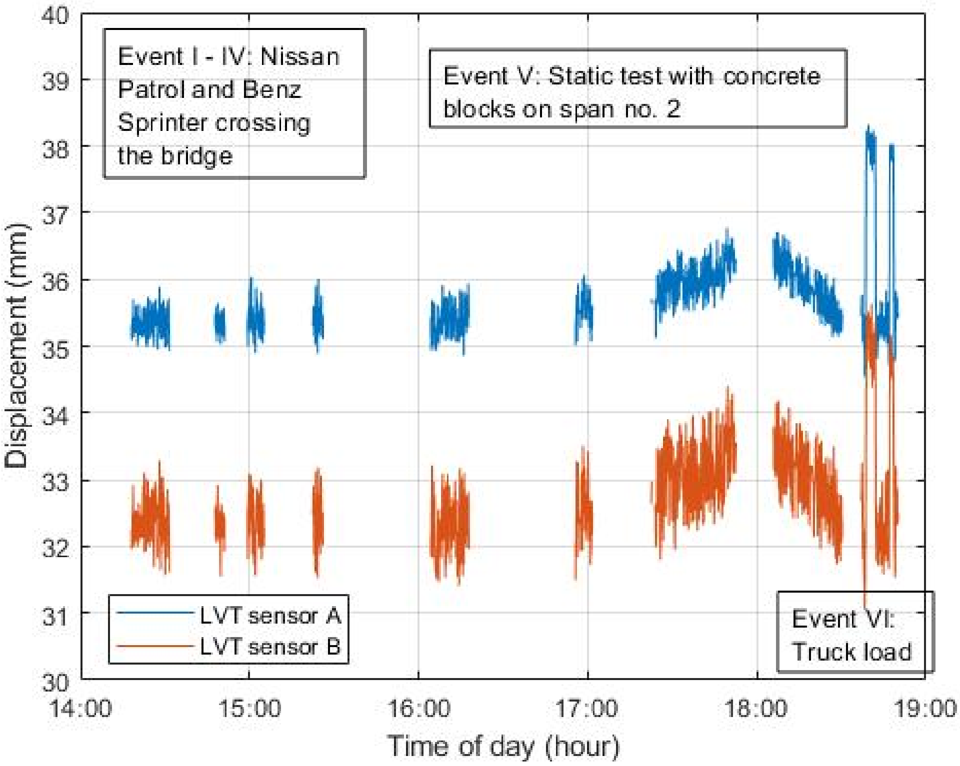

Figure 2.11: An overview of the time history of displacement monitoring.

The first four events (from 14:20 to 15:27), consisted of the Nissan Patrol jeep and Mercedes Benz Sprinter driving over planks on the first span (from east) and then over planks on the second span (from east), as outlined in Table 2.1. The primary idea was to attempt to get an impulse-like excitation of the bridge deck. The static displacements were not of primary importance for these events and therefore the exact timing of the position of the car or the stops on the bridge were not documented in detail. However, looking at the displacement records, it is considered reasonable that the Sprinter induced a static displacement of about 0.5 mm on the bridge span. Figure 2.12 gives an overview of the displacements recorded during these events.

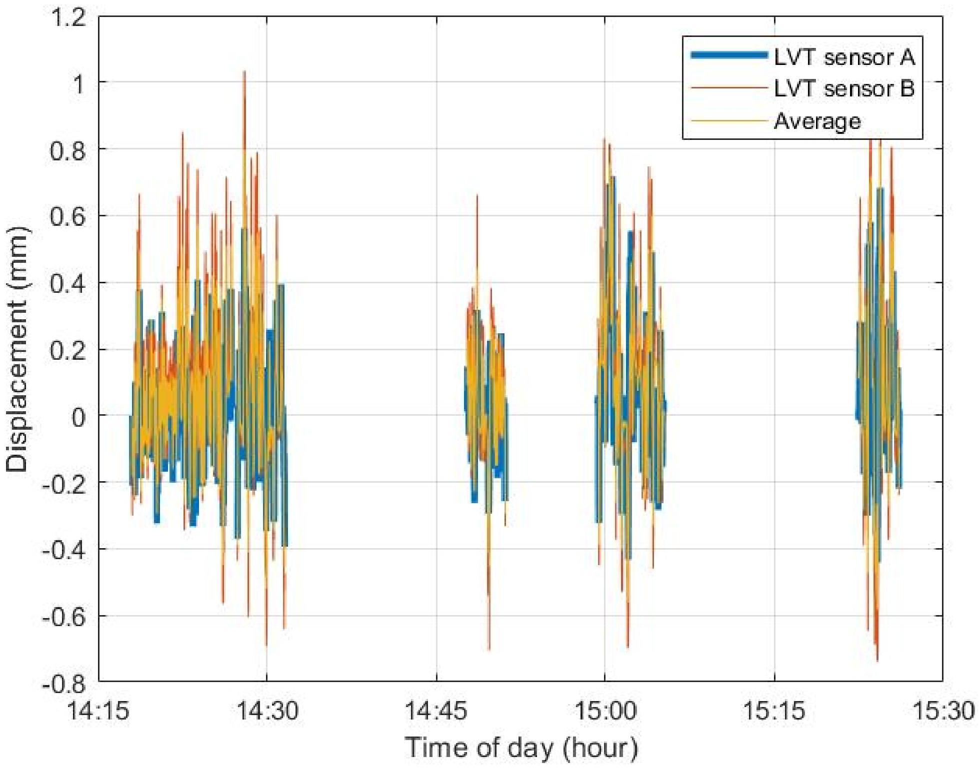

Figure 2.12: The displacement induced by a Nissan Patrol and M-Benz Sprinter driving over the two eastern most bridge spans.

The fifth event (from 16:10 – 18:30) was static loading of six concrete blocks in the center of the second span. Figure 2.6 shows the arrangement of the blocks which were loaded one by one, on to the bridge, and then again removed one by one. Figure 2.13 shows the development of the gradual displacement increase and decrease depending on the number of blocks on the span above the displacement transducers. It should be noted that the mass of the individual concrete blocks varied somewhat. The discontinuity in the displacement time series is due to problems with the data acquisition system, which was affected by the rainy weather during the day. It is estimated that the static displacement at peak loading was about 1 mm.

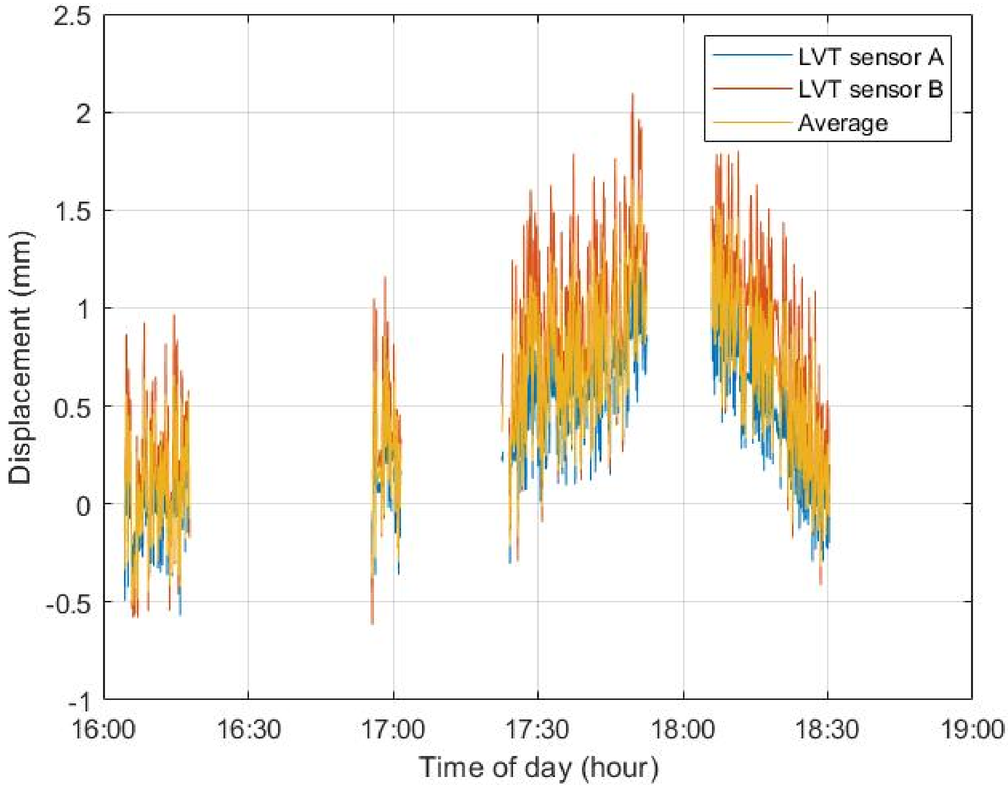

Figure 2.13: The disp. induced by six concrete blocks at the center of span 2 from east.

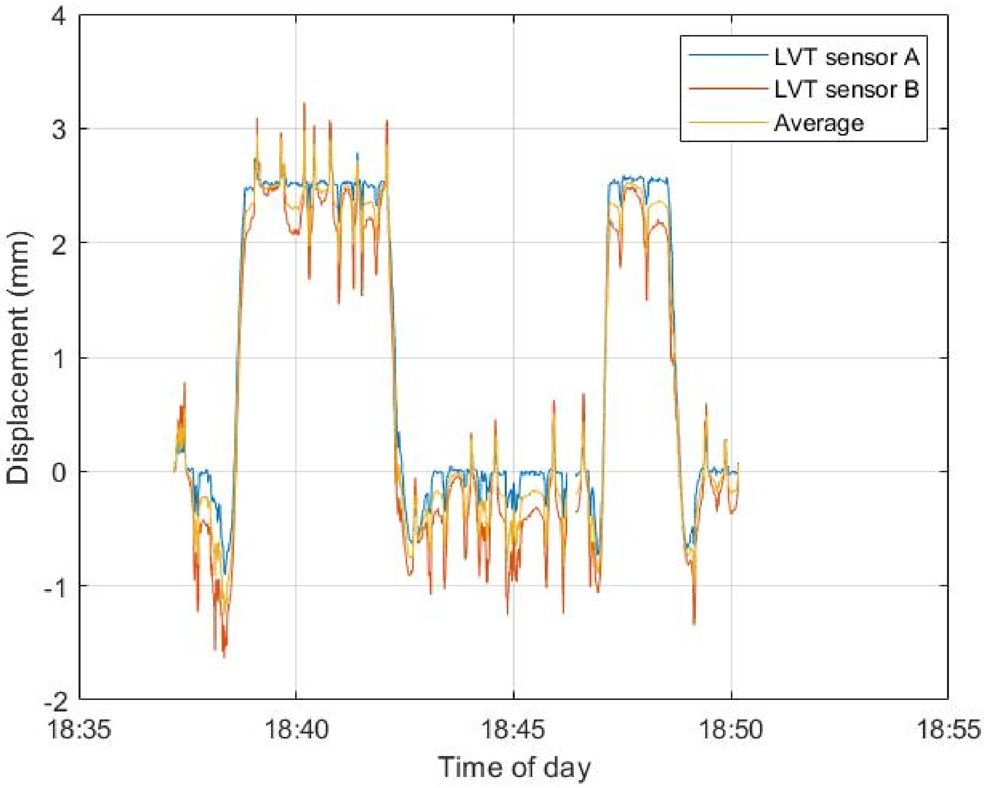

Figure 2.14: The disp. induced by a Roto Merlo truck driving twice onto the bridge.

The sixth event (from 18:35 – 18:50) involved a Roto Merlo truck driving onto the bridge and stopping at the center of span no. 2 (from east) for a few seconds, then driving off again and then repeating this process once more. Figure 2.14 shows the combined action as the truck drives twice onto that span and stops. It is estimated that the truck‘s loading produced a displacement of about 2.5 mm.

The estimated static loading and the resulting average maximum displacement is summarized in Table 2.3. As can be seen from Table 2.3, there is an internal correspondence between the estimated loading and the estimated displacement. However, it should be noted that neither can be established very accurately, due to uncertainties in the true weight of the vehicles and the concrete blocks as well as instability in the displacement monitoring devices. Sensor A, which has a spring resistant push down action, gives a more stable estimate of the displacement. Sensor B on the other hand has an unrestrained pull out – push in action, that gives a more dynamic and larger reaction to the loading processes, especially for the lower force levels. For higher force levels they largely show a similar displacement on average. The noticeable difference between the two sensors, is more likely related to their own characteristics, rather than a real difference in displacement at the two measurement locations. When the displacements are within a mm, the fixture of sensor B to the bridge, may also come into play as the screw attaching it to the concrete beam may not have fully restrained the end of the probe. Overall, it is my belief that sensor A, gives a more accurate and reliable measure of the static or quasi-static displacements of the beam.

Table 2.3: Summary of estimated static loading and displacement of bridge span.

Event no.	Type of Loading	Estim. loading [kN]	Estim. average max. displacement [mm]
I-IV	M-Benz / Sprinter Tourer long	30	0.5
V	6x concreat blocks	60	1.0
VI	Roto Merlo, M40.26 MCSS	150	2.5

These results will be used to validate a FE model, by applying to it a static loading equivalent to the cases of the concrete blocks and the Roto Merlo truck, see Chapter 4.

2.4.2 Acceleration measurements in July 2019

The acceleration was sampled continuously at 200 Hz on all channels during the monitoring period from 13:00 to 19:00 on July 4^{th} 2019. Examples of the acceleration time-series recorded at the center of span 2 from east (Instrument nr. 3 in Figure 2.3) will be given.

The first sample chosen, Figure 2.15, is from the first hour of monitoring (13:00-14:00), before any specific action took place. But still there was some undefined action on the bridge, that resulted in some random ambient excitation and with some acceleration spikes in the response. However, the acceleration levels are low. The signals shown are the raw data recorded without any filtering or decimation.

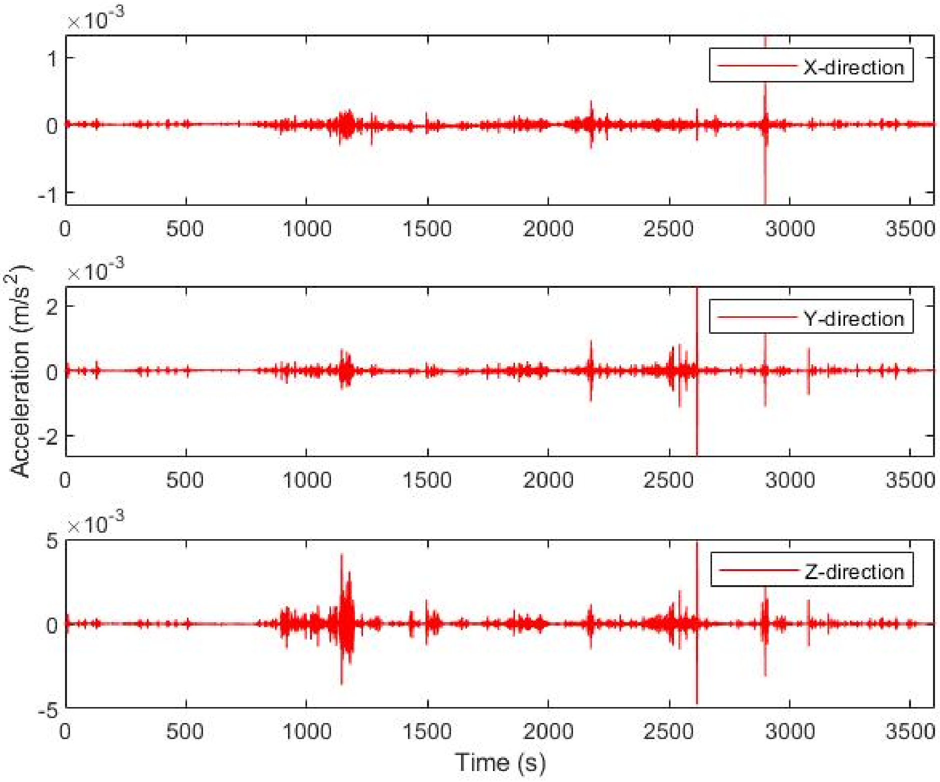

Figure 2.15: Time series of acceleration recorded between 13:00-14:00 on July 4th 2019.

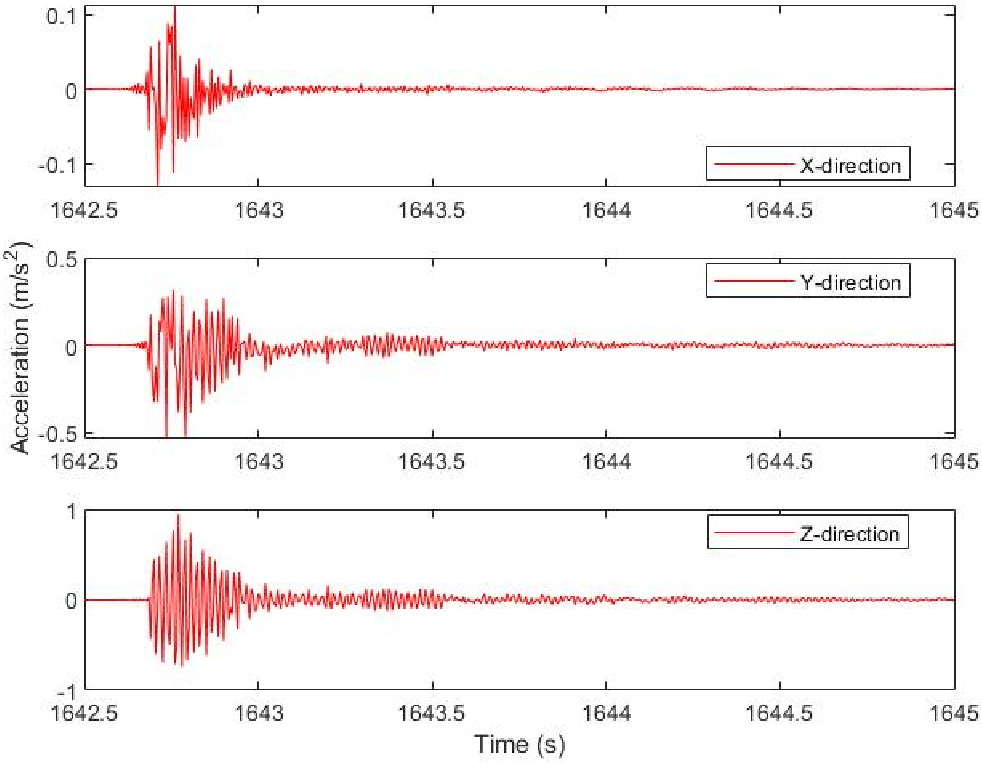

Figure 2.16: Time series of acceleration recorded between 18:00-19:00 on July 4th 2019.

The second sample chosen, Figure 2.16, is a short segment from the last hour of monitoring during July 4^{th} 2019. It shows the recorded response when one of the concrete blocks was dropped on the bridge. As can be seen the vertical (z-axis) acceleration level is high, but the drop also excites the lateral directions, especially the transverse (y-axis) direction. The duration of strong motion is however very short or only a fraction of a second.

The absolute peak vertical acceleration levels observed during the monitoring session of July 4^{th} 2019, are displayed in Table 2.4. The values are shown for all the sensors. As can be noted the vertical acceleration levels are in all cases largest at the centre of span 2 (sensor 3), except for the first hour, when basically ambient noise was recorded. The maximum lateral acceleration was generally considerably smaller than the vertical one. Normally varying from 10% to 50% of the vertical acceleration. Although for the case shown in Figure 2.16, the y- and z-components were of the same order of magnitude.

Table 2.4: Absolute maximum vertical acceleration recorded during July 4, 2019.

Excitation	Hour	Sensor 1 m/s2	Sensor 2 m/s2	Sensor 3 m/s2	Sensor 4 m/s2	Sensor 5 m/s2
Ambient	13-14	0.020	0.004	0.005	0.005	0.002
Set I & II	14-15	0.150	0.052	0.111	0.082	0.049
Set III & IV	15-16	0.049	0.084	0.131	0.074	0.040
Static	16-17	0.028	0.045	0.189	0.054	0.012
Static	17-18	0.037	0.062	0.135	0.078	0.034
RC Blocks dropped	18-19	0.110	0.304	0.946	0.326	0.083

For a quick look at the frequency content of the acceleration records, the normalized power spectral density (PSD) was evaluated for each time series at each measurement point and then they were averaged over the duration of the monitoring period based on the direction of motion. The results are shown, in a log-log scale, in Figures 2.17-2.19, for each measurement direction.

The power spectra were evaluated using the "pwelch" function in MATLAB which is based on the Welch method for calculating power spectra. The number of points in the Fourier spectra were NFFT = 8192, the sampling frequency was 200 Hz and double overlapping was used. The signals in each direction were then averaged for each monitoring station and measurement hour. As can be seen the spectral peaks are clearly visual in the vertical signal, Figure 2.19. The peaks at 1.8 Hz and 2.8 Hz are most likely linked to the sandy foundation of the bridge, which will be discussed further in section 2.4.4. Looking at the PSD of the vertical acceleration, at least 5 relevant modes of vibration can be observed, at 5.6 Hz, 6,6 Hz, 8.0 Hz, 9.6 Hz and 11.4 Hz. This will be demonstrated and analysed further in Chapter 3. There is a considerable noise noticeable at high frequencies that is not of interest for this study and will be filtered out in further analysis.

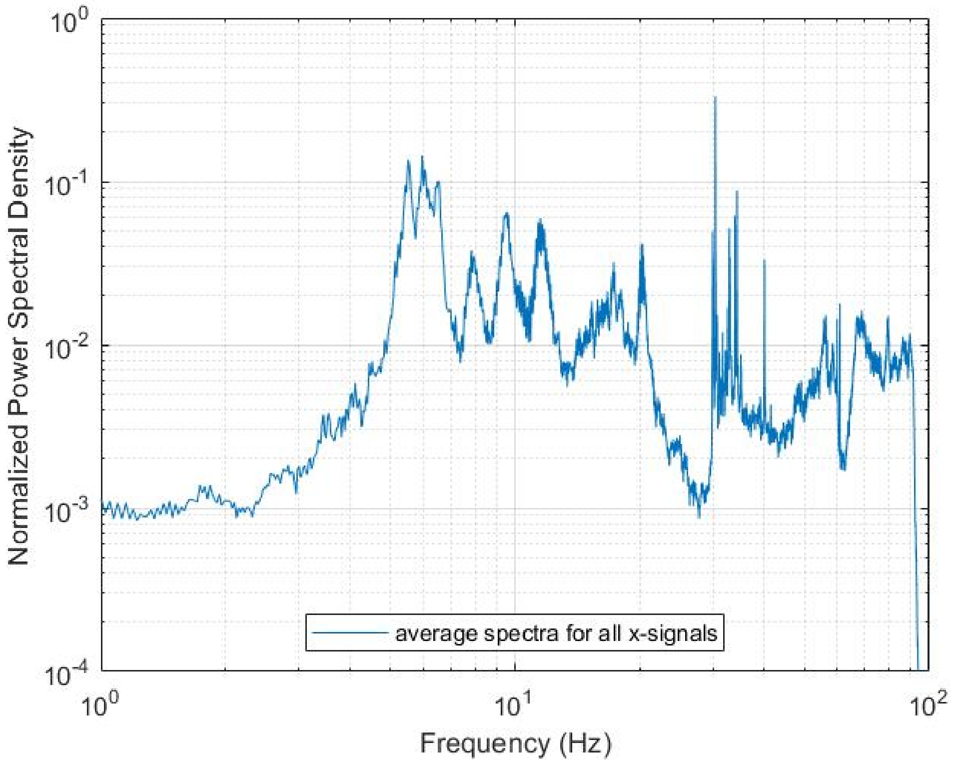

Figure 2.17: Averaged normalized Power Spectral Density for all recorded longitudinal signals as a function of frequency on July 4, 2019.

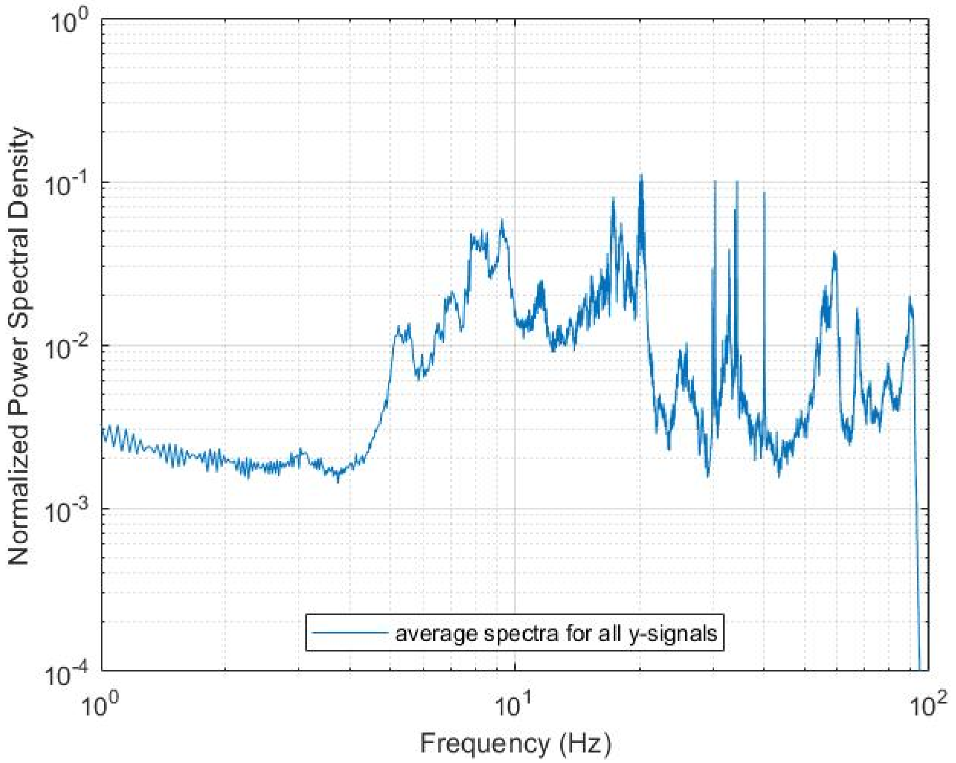

Figure 2.18: Averaged normalized Power Spectral Density for all recorded transverse signals as a function of frequency on July 4, 2019.

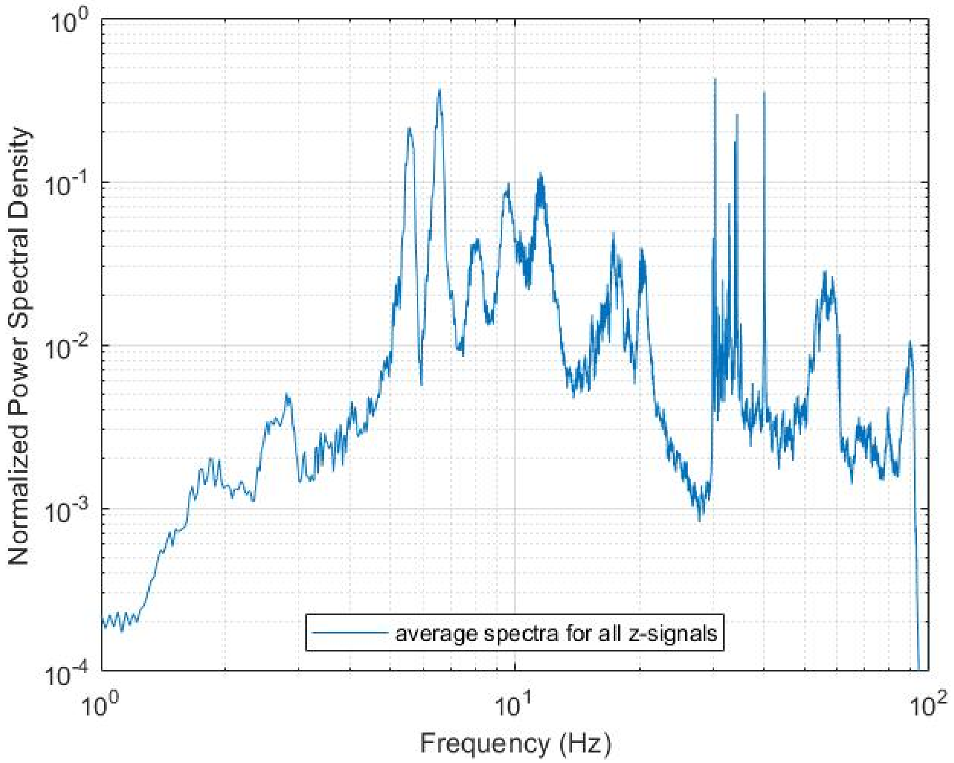

Figure 2.19: Averaged normalized Power Spectral Density for all recorded vertical signals as a function of frequency on July 4, 2019.

2.4.3 Acceleration measurements in August 2019

The setup of the accelerometers during the August campaign, has been described in section 2.3. Again the acceleration was sampled continuously at 200 Hz on all channels during the monitoring period from 21:00 on August 27^{th} to 19:00 on August 28^{th} 2019. Examples of the acceleration time-series recorded at the center of span 2 from east (Instrument nr. 3 in Figure 2.3) will be given.

Figure 2.20, which shows the absolute peak values of recorded vertical acceleration, and Figure 2.21, which shows the standard deviation of recorded vertical acceleration, demonstrate the three monitoring stages discussed in section 2.3.

It is noteworthy that nearby traffic keeps the noise level up into the night, then after about 1 o'clock the environmental noise level goes down, and then from about 6 o'clock, it starts to increase again. Then after 8:00 the pile driving preparations start. It is seen that the sensors on the pillars give lower response than the sensors on the deck, except during the pile driving, then response of sensor 5, which is closest to the piles, increases.

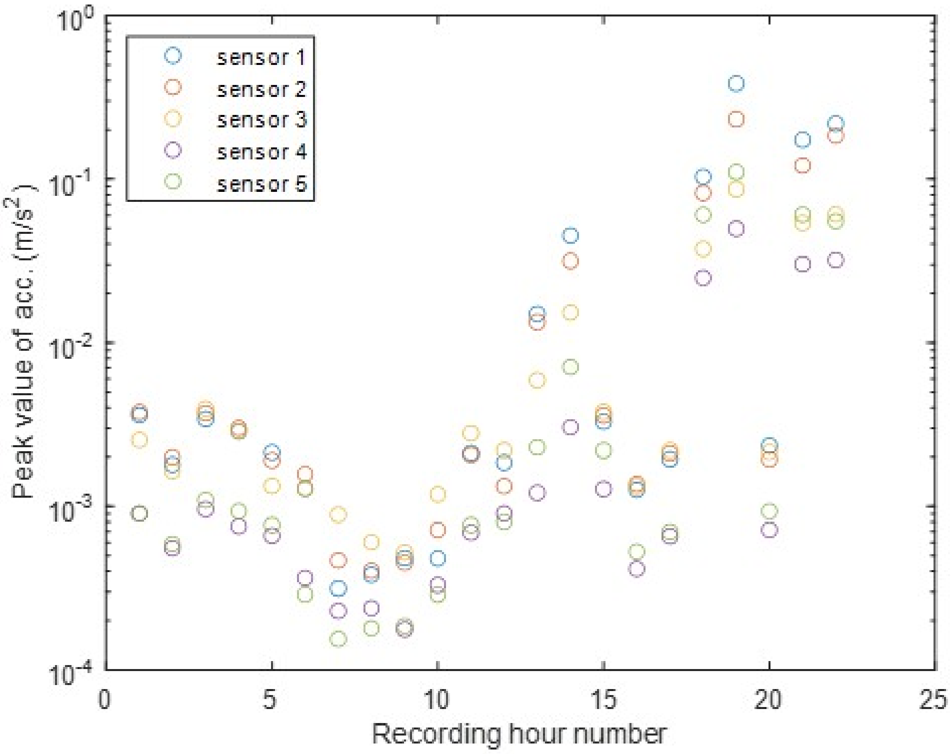

Figure 2.20: Absolute peak value of recorded vertical acceleration during the period 27/8, 21:00 to 28/8, 18:00.

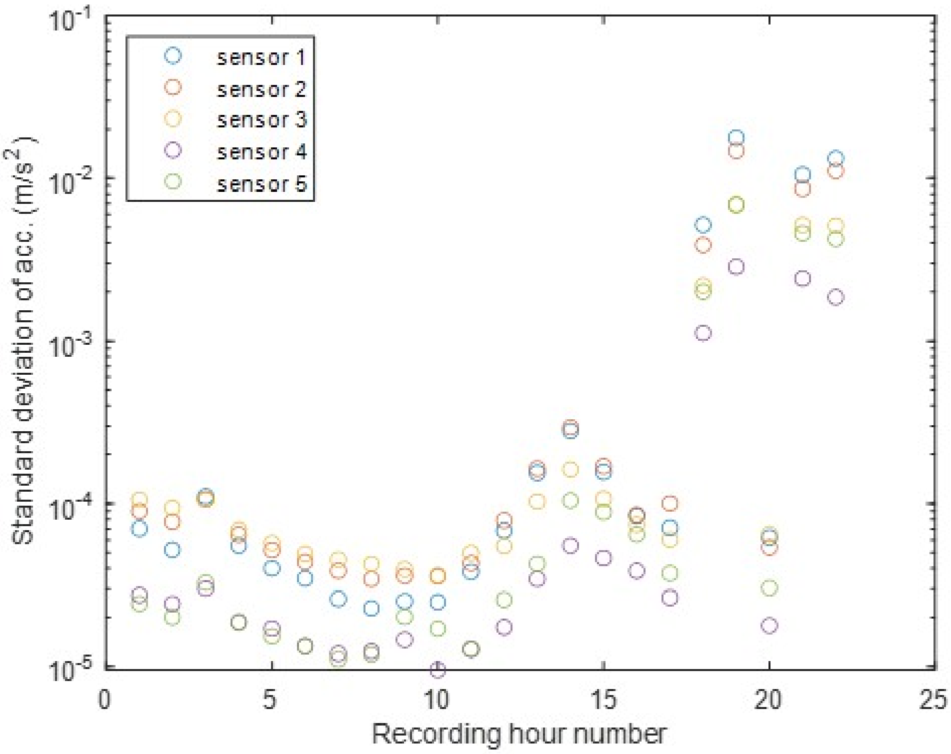

Figure 2.21: Standard deviation of recorded vertical acceleration during the period 27/8, 21:00 to 28/8, 18:00.

It is usually sensor 3, at the center of span 2 from east that shows the largest response of the five. The ratio between peak value and standard deviation varies, as the acceleration series often have individual spikes that dominate the peak values, but on average the ratio is about 30. The transverse response (y-direction) of the deck sensors is generally only half or less of the vertical response and the longitudinal response (x-direction) of the deck sensor is about half of the transverse response. This is, however, different for the sensors on the pillars, where all response signals are of similar amplitude.

Figures 2.22, 2.23 and 2.24 show 90 s examples of the time series recorded by sensor 3 at the center of span 2 from east, during the three excitation phases on 28^{th} of August.

Firstly, Figure 2.22 shows an example of the ambient noise recorded during the night between 2:00 and 3:00. As can be seen the signal recorded is more or less a steady noise.

Secondly, Figure 2.23 shows an example of the noise recorded between 10:00 and 11:00, while the pile driving was being prepared. The acceleration series are characterized by short term acceleration spikes, related to the activities around the bridge.

Thirdly, Figure 2.24 shows an example of the acceleration recorded during the pile driving between 17:00 and 18:00. Here we have periods of steady pounding at a relatively fixed frequency, as shown, and then intervals of lesser or no activity in between, as demonstrated by the first few seconds of the time series shown.

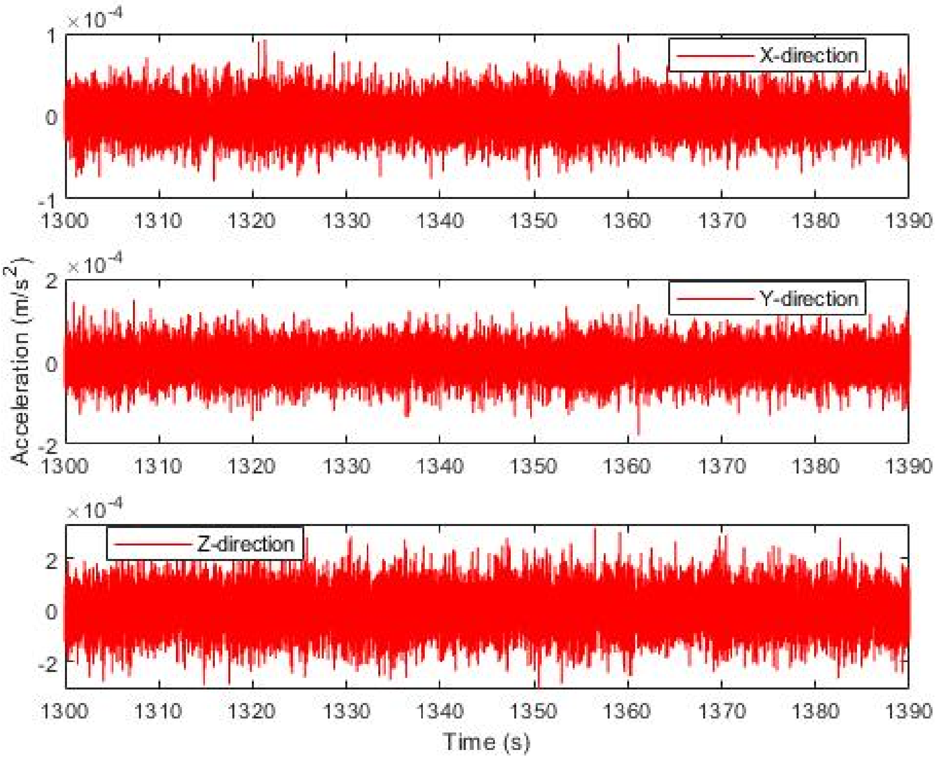

Figure 2.22: A 90 s example of the time series recorded by sensor 3 at the center of span 2 from east between 2:00 and 3:00 on August 28^{th}, 2019.

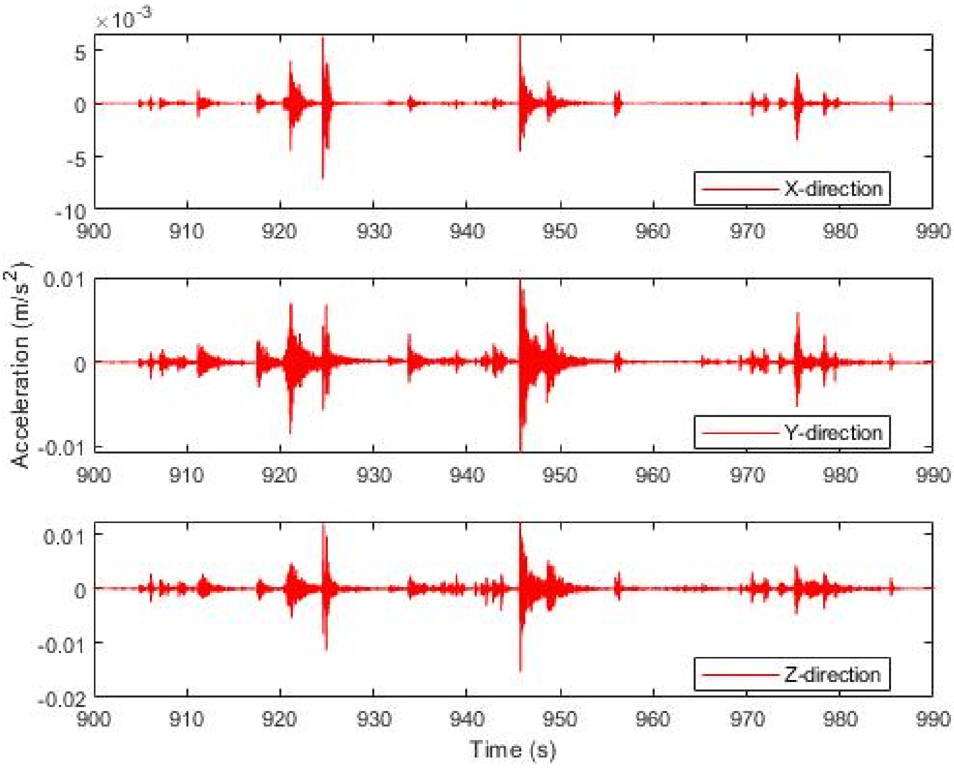

Figure 2.23: A 90 s example of the time series recorded by sensor 3 at the center of span 2 from east between 10:00 and 11:00 on August 28th, 2019.

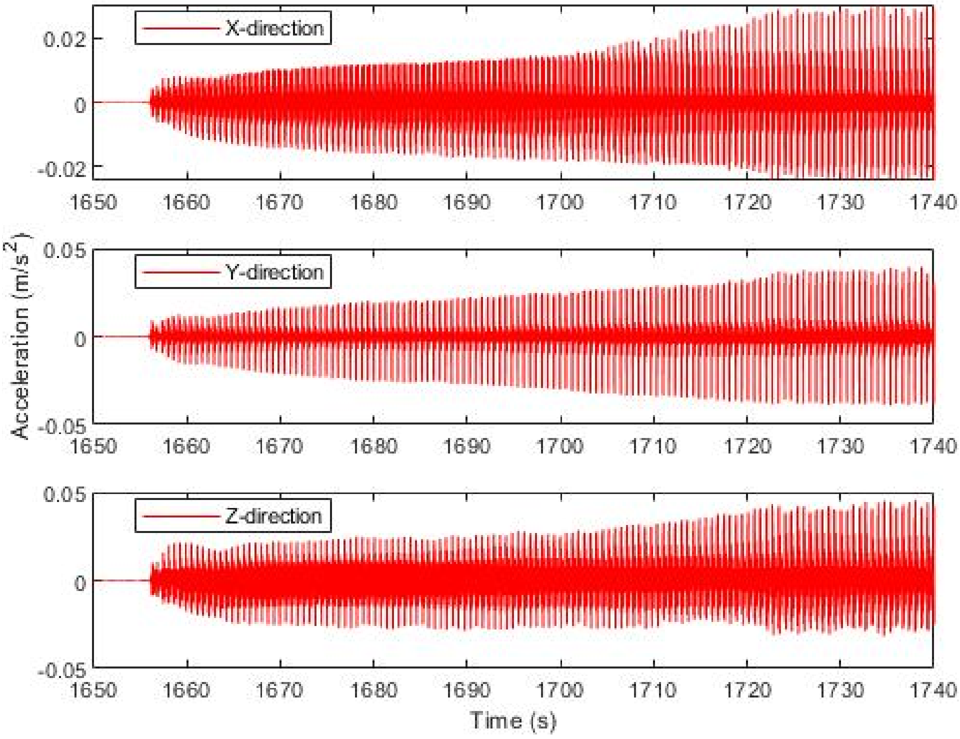

Figure 2.24: A 90 s example of the time series recorded by sensor 3 at the center of span 2 from east between 17:00 and 18:00 on August 28th, 2019.

Figures 2.25 through 2.33 give an overview of the frequency content in the recorded signals for the three data groups previously mentioned. The spectra is evaluated as before using the "pwelch" function in MATLAB, for each group of recorded signals, with 8192 points in the NFFT and a sampling frequency of 200 Hz.

The ambient noise spectra recorded during the evening of the 27^{th} and the night of the 28^{th}, show similar characteristics as the spectra of the July data. They are however, cleaner in sense and less noisy. Partly because the average includes 12 hours instead of 6 in July. But mainly it is because there is no activity on or around the bridge at that time. It is noteworthy how strong the spectral peak at 5.7 Hz is in the x-signal. Again, the spectrum of the transverse motion has lower amplitude and less prominent peaks than the spectrum of vertical motion, although peaks at 12 Hz and 20 Hz are seen in both, which might indicate some torsional vibration in those modes.

During the pile driving preparation period heavy vehicles were driven in the water saturated sand around the bridge, transporting the piles etc. The acceleration records and the corresponding spectra, shown in Figures 2.28 to 2.30, from that time are affected by this. The frequency peaks observed at 1.8 Hz and 3.4 Hz correspond to the frequency response of the sand underneath and around the bridge, which will be discussed further in section 2.4.4.

During the pile driving period, the acceleration response is dominated by the frequency of the hammer blows, as seen in Figure 2.24. The hammer used was a HYDROHAMMER® S-30 (IHCIQIP.COM) which has 65 blows/min or about 1 blow/s and provides an energy input in the range of 3-30 kJ. It is noteworthy that the hammer induces acceleration response at regular frequency intervals, i.e. 1.5 Hz, 3 Hz, 4.5 Hz, 6 Hz, 7.5 Hz, etc. This is particularly clear through the spectra of transverse motion shown in Figure 2.32. The key structural modes of vibration can still be seen in the vertical acceleration spectra in figure Figure 2.33, but they are disturbed and confused by the forced excitation.

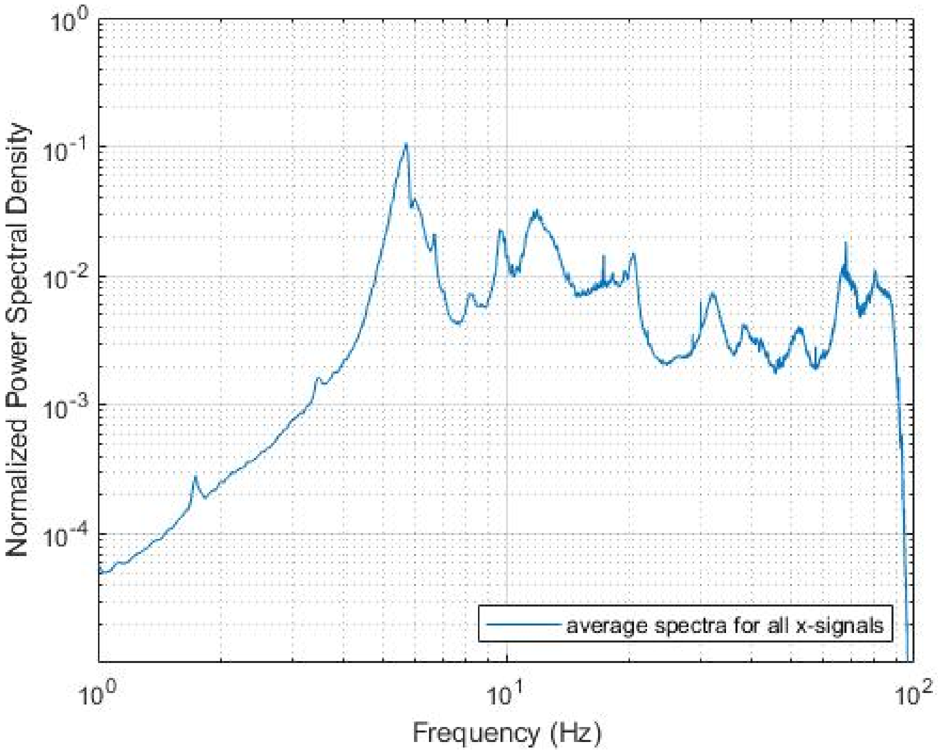

Figure 2.25: Averaged normalized Power Spectral Density for all recorded longitudinal signals as a function of frequency from August 27^{th} 21:00 – 28^{th} 08:00 2019.

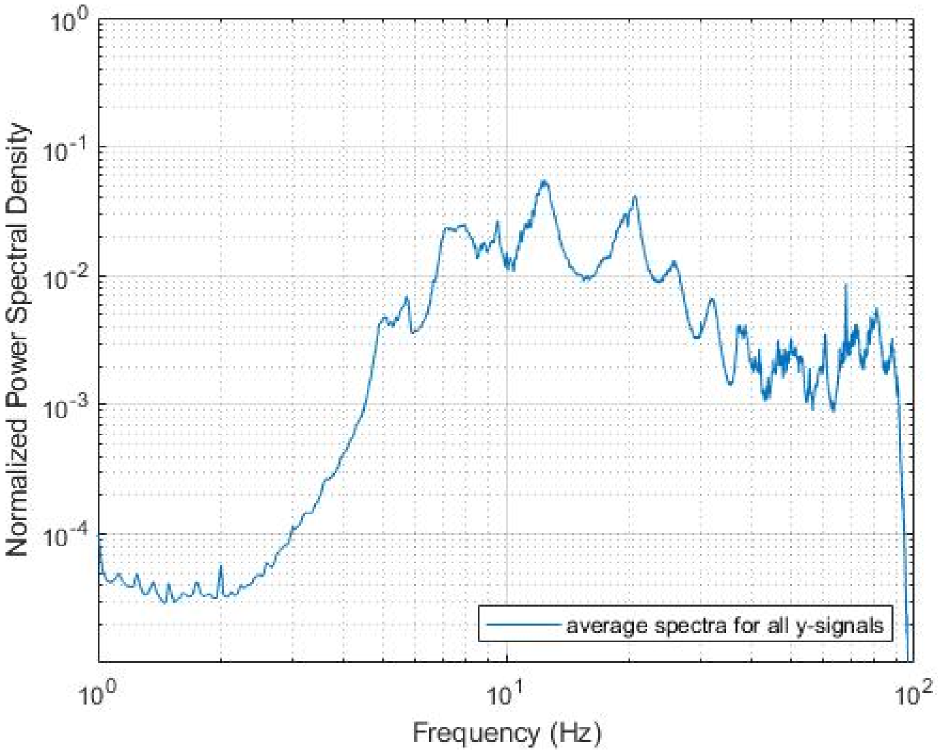

Figure 2.26: Averaged normalized Power Spectral Density for all recorded transverse signals as a function of frequency from August 27^{th} 21:00 – 28^{th} 08:00 2019.

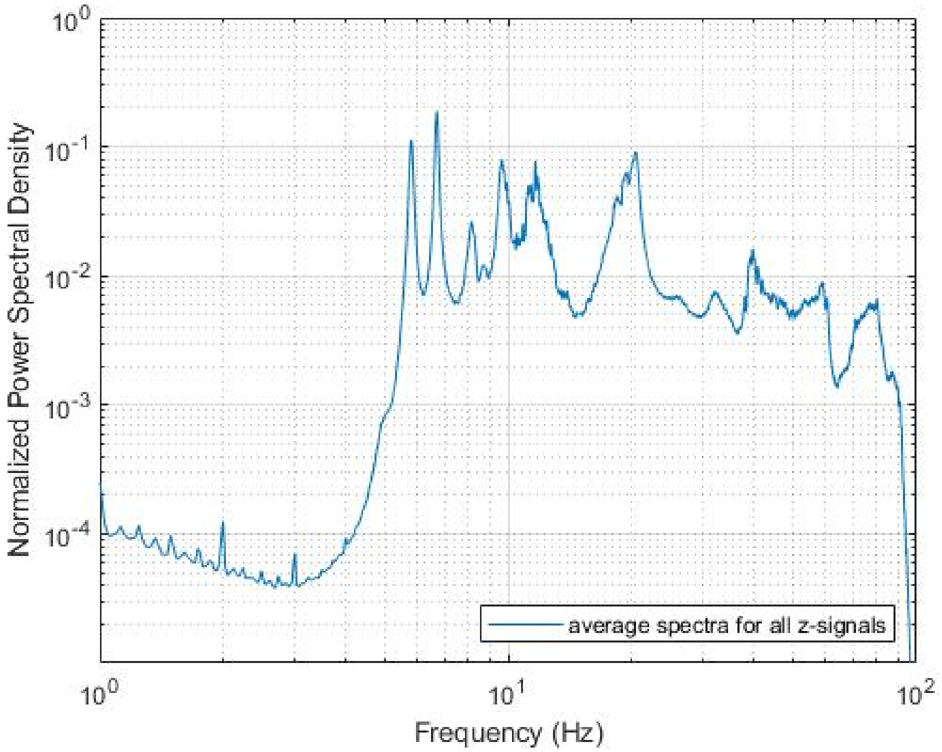

Figure 2.27: Averaged normalized Power Spectral Density for all recorded vertical signals as a function of frequency from August 27th 21:00 – 28th 08:00 2019.

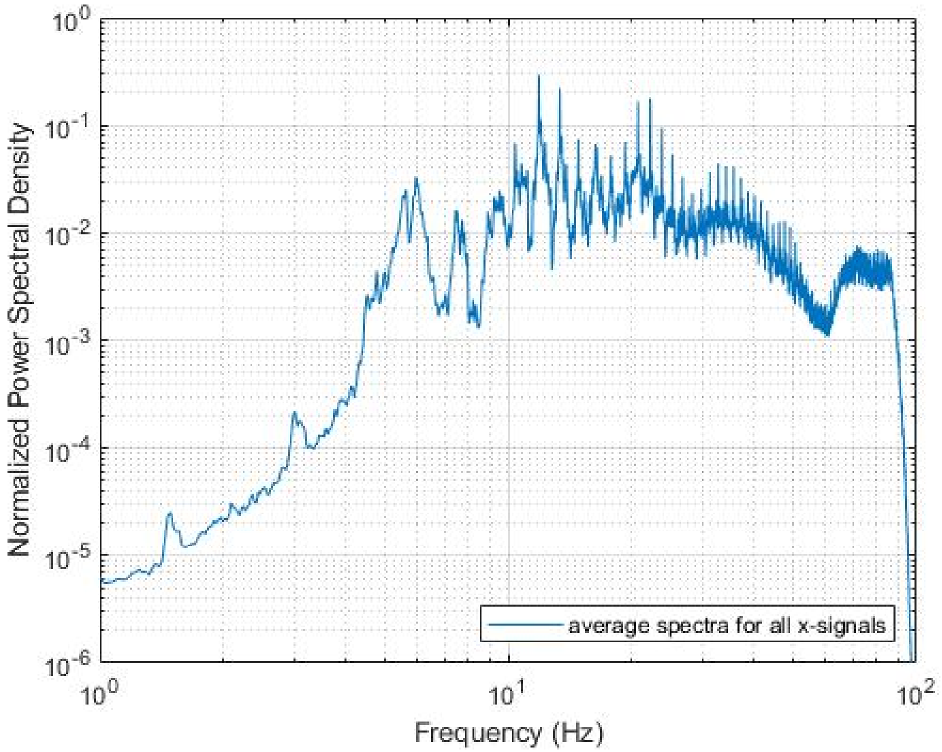

Figure 2.28: Averaged normalized Power Spectral Density for all recorded longitudinal signals as a function of frequency from August 28th, 08:00 – 14:00, 2019.

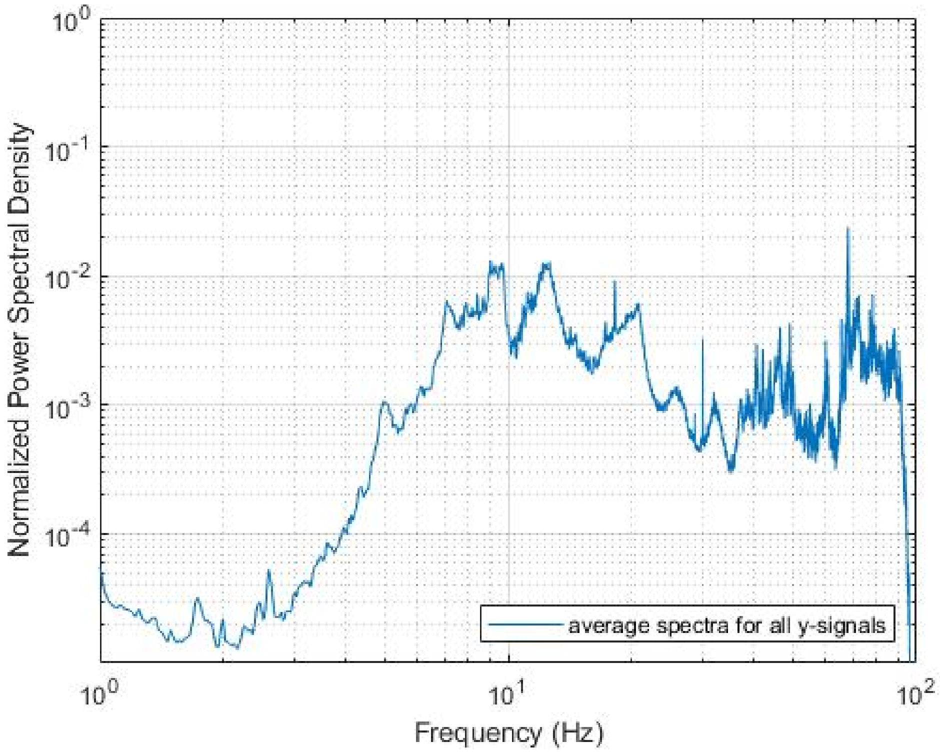

Figure 2.29: Averaged normalized Power Spectral Density for all recorded transverse signals as a function of frequency from August 28th, 08:00 – 14:00, 2019.

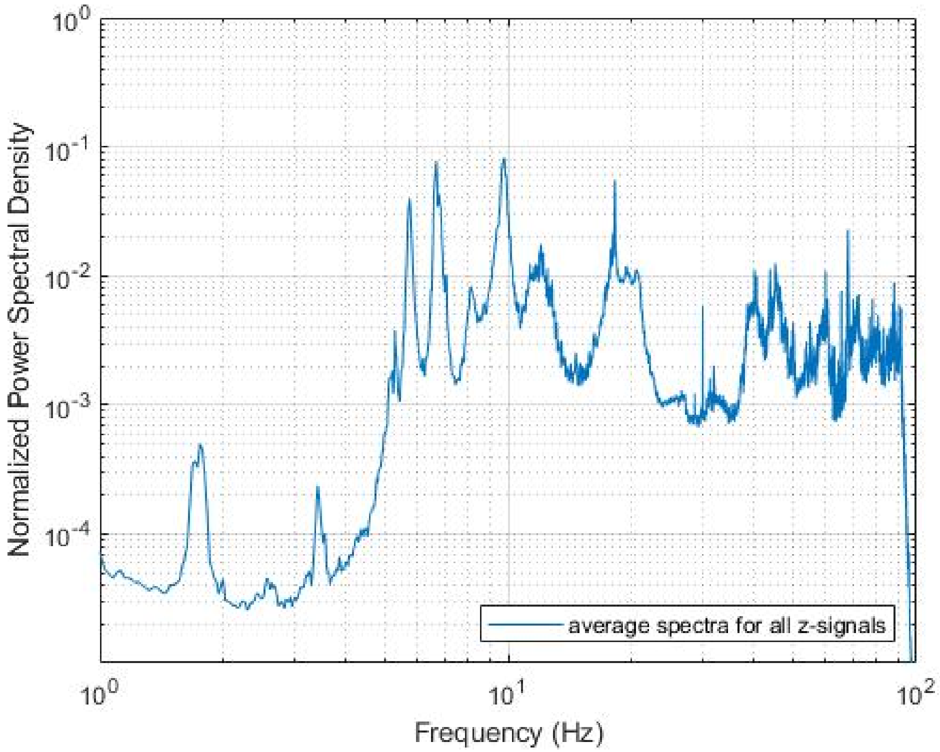

Figure 2.30: Averaged normalized Power Spectral Density for all recorded vertical signals as a function of frequency from August 28th, 08:00 – 14:00, 2019.

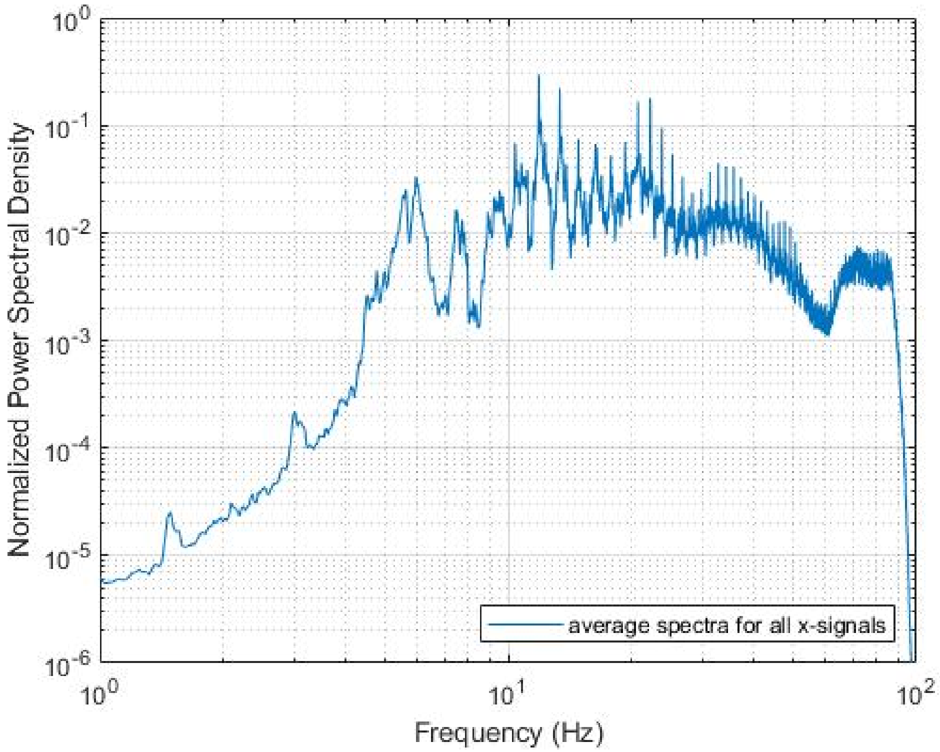

Figure 2.31: Averaged normalized Power Spectral Density for all recorded longitudinal signals as a function of frequency from August 28^{th}, 14:00 – 19:00, 2019.

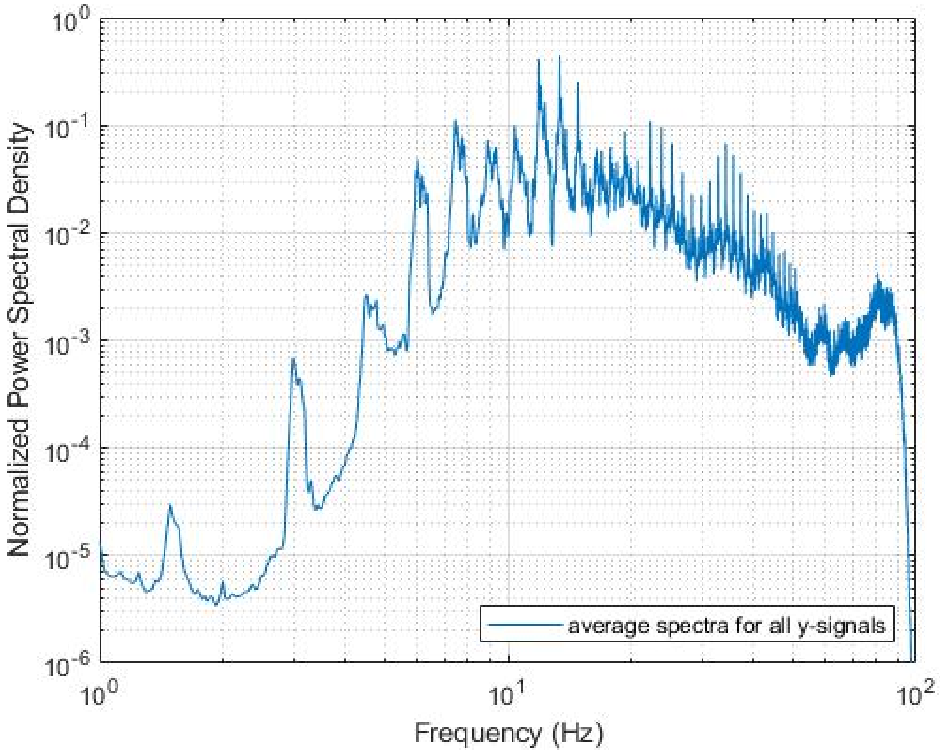

Figure 2.32: Averaged normalized Power Spectral Density for all recorded transverse signals as a function of frequency from August 28^{th}, 14:00 – 19:00, 2019.

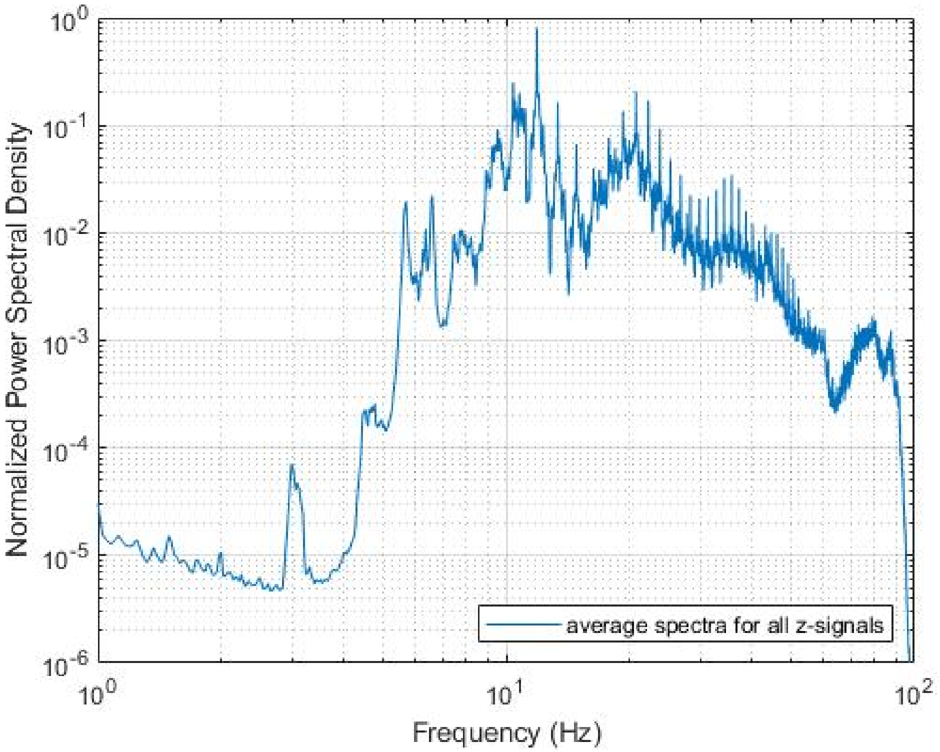

Figure 2.33: Averaged normalized Power Spectral Density for all recorded vertical signals as a function of frequency from August 28^{th}, 14:00 – 19:00, 2019.

2.4.4 Microtremor recordings in August 2019

HVSR analysis based on ambient noise measurements

Experiments have shown that the H/V spectral ratio (i.e. the ratio between the Fourier amplitude spectra of the horizontal and the vertical component of ground motion) can be successful for identifying the fundamental resonance frequency of sedimentary deposits [14] [15].

A Horizontal-to-vertical spectral ratio (HVSR) analysis based on the available ambient noise measurements on the riverbed at Steinavötn was carried out. The resulting graph is shown in Figure 2.34, where it can be seen that the fundamental resonance frequency of the gravel layers around the bridge is 2.95 Hz, based on an average of 16 hours of surface velocity data. This frequency corresponds well with the frequency peaks observed in the recorded acceleration data from the bridge during the pile-driving activities of the August 28, 2019 (see Figures 2.31 to 2.33).

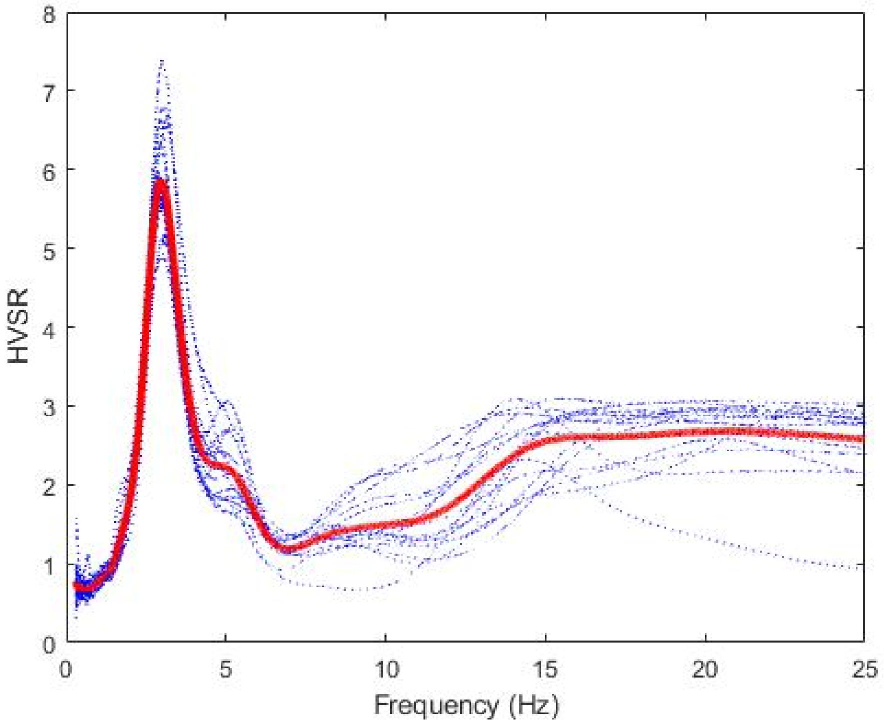

Figure 2.34: HVSR curves for the gravel/sand deposits around the bridge at Steinavötn.

Shear wave velocity and thickness of soft soil layers at the site

Prof. Bessason at University of Iceland, has published results from Spectral Analysis of Surface Waves (SASW) based on measurements done at a similar site and in the same region as Steinavötn, that is in the vicinity of Gígja river and Skeiðará river, south of Vatnajökull Glacier and slightly west of Steinavötn. Based on the similarities between those three locations, the shear wave velocity of the unfrozen sediments at Steinavötn river can be expected to be in the range of 140 m/s (measured at Gígja river) to 185 m/s (measured at Skeiðará river) from about 2 m down to a depth in the range of 10-20 m thickness (see [16]).

The fundamental period T of soil layer of thickness H, having average shear wave velocity Vs is approximately [17]:

$$T = \frac{4H}{V_s} \tag{2.2}$$

If we assume the weighted average shear wave velocity for a 16 m soil layer is 185 m/s, then the fundamental period of the soil layer will be 0.35 s according to eq. 2.2 and the fundamental frequency therefore 2.89 Hz. This is a frequency that corresponds well with the fundamental frequency obtained from the HVSR analysis. This further indicates that the thickness of the soft soil sediments at the site could be around 16 m.

The thickness of the weak sediment layers at the site has been further verified through soil-mechanical testing in the form of Borro drilling test by IRCA which took place in October 2017. The test, as practiced in Iceland, is a special version Dynamic probing, a cross over between heavy dynamic probing (DPH) and super heavy dynamic probing (DPSH) [18]. The most common dynamic probing method is the so called Standard penetration test (SPT), which is best suited for sand, clay and silt materials. The DPH and DPSH methods, are more robust and better suited for sandy gravel sites. They are not directly comparable to the SPT, but methods have been developed correlate the different approaches [19]. The IRCA DP test (see Appendix D) showed that in a penetration hole 16 m away from the bridge there was a stiff or dense layer at 14 m depth, which provided at least 4 times more resistance than the layers above. If we take the thickness as 14 m and the fundamental frequency as 2.9 Hz, then the shear wave velocity should be 162 m/s, which is within the range expected.

These results can be further used to estimate the modulus of elasiticy (E) and the shear modulus (G) of the soil assuming a reasonable Poission ratio (υ) and density of the soil (ρ). The stiffness parameters can then possibly be used for developing the boundary conditions for finite element modelling, in terms of evaluating equivalent springs to represent the resistance of the soft soil layers under the bridge (see section 4.2.1).

3 Modal Analysis and System Identification

3.1 Structural Dynamics and Modal Analysis

This section introduces the basic concepts of classical structural dynamic analysis that can be found in [20], [21], [22] and chapter 5 in [23].

3.1.1 Simple degree of freedom systems

Simple structures can be modeled as a single-degree-of-freedom (SDOF) system. A full water tank on top of a single colum a tower is a common example, along with the idealized one-story frame shown in Figure 3.1 The structure is defined by a system that consist of a mass, spring, damper and excitation force.

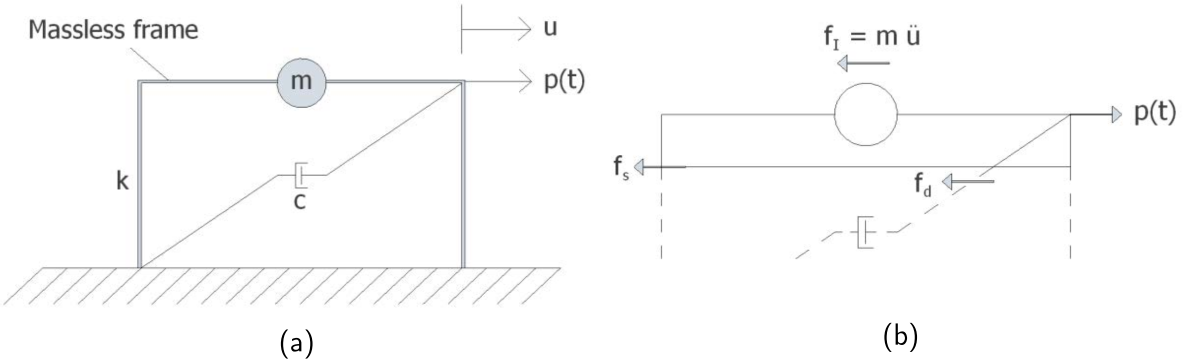

Figure 3.1: (a) Idealized one-story frame and (b) free-body diagram of the one-story frame.

By applying Newton's Second Law on the system and drawing the free-body diagram, the equation of motion is defined as:

$$m\ddot{u} + c\dot{u} + ku = p(t) \tag{3.1}$$

where m is the mass, k is the stiffness, c is the damping, $\ddot{u}$ is the acceleration, $\dot{u}$ is velocity and u is displacement.

The stiffness is based on the material properties and the cross-sectional geometry of the supporting columns. If the top beam is rigid, the lateral stiffness of each column can be estimated as ([20], page 9):

$$k = \frac{12EI}{L^3} \tag{3.2}$$

where E is the Young's modulus (modulus of elasticity), I is the moment of inertia (second moment of area) and L is the length of the element or height of the column.

The mass in this case could be taken as the sum of the mass of the top beam and half of the mass of the columns, lumped in a single mass point.

The damping value depends on the inherent material damping of the columns and the damping characteristics of the connections between foundation and column and column and beam, as will be discussed further in section 3.1.4.

The excitation force can be any dynamic force that is a function of time, for instance induced by wind, earthquake or machine. The excitation will result in a time dependent vibrational displacement response, u(t), that can also be described through velocity or acceleration.

3.1.2 Multi-degree of freedom systems

Engineering structures are, in principle, continuous structures with infinite degrees of freedom. The simple SDOF system therefore needs to be expanded into a multi-degree of freedom system (MDOF). For transparency we start by expanding the SDOF system into a two degree of freedom system shown in Figure 3.2.

For this system we can express the equation of motion in a matrix form ([20], page 345-348):

$$\begin{bmatrix} m_1 & 0 \\ 0 & m_2 \end{bmatrix} \begin{bmatrix} \ddot{u}_1 \\ \ddot{u}_2 \end{bmatrix} + \begin{bmatrix} f_{d1} \\ f_{d2} \end{bmatrix} + \begin{bmatrix} f_{s1} \\ f_{s2} \end{bmatrix} = \begin{bmatrix} p_1(t) \\ p_2(t) \end{bmatrix} \tag{3.3}$$

or in a more general matrix notation:

$$\boldsymbol{m}\ddot{\boldsymbol{u}} + \boldsymbol{f_d} + \boldsymbol{f_s} = \boldsymbol{p}(t) \tag{3.4}$$

where $\boldsymbol{m}\ddot{\boldsymbol{u}}$ represents the inertia force of the mass with $\boldsymbol{m}$ being the lumped mass matrix, $\boldsymbol{f_d}$ is the damping force and $\boldsymbol{f_s}$ is the stiffness force.

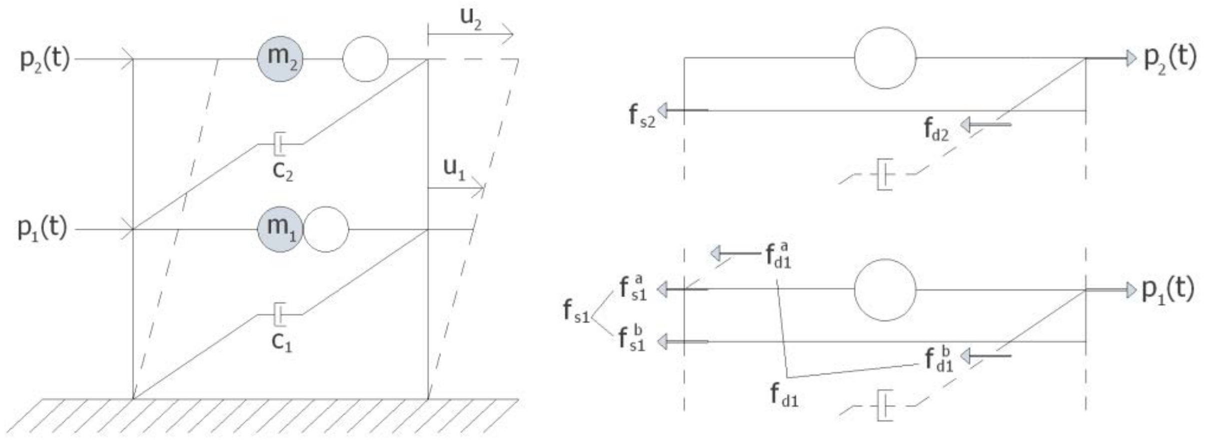

(a) (b)

Figure 3.2: (a) Two-story frame and (b) free-body diagram of the two-story frame.

The damping force and stiffness force can by found through the free body diagram as:

$$\boldsymbol{f_s} = \begin{bmatrix} k_1 + k_2 & -k_2 \\ -k_2 & k_2 \end{bmatrix} \begin{bmatrix} u_1 \\ u_2 \end{bmatrix} = \boldsymbol{ku} \tag{3.5}$$

$$\boldsymbol{f_d} = \begin{bmatrix} c_1 + c_2 & -c_2 \\ -c_2 & c_2 \end{bmatrix} \begin{bmatrix} \dot{u}_1 \\ \dot{u}_2 \end{bmatrix} = \boldsymbol{c\dot{u}} \tag{3.6}$$

Where each floor has a specific stiffness k_1 and k_2 corresponding to the numbering of m and c. We have developed a stiffness matrix, $\boldsymbol{k}$, and a damping matrix, $\boldsymbol{c}$.

The equation of motion looks the same as for the SDOF system, but it is now in matrix form and the equation is coupled through the off-diagonal terms in the damping and stiffness matrices. This simple 2DOF system can be expanded through a similar methodology to a true MDOF system, for instance using the Finite element method.

3.1.3 Free vibration and modal representation

The basic state of a dynamic system is the undamped free vibration, described with the equation ([20], page 39):

$$\boldsymbol{m\ddot{u}}(t) + \boldsymbol{ku}(t) = \boldsymbol{0} \tag{3.7}$$

Free vibration means that if the structure is pulled out of its equilibrium position it can vibrate without any external dynamic forcing ($\boldsymbol{p}(t) = 0$). A convenient start is to look at undamped vibrations, which means that the damping is taken as $\boldsymbol{c} = \boldsymbol{0}$ for the time being.

A solution to the free vibration can be described as:

$$\boldsymbol{u}(t) = q_n(t)\phi_n \tag{3.8}$$

where n is the number of degree of freedom, ϕ_n are the natural modes of the system, and $q_n(t)$ is a harmonic function, that can be written as:

$$q_n(t) = c_n e^{i\omega_n t} \tag{3.9}$$

By differentiating $q_n(t)$ twice, to get velocity and acceleration, and inserting the result into Eq. 3.9, gives:

$$\left[-\omega_n^2 \boldsymbol{m}\phi_n + \boldsymbol{k}\phi_n\right] q_n(t) = \boldsymbol{0} \tag{3.10}$$

Since the solution of $q_n(t) = 0$, meaning that there is no motion, is trivial and not useful, the contents of the bracket must equal zero. This gives the matrix eigenvalue problem:

$$\left[\boldsymbol{k} - {\omega_n}^2 \boldsymbol{m}\right] \phi_n = \boldsymbol{0} \tag{3.11}$$

This equation has a nontrivial solution if:

$$det\left[\boldsymbol{k} - {\omega_n}^2 \boldsymbol{m}\right] = \boldsymbol{0} \tag{3.12}$$

From this equation, the natural circular frequencies, ω_n, are calculated, and then the natural mode shapes, ϕ_n, can be retrieved by inserting the known natural frequencies into Eq. 3.11 and solve for ϕ_n. However, this will only give relative values for the vectors ϕ_n, that is only the shape of the vector, or the mode shape.

The vibration amplitude of a structure can be split up into modal contributions, $u_n = \phi_n Y_n$, based on the normal mode shapes of the structure. This is shown in Figure 3.3, for the first three lateral mode shapes of a typical column multiplied with a time dependent modal or generalized amplitude (Y_n) The amplitudes of the normal modes can then be superimposed to get the total displacement ([21] page 220-223):

$$\boldsymbol{u} = \phi_1 Y_1 + \phi_2 Y_2 + \cdots + \phi_n Y_n = \sum_{n=1}^{N} \phi_n Y_n \tag{3.13}$$

or, in matrix notation:

$$\boldsymbol{u} = \Phi \boldsymbol{Y} \quad \text{where} \quad \Phi = \begin{bmatrix} \phi_{11} & \cdots & \phi_{1N} \\ \vdots & \ddots & \vdots \\ \phi_{N1} & \cdots & \phi_{NN} \end{bmatrix} \tag{3.14}$$

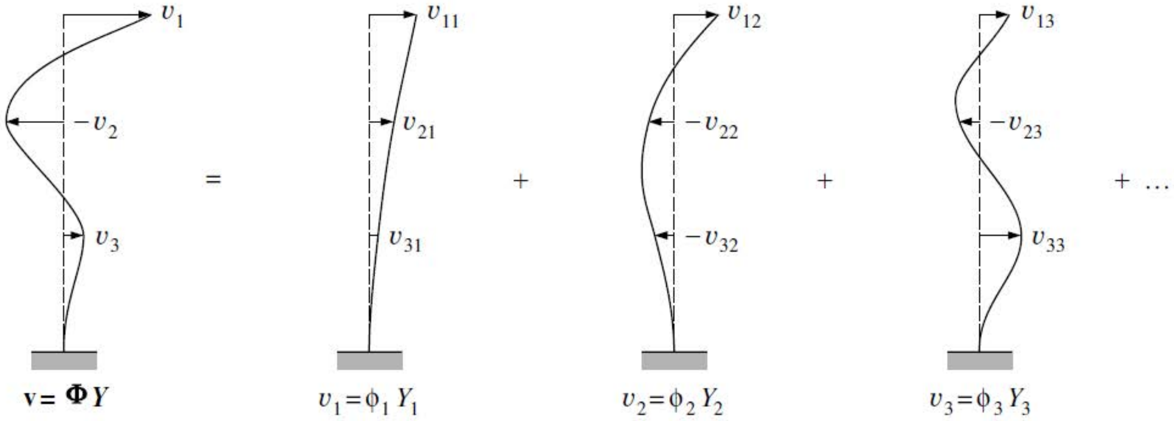

Figure 3.3: The first three lateral modes of vibration for a column ([21], page 220)

To include the modal representation into the equation of motion, the velocity, $\dot{\boldsymbol{u}}$ and acceleration vector $\ddot{\boldsymbol{u}}$ are needed, which are a derivatives of the displacement $\boldsymbol{u}$. Since the mode shapes are only functions of spatial variables but not a function of time, the time derivative does not change the mode shapes. If we now also pre-multiply each part of the equation of motion with the transpose of the mode shape matrix, then we get:

$$M_n \ddot{Y}_n(t) + C_n \dot{Y}_n(t) + K_n Y_n(t) = P_n(t) \tag{3.15}$$

where $M_n = \phi_n^T \boldsymbol{m} \phi_n$ is the modal mass, $C_n = \phi_n^T \boldsymbol{c} \phi_n$ is the modal damping, $K_n = \phi_n^T \boldsymbol{k} \phi_n$ is the modal stiffness, and $P_n(t) = \phi_n^T \boldsymbol{p}(t)$ is the modal excitation.

It can be shown ([20] & [23](chapter 5)) that the natural modes satisfy the following orthogonality conditions, when $\omega_n \neq \omega_r$

$$\phi_n^T \boldsymbol{k} \phi_r = 0 \text{ and } \phi_n^T \boldsymbol{m} \phi_r = 0 \tag{3.16}$$

This orthogonality also implies that the square matrices for the stiffness and mass are diagonal. These relations can then be used to uncouple the equation of motion, as all off diagonal terms in the equation of motion (Eq. 3.15) will vanish and each n^th equation can be treated as a separate SDOF system. To obtain the total response of the MDOF system, the n SDOF equations are solved and their effects superimposed.

As previously mentioned earlier, the mode shapes derived from Eq. 3.11 have a relative amplitude. This means that the modes can be scaled, or normalized, to our liking. In theoretical usage and in computer programs the modes shapes are generally scaled to give a modal mass, $M_n = 1$, for all modes, which in turn gives a modal stiffness, $K_n = \omega_n^2$.

The damping matrix can not be determined in the same semi-definite way as the mass- and stiffness matrix, which are based on known physical parameters, such as material properties and structural geometry. It is therefore no guarantee that the modal damping matrix truly fulfils the same orthogonal properties as the mass and stiffness matrix. To include damping at this point, it is however generally assumed that C_n can be expressed with the same orthogonality condition as K_n and M_n, and there are convenient mathematical models such as the Rayleigh damping model that assumes that damping can be written as a linear combination of stiffness and mass [20]. This mathematical representation has however, limited relation to real damping properties.

Equation 3.15 is often divided by the generalized mass to form the equation:

$$\ddot{Y}_n(t) + 2\xi_n \omega_n \dot{Y}_n(t) + \omega_n^2 Y_n(t) = \frac{P_n(t)}{M_n} \tag{3.17}$$

where ξ_n is the critical damping ratio, defined as:

$$\xi_n = \frac{C_n}{2M_n\omega_n} \tag{3.18}$$

It is often more convenient to express the equation of motion in this way, through the natural frequency and the critical damping ratio directly, because they are variables that can be measured experimentally or estimated with good precision. This representation also provides means to implement the modal damping directly into the equation of motion in modal form, without creating a damping matrix.

3.1.4 Damping

Damping describes the ability of a structure to dissipate kinetic (or vibrational) energy, that is change it into some other form of energy such as thermal energy or radiation. In the area of civil engineering the damping forces are usually small compared with the elastic and inertia forces. All the same, they can have a great influence on structural behaviour. Damping can control vibration response amplitudes and it can determine the borderline between dynamic stability and instability.

Damping can be generated by several mechanisms. They can be grouped into three main sources of damping:

- Internal energy dissipation of materials (Material damping)
- Friction, impacting and rubbing between parts of a structure (Structural damping)
- Fluid dynamic drag (Fluid damping)

Damping cannot be described exactly in mathematical terms. In fact, damping established by different sources generally call for different modelling description. Therefore, simplified mathematical models are used, which in many cases give satisfactory results. The classical Linear velocity dependent viscous damping model is the most common one.

If a SDOF system is subjected to a harmonically varying load $p(t)$, with a amplitude, p_0, and a circular frequency ω, then it can be shown ([21], page 36-37) that the viscously damped total response can be written as:

$$\begin{aligned} u(t) = & \left[A\cos\omega_D t + B\sin\omega_D t\right] e^{-\xi\omega_n t} \\ & + \frac{p_0}{k}\left[\frac{1}{\left(1-\beta^2\right)^2 + (2\xi\beta)^2}\right]\left[\left(1-\beta^2\right)\sin\omega t - 2\xi\beta\cos\omega t\right] \end{aligned} \tag{3.19}$$

Where we have the frequency ratio $\beta = \omega/\omega_n$, the damped natural frequency, $\omega_D = \omega_n\sqrt{1-\xi^2}$ and the stiffness k. The coefficients A and B, depend on the initial conditions of the motion. From Eq. 3.19 we see that the damping controls both the exponential decay of the transient part of the motion and the amplitude of the steady state motion through the response function:

$$\rho = \frac{p_0}{k}\left[\frac{1}{\left(1-\beta^2\right)^2 + (2\xi\beta)^2}\right] \tag{3.20}$$

This function is composed of the static displacement ($\rho_0 = p_0/k$) and the so-called dynamic magnification factor (within the bracket). Buildings, as well as most structures are under-damped, i.e. $\xi << 1$. When a structure is under-damped the free vibration decays out with time as the structure slowly looses its energy until the oscillation stops, as shown in Figure 3.4 for the free vibration of three SDOF systems with the same natural frequency, but different critical damping ratio.

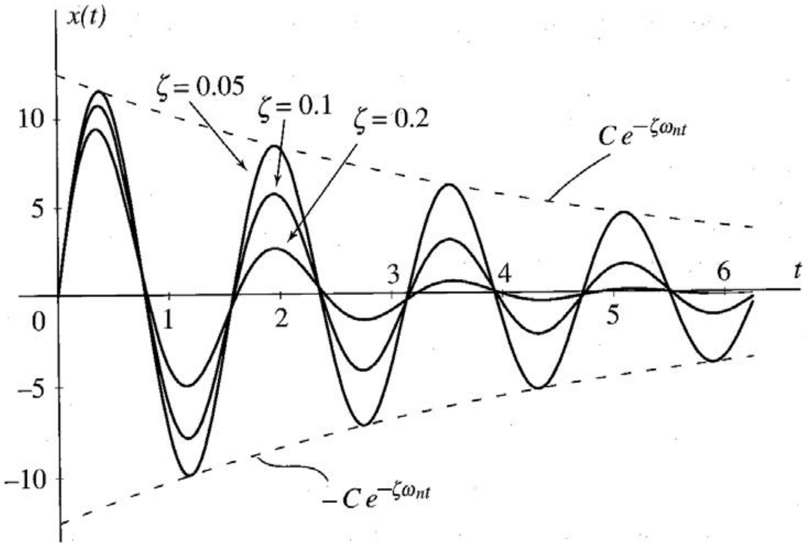

Figure 3.4: Free vibration response of underdamped systems with different damping ratios ([24] ,page 91).

There are many ways of determining the damping ratio of a system. Two classical experimentally based methods will be briefly mentioned here, as they demonstrate the basics for various other approaches. Those are the Resonant Amplification method ([21], page 53) and the Free Vibration Decay method ([25]), page 35).

The Resonant Amplification Method

The Resonant Amplification Method ([21], page 53) uses the amplitude of the steady-state response and/or the width of the amplitude response function, ρ, as demonstrated in Figure 3.5, estimating the critical damping ratio as:

$$\xi = \frac{\rho_0}{2}\rho_{max} \text{ or } \xi = \frac{\beta_2 - \beta_1}{\beta_2 + \beta_1} \qquad (3.21)$$

where $\rho_0 = \frac{p_0}{k}$ is the static displacement, p_{max} is the peak displacement and β is the frequency ratio ([21], page 53-55).

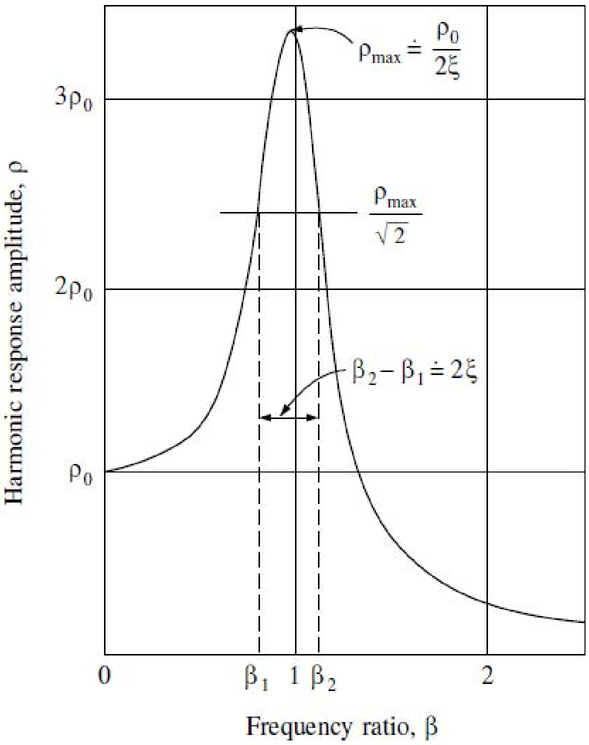

Figure 3.5: Frequency-response curve for moderately damped system ([21], page 53).

The Free Vibration Decay Method

The Free Vibration Decay Method ([25], page 35) is the simplest and probably most used method for measuring damping. For this method, one has to displace or excite a system and then release the excitation. This will result in a time series of amplitude decay similar to the one shown in Figure 3.4. The next step is to evaluate the free vibration response. The rate of decay of oscillation is the factor of interest. By using two peak amplitude values (x_i and x_j) and the number of oscillations, N, between them, one can determine the critical damping ratio of the system by using the following relation:

$$\xi = \frac{1}{2\pi} \ln\left(\frac{x_i}{x_j}\right) \frac{1}{N} \tag{3.22}$$

Another possibility would be to fit an exponential function to the decay curve as shown in Figure 3.4.

3.2 Operational Modal Analysis and System Identification

This section, which is mainly based on [23] (chapter 5), provides a brief introduction to some key aspects of operational modal analysis (OMA).

In an OMA identification process, we generally want to estimate either correlation functions or spectral densities and then from these functions extract the physical information about the system, that is, the modal parameters for each mode (the mode shape, the natural frequency, and the damping). Normally random responses are Gaussian distributed, and therefore all the relevant modal information in the signals is concentrated in the second order properties, which are described completely by correlation functions or spectral densities. Both functions carry the same information because they form a Fourier transform pair, with correlation functions describing the system in the time domain and spectral density functions describing the system in the frequency domain.

The definition and realization of correlation functions and spectral density functions are described and discussed in detail in [23]. The autocorrelation and cross-correlation functions basically describe the correlation between two points at time lag t, either within the same time-series (auto) or two different time-series (cross) It must be expected that if the points are close, then the correlation is high, and as the separation between points increases then the correlation is lower. The basic definition of the cross-correlation function is given as

$$R_{xy}(\tau) = E[x(t-\tau)y(t)] = \frac{1}{T}\int_0^T x(t)y(t+\tau)dt \tag{3.23}$$

The cross spectral density function for two time series x(t) and y(t) is defined as the Fourier transform of the cross-correlation function $R_{xy}(\tau)$:

$$G_{xy}(\omega) = \frac{1}{2\pi}\int_{-\infty}^{\infty} R_{xy}(\tau)e^{-i\omega\tau}d\tau \tag{3.24}$$

Parseval's theorem gives us the interesting relation between the correlation function, spectral density and the signal variance:

$$R_{xx}(0) = E[xx] = \int_{-\infty}^{\infty} G_{xx}(\omega) d\omega = \sigma_{xx}^2 \tag{3.25}$$

The aim of OMA is to obtain information about structural properties, either through time domain identification based on the correlation functions, or through frequency domain identification based on the spectral densities. Time domain methods generally use input time functions in the form of "free decays" represented by correlation functions, and normally use fitting techniques based on parametric regression models of the data. In this report, the focus is on the frequency domain identification methods, in particular the FDD approach and variants thereof [23], described briefly in section 3.3.

Pre-processing

Before initiating system identification, the signals generally need some pre-processing. Such as detrending to remove any offsets in the data or linear trends. We also may need to classify the signals, or determine which signals are most suitable for OMA. Basic assumption in OMA is that the system is invariant and the response stationary. Lack of stationarity is mainly due to changes in the loading conditions. However, the requirement for stationarity is not very strict, as the methods used normally work under weakly non-stationary conditions.

It is generally desirable to filter the data to remove both irrelevant high and low frequency components from the data that might distract the SI algorithms applied. It can also be desirable to either down-sample or up-sample the data, depending on the sampling frequency, the frequency range and resolution required. The various steps and aspects of signal processing are thoroughly discussed in chapter 8 in the book by Brinker and Ventura [23]. What is important in this context, is to apply the same pre-processing steps systematically to all channels of the data used.

Frequency-Domain Identification

In the frequency domain the identification methods are based on the fact that each mode has a small frequency band where a single mode dominates, thus, the frequency domain provides the advantage of a "natural modal decomposition" simply by considering the different frequency bands where different modes dominate. This is the main advantage of the frequency-domain approach, and the main idea behind the classical basic frequency domain approach, which assumes that any structural mode that is reasonably lightly damped is only influencing the response of the structure in a narrow frequency band around the natural frequency of the considered mode. The drawback of the frequency domain is that the spectral density estimates may suffer from bias, whereas the time domain modal extraction is based on information that is nearly bias free (see [23] chapter 10.9).

Considering the structural response y(t) in a frequency band dominated only by a single mode, the response is given by

$$\boldsymbol{y}(t) = \boldsymbol{a} q(t) \tag{3.26}$$

where $\boldsymbol{a}$ is the mode shape and $q(t)$ is the modal coordinate of the mode. Using the definition of the correlation function (CF) matrix given by

$$\boldsymbol{R}(\tau) = E\left[\boldsymbol{y}(t)\boldsymbol{y}(t+\tau)^T\right] = \boldsymbol{a}\boldsymbol{E}[q(t)q(t+\tau)]\boldsymbol{a}^T = R_q(\tau)\boldsymbol{a}\boldsymbol{a}^T \tag{3.27}$$

where $R_q(\tau)$ is the autocorrelation function of the modal coordinate. The spectral density (SD) matrix $\boldsymbol{G}_y(f)$ of the response, defined as the Fourier transform of the correlation function matrix, is then

$$\boldsymbol{G}_y(f) = G_q(f)\boldsymbol{a}\boldsymbol{a}^T \tag{3.28}$$

where $G_q(f)$ is the auto spectral density function of the modal coordinate. As it appears, this gives us a spectral density matrix of rank one, and any row or column of the spectral matrix is proportional to the mode shape vector. This means that for this case, we can take any column (channel) in the spectral density matrix as an estimate of the mode shape, and the mode shape estimates could then be averaged over channels/columns in the spectral matrix.

Cases where this approach can be used effectively are when only one mode is active or when a considered mode is well separated from all other modes, so that the influence from the surrounding modes can be neglected. The mode can be considered "well separated" from other modes when the minimum frequency distance to any other mode is much larger than the bandwidth $B = 2\xi_n f_n$ of the considered mode nr.n. Although this approach seems simple and effective if these assumptions are fulfilled, a more general approach is needed to be able to treat problems with closely spaced modes and random noise.

Frequency-Domain Decomposition (FDD)

The Frequency-Domain Decomposition (FDD) technique is based on singular value decomposition (SVD) of the spectral density matrix [26]. The idea of the technique can be introduced by extending Eq's. 3.26 to 3.28 to multi normal modes and modal coordinates giving the SD matrix:

$$\boldsymbol{G}_y(f) = \boldsymbol{A}\boldsymbol{G}_q(f)\boldsymbol{A}^T \tag{3.29}$$

where $\boldsymbol{A}$ is the mode shape matrix $\boldsymbol{A} = [\boldsymbol{a}_1, \boldsymbol{a}_2, \ldots]$ and $\boldsymbol{G}_q(f)$ is the spectral density matrix of the modal coordinates $\boldsymbol{q}(t)$.

If we now assume that the modal coordinates are uncorrelated, that is, the off-diagonal elements of the correlation function matrix of modal coordinates $\boldsymbol{R}_q(\tau)$ is zero, then the spectral density matrix $\boldsymbol{G}_q(f)$ of the modal coordinates is both diagonal and positive valued. Further, since we know that the SD matrix is Hermitian and that some complexity might be present in the mode shapes, we need to use the Hermitian instead of the transpose. The final form of the SD matrix is then:

$$\boldsymbol{G}_y(f) = \boldsymbol{A}\left[g_n^2(f)\right]\boldsymbol{A}^H \tag{3.30}$$

where $g_n^2(f)$ are the auto spectral densities (diagonal elements) of $\boldsymbol{G}_q(f)$. A decomposition such as that given by Eq. 3.30 can be performed by taking an SVD of the SD matrix, which for a complex, Hermitian, and positive definite matrix, takes the form:

$$\begin{aligned}\boldsymbol{G}_y(f) &= \boldsymbol{U}\boldsymbol{S}\boldsymbol{U}^H \\ &= \boldsymbol{U}\left[s_n^2\right]\boldsymbol{U}^H\end{aligned} \tag{3.31}$$

It follows directly that the singular values s_n^2 in the diagonal matrix $\boldsymbol{S}$ should be interpreted as the auto spectral densities of the modal coordinates, and the singular vectors, that is the columns in $\boldsymbol{U} = [\boldsymbol{u}_1, \boldsymbol{u}_2, \ldots]$ should be interpreted as the mode shapes. However, because the SVD given by Eq. 3.31 does not correspond completely to the theoretical decomposition of the SD matrix, the FDD is always an approximate solution.

In the case of well-separated modes and light damping, the SD matrix approximately decomposes as given by Eq. 3.31. This is also true when the modes are not well separated if the modal coordinates are uncorrelated.

For closely spaced modes the mode shapes are estimated based the singular vectors of the SVD of the modal decomposition of the SD matrix, as discussed in [23], section 10.3.3. Introducing the main rule in FDD mode shape estimation: Any mode shape in FDD should be estimated as the first singular vector at a frequency line where the corresponding singular value is dominating. It should be noted that the complexity of the mode shapes estimated by the FDD technique is heavily biased and thus should not be used for physical interpretations.

3.3 OMA using the ARTeMIS Modal Pro software

The ARTeMIS Modal Pro [27] was used to perform Operational Modal Analysis (OMA) on selected ambient acceleration time series. Two types of OMA estimation methods were used for the system identification, the Frequency Domain Decomposition (FDD) and the Enhanced Frequency Domain Decomposition (EFDD).

Both techniques are derived from the Frequency Domain Decomposition technology utilizing the singular value decomposition of the estimated spectral densities of the measured response. They are based on peak-picking in frequency domain, using either automatic picking or manual picking using the mouse. Once picked, the mode shapes are ready for immediate animation and a stabilization diagram shows the stabilized modes identified. The EFDD method works just like the FDD, except the EFDD identifies the top part of the auto-spectral density of the Single-Degree-Of-Freedom (SDOF) system of the picked mode, based on a Modal Assurance Criterion (MAC). By transforming the auto-spectral density SDOF function to a time domain correlation function by inverse FFT, the natural frequency and damping ratio are obtained by least squares estimation in the time domain. Mode shapes are obtained by averaging directly in the frequency domain using the identified part of the auto-spectral function and the corresponding singular value decomposition of the spectral matrices, as described in section 3.2.

The Operational Modal Analysis made with ARTeMIS is geometry driven. Measurement channels in use must be tied to a geometry node, and mode shapes and operating deflection shapes need a realistic test geometry for proper animation. The first step in the modelling process is therefore to produce a realistic test geometry via a simple model of the structure.

Figures 3.6-3.7 show the bridge geometry modelled in ARTeMIS as well as the positions of the measurement channels, or the three perpendicular components from each of the five accelerometers used, identified as a1 through a5. Figure 3.6 shows how the sensors were placed during the tests in July 2019, whereas Figure 3.6 illustrates how the sensors were placed during the test in August 2019. Note, that only half of the bridge geometry was modelled in ARTeMIS since the accelerometers were only placed on the eastern half of the bridge.

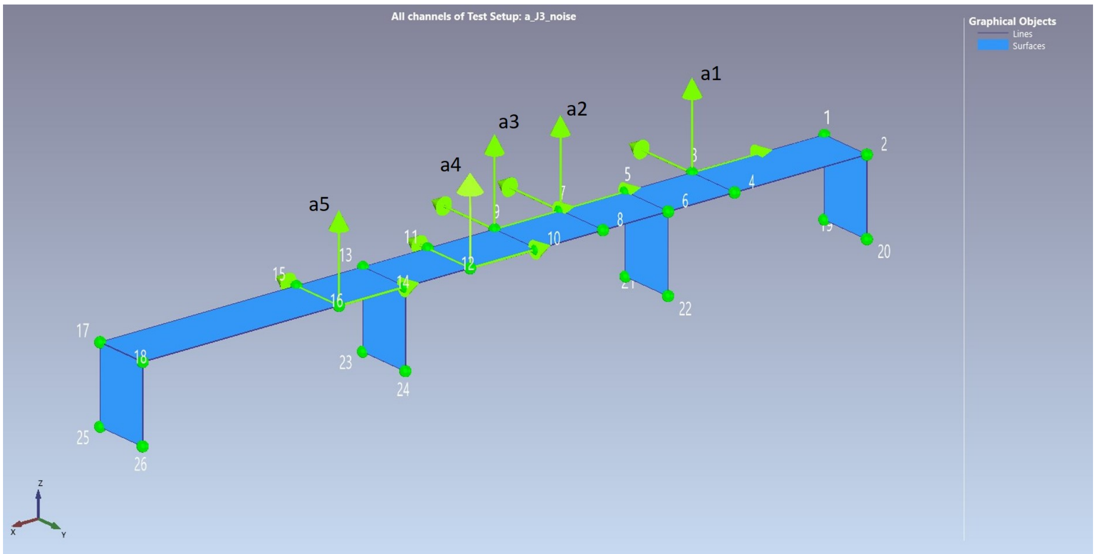

Figure 3.6: Sensor and measurement channels positions in July. (east-end of the bridge to the right, mid-span to the left).

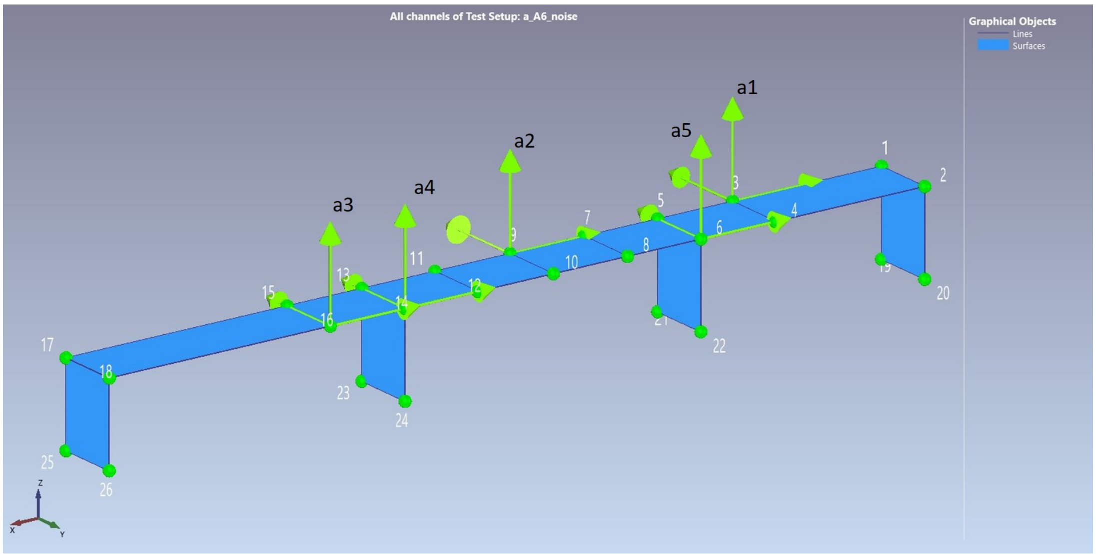

Figure 3.7: Sensor and measurement channels positions in August. (east-end of the bridge to the right, mid-span to the left).

In all cases the data series selected only represented the ambient environmental excitation, without any notable acceleration spikes from nearby traffic or other human activities in the recorded response. The three different data series selected were: (a) 10 minute data segment from August 2019, (b) 1 hour data segment from August 2019 and (c) 30 minute data segment from July 2019. The signal processing was the same for each of the time series. Detrending was enabled to remove the mean value and any linear trend from the processed measurements. The signal was then decimated to reduce the Nyquist frequency from 100 Hz to 33.33 Hz. Finally a high pass filter of 2^{nd}-degree, with the lower cut-off frequency of 1 Hz, was applied.

The results from the three different data series studied are listed and compared in Table 3.1. Appendix E contains plots of Singular values of the spectral matrices of all the data series 1) before the peak picking, 2) after peak picking for the FDD analysis and 3) after peak picking for the EFDD analysis. Figure 3.8 gives an example of a spectral matrix for the 10 min series where possible selection of peaks has been marked.

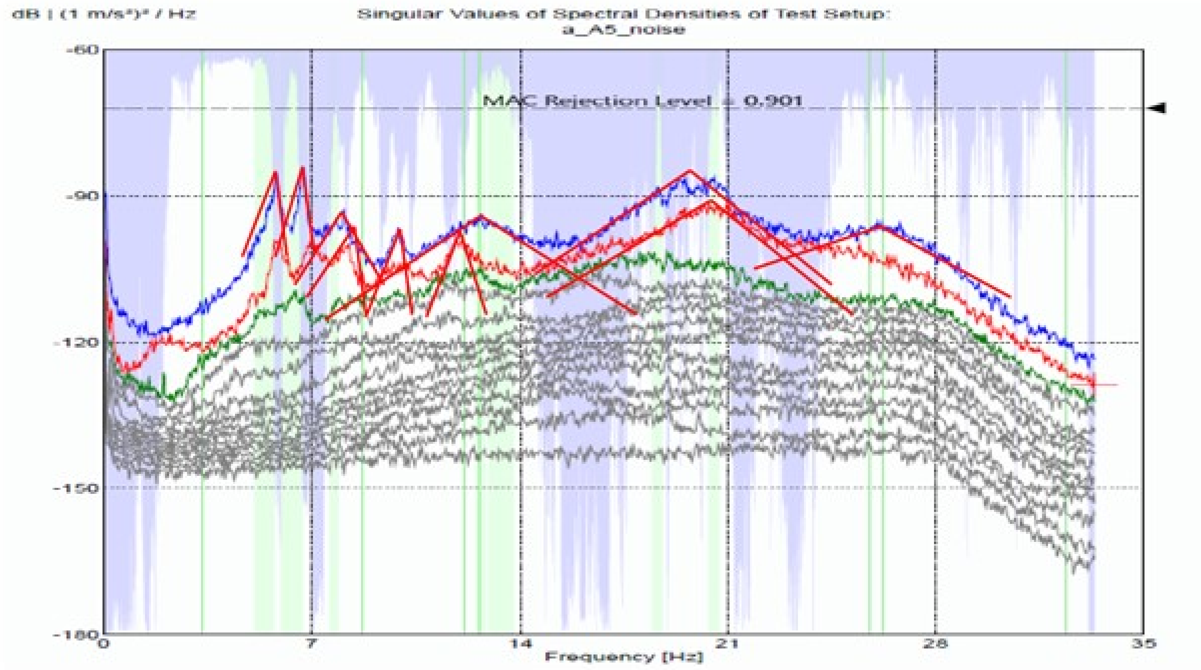

Figure 3.8: The singular values of the spectral matrix [dB rel. to m^2/s^3] as a function of frequency [Hz] as evaluated by ARTeMIS for a test-setup using 10-minute data segment from August 2019. Potential modes are drawn as open red triangles.

As can be seen from table Table 3.1, at least up to 10 modes can be identified, but some variability is seen in both the modal frequencies and the damping ratios identified, depending on the data set used in the analysis. It is also not necessarily exactly the same higher modes that are identified in the different data sets. This difference is based on the peak picking choices made by the user, or what peaks and modes stand out in the graph showing the singular values of the spectral matrix.

The difference in the complexity of the same modes between data sets is also noteworthy, mainly indicating that the quality of identification differs between the three data series used. For two spectral peaks picked from the SD plot, the EFDD method gives zero damping, indicating that the frequency picked does not represent a real mode of vibration, but could be linked to some external noise.

Table 3.1: Natural frequencies, f, complexity, C, and damping, ζ, of the 3 time series.

August - Ambient noise (10min)					August - Ambient noise - (1hour)					July - Ambient noise (30min)				
OMA - FDD		OMA - EFDD			OMA - FDD		OMA - EFDD			OMA - FDD		OMA - EFDD		
f [Hz]	C [%]	f [Hz]	ζ [%]	C [%]	f [Hz]	C [%]	f [Hz]	ζ [%]	C [%]	f [Hz]	C [%]	f [Hz]	ζ [%]	C [%]
5.762	23.275	5.786	0.907	13.692	5.794	6.974	5.785	0.966	3.879	5.697	1.546	5.71	0.931	1.986
6.673	2.997	6.695	1.156	10.925	6.706	2.626	6.695	1.168	10.536	6.641	2.933	6.623	1.047	3.207
8.073	12.837	8.07	0.879	15.258	8.171	26.739	8.153	0.678	31.47	8.203	24.521	8.193	0.834	14.807
					9.18	22.04	9.196	1.023	34.43					
9.896	17.026	9.877	1.257	29.637	9.733	2.323	9.714	1.114	7.477	9.603	18.535	9.576	1.808	20.551
					10.124	24.296	10.116	0.341	16.511					
										11.165	92.708	11.147	1.538	80.814
					11.589	5.132	11.589	0	5.132					
11.979	52.838	11.968	0.146	64.507						11.979	5.689	11.906	1.817	11.274
12.695	59.967	12.684	2.356	71.937	12.37	13.969	12.32	0.806	21.889					
					13.314	52.711	13.313	0.34	72.522	13.477	26.284	13.457	0.538	45.858
15.234	42.439	15.225	0.218	46.975										
										17.676	12.737	17.788	2.227	21.106
18.62	31.857	18.598	0.707	48.933						18.75	15.369	18.848	0	21.937
19.564	20.564	19.496	0.998	41.227										
20.54	25.801	20.509	0.931	33.399						20.573	11.475	20.535	0.47	10.878

Table 3.2: Natural frequencies, f, complexity, C, and damping, ζ, of the 1-hour series, x-,y-, and z-directions.

August - Ambient noise (1hour)-X					August - Ambient noise (1hour)-Y					August - Ambient noise (1hour)-Z				
OMA-FDD		OMA-EFDD			OMA-FDD		OMA-EFDD			OMA-FDD		OMA-EFDD		
f [Hz]	C [%]	f [Hz]	ζ [%]	C [%]	f [Hz]	C [%]	f [Hz]	ζ [%]	C [%]	f [Hz]	C [%]	f [Hz]	ζ [%]	C [%]
5.371	0.398	5.524	5.369	0.085	5.241	88.857	5.233	0.508	96.632					
5.827	1.201	5.814	1.09	2.29						5.794	0.129	5.737	0.818	55.111
6.673	89.935	6.654	0.821	70.542	6.999	26.533	7.153	3.571	31.806	6.706	0.053	6.697	0.971	0.012
8.171	15.508	8.221	3.624	11.184						8.171	1.758	8.117	2.422	0.526
					9.212	1.973	9.212	0	1.973					
9.766	13.002	9.733	1.507	8.916						9.733	0.344	9.758	2.698	0.626
					10.579	8.324	10.658	2.675	1.937					
11.849	7.812	11.599	0.218	80.105						11.589	2.099	11.792	1.422	0.13
12.174	12.753	12.423	5.744	7.509	12.598	24.121	12.593	6.107	24.956	12.37	0.442	12.362	0.327	2.855
										13.346	16.594	13.333	0.753	31.617
16.341	4.24	16.956	0.399	92.215										
							17.651	1.864	51.43					
										18.555	18.589	18.546	0.995	11.837
					19.629	54.414				19.368	27.21	19.362	0.921	36.694
20.54	51.622	20.453	1.258	58.582	20.898	12.025	20.462	3.313	20.827	20.54	34.183	20.525	0.667	30.756
26.823	23.713	26.642	1.498	14.279	25.456	4.636	26.604	0.756	11.04					

It was of interest to investigate the effects from each component of motion on the modal analysis. Therefore, the 1-hour data series from August 2019, was split into the longitudinal (x), transverse (y) and vertical (z) components of motion. Then the set of each component of motion, from the five measurement positions was analysed, 5 channels at a time, using both the FDD and the EFFD method. The results are compiled in table Table 3.2. What is interesting is to view the modes identified in view of the complexity of the modes. Then it is seen that the first mode has the least complexity in the x-data set. Actually, the x-component shows two modes between 5 and 6 Hz, the lower of which is possibly also seen in the y-data set, but the higher one is seen in the z-data. This fact, that there may be closely spaced modes in the different components, complicates the general identification. This frequency shift observed in the x- and y-data may be related to soil-structure interaction. Otherwise the x- and z-data show more or less the same modes, of those the complexity is always lower in the z-data set. Also there is a mode at 16 Hz in the x-data set, which is not observed in the z-data set. The y-data set shows somewhat different frequencies than the other components, such as the mode at 10.6 Hz which is not seen in the x- and z-data.

3.4 OMA using a MATLAB based toolbox

An FDD analysis MATLAB toolbox developed by Rune Brincker and introduced in [23] was used for system identification of the same three data series that were selected for the ARTeMIS OMA analysis before, i.e. (a) a 10 minute data segment from August 2019, (b) a 1 hour data segment from August 2019 and (c) 30 minute data segment from July 2019. In all cases the data series only represented the ambient environmental noise, without any notable acceleration spikes from nearby traffic or other human activities.

It was decied to focus the analysis on the first 5 modes seen in a plot of the singular values of the SD matrix. To estimate these five modes an appropriate frequency band has to be selected. Since the data is recorded by five sensors only, it is not feasible to attempt to evaluate all five modes in one run. Therefore, first we evaluate the two lowest modes, in the band between 5 Hz and 7 Hz. Then the next three between 7 Hz and 13 Hz. Then the approximate frequencies of each mode are selected as well the appropriate spectral bandwidth for each mode and the number of valid decay points in the correlation function for each mode. The identification was carried out based on the half spectrum matrix estimated with 1025 frequency lines.

The correlation function is found by taking the modal coordinate estimated in the frequency domain by modal filtering back to time domain by inverse discrete Fourier transform. The decay of the correlation function is used to estimate a SDOF system fit that gives a value for the critical damping ratio. When the appropriate choices have been made the MATLAB script can be run. The process in the analysis is roughly the following:

- Modal decomposition is carried out with the mode shapes estimated as the first singular vector as the first singular vector at the initial frequencies over a frequency band centered at the initial frequencies.
- Each modal coordinate is then taken back to time domain by inverse discrete Fourier transform, and the poles estimated from the corresponding correlation function using ITD on each single channel SDOF free decay (forceing the algorithm to return only one pole).

All the data sets were analysed taking as reference the same five approximate initial frequencies. These frequencies do not necessarily fall exactly at the peak of each of the spectral peaks in seen in the singular value SD matrix plots, but the initial frequencies must be chosen in such a way that a reasonable modal decomposition is obtained for all data sets tested.

Table 3.3 shows the id-parameters chosen for each data set based on the singular values of the SD matrices displayed in Figure 3.9.

Table 3.3: ID-parameters for the FDD analysis, shown for each data segment tested.

Data: 10-minuts August 2019			Data: 1-hour August 2019			Data: 30-minuts July 2019		
Initial freq. (Hz)	Decay points (Nr.)	Band width (Hz)	Initial freq. (Hz)	Decay points (Nr.)	Band width (Hz)	Initial freq. (Hz)	Decay points (Nr.)	Band width (Hz)
5.8	100	0.8	5.8	100	0.6	5.7	100	0.6
6.7	100	0.8	6.7	100	0.6	6.6	100	0.6
8	100	1	8.2	100	0.6	8.2	100	1
9.8	100	2	9.7	100	0.6	9.6	100	1.5
12.7	100	2	12.1	100	0.9	11	100	1

The following graphs and tables show the analysis process and results for each of the selected data sets. The results are collected and displayed for each of the analysed data sets, (a) 10 minute data segment from August 2019, (b) 1 hour data segment from August 2019 and (c) 30 minute data segment from July 2019.

Figure 3.9 shows the singular values SD matrix for all the data channels included in the analysis for each of the selected data segments.

Figures 3.10 and 3.11 show the singular values SD matrix for the 5 modes identified and included in the analysis for each of the selected data segments. As it appears in Figure 3.10 the FDD clearly separates the first two modes, where as the identification of modes 3, 4 and 5 shown in Figure 3.11 is not as clear in all cases as for the first two modes. The three higher modes are actually clearest in the July data, which indicates somewhat different circumstances during daytime in July and night time in August.

The identification of the first mode shown in Figure 3.10, is also seen to be confused by what is believed to be some slight difference or shift in the spectral frequency of the lowest mode between different components of motion (x, y z). This was also seen in ARTeMIS for the analysis of the x-component (see Table 3.2) and will be investigated further in section 3.5.

Figures 3.12 to 3.16 show the autocorrelation functions found by taking each modal coordinate estimated in the frequency domain through modal filtering back to the time domain by inverse discrete Fourier transform. The free decay fit on the SDOF systems estimated by ITD (Ibrahims Time Domain identification technique [23]) are shown by the solid lines. As can bee seen, the number of decay points specified is a key for a reliable estimation of damping. As is an appropriate choice of the frequency bandwidth parameter to be able to properly isolate each spectral peak as a SDOF system.

For the most part the correlation functions are seen to be well behaved, but in some cases a minor beating phenomenon is noticeable, indicating a slight coupling with a secondary frequency. This can partly be seen for mode 1 (Figure 3.12), mode 3 (Figure 3.14) and mode 5 (Figure 3.16).

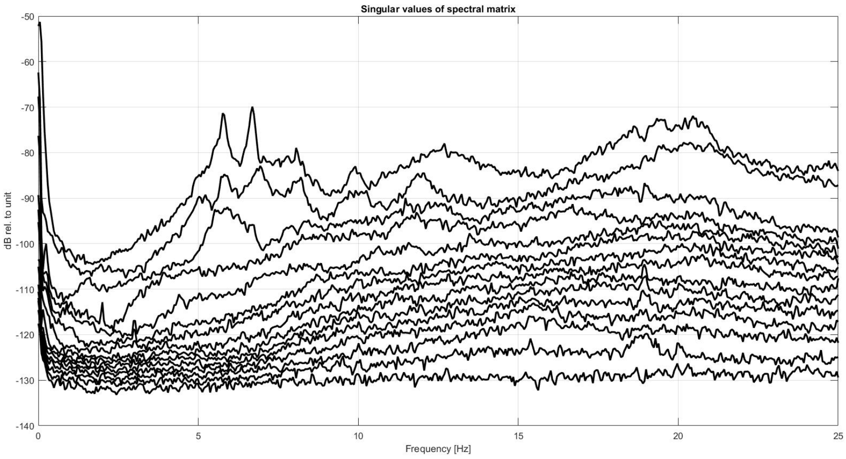

(a) 10 min. series in August 2019.

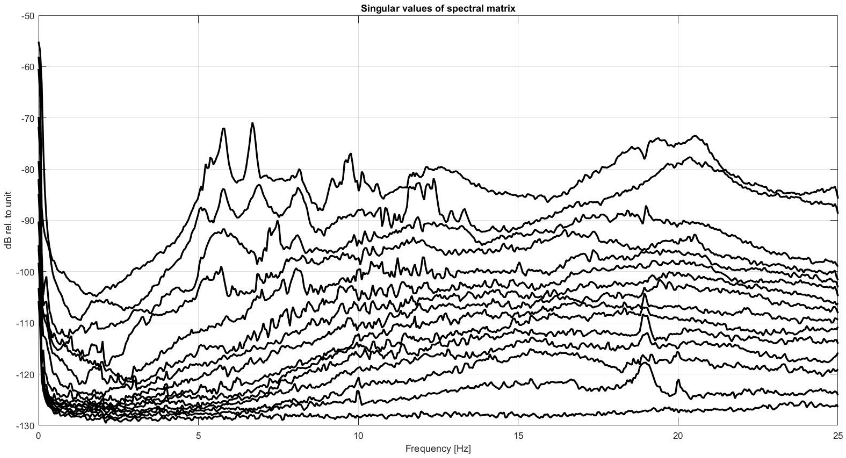

(b) 1 hr. series in August 2019.

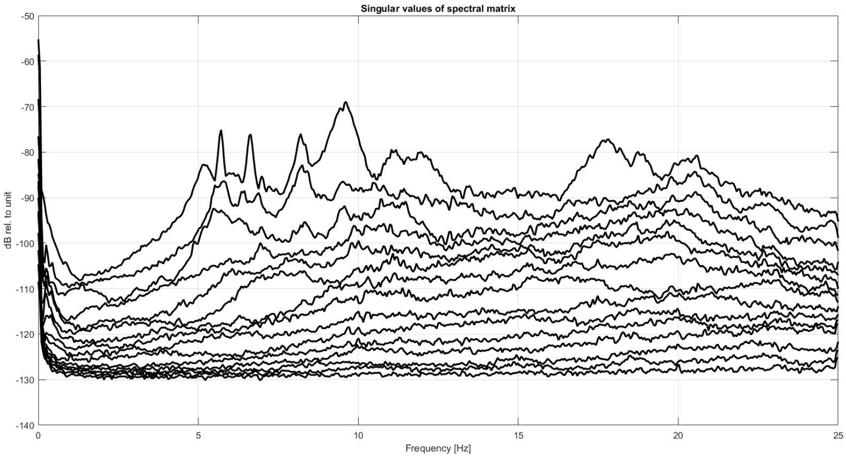

(c) 30 min. series in July 2019

Figure 3.9: The singular values of the spectral matrix ([dB rel. to m^2/s^3] as function of frequency [Hz]) for the three selected data segments. There are 15 time-series analysed, 3 perpendicular components (x,y,z) at 5 measurement points.

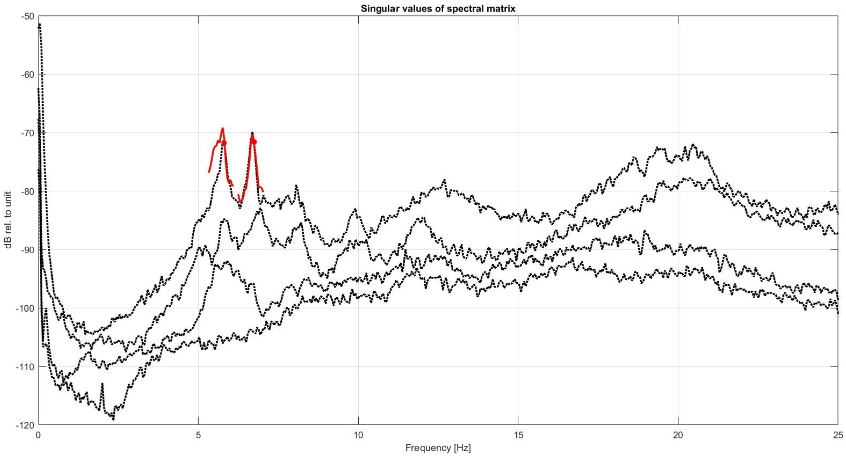

(a) 10 min. series in August 2019.

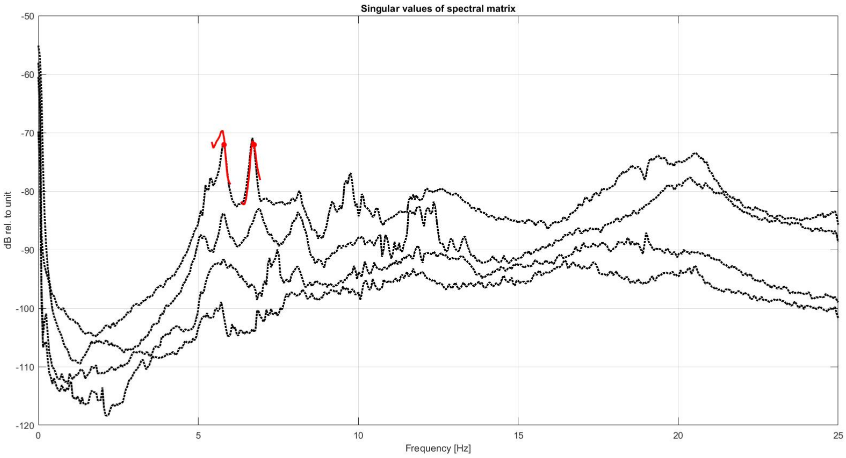

(b) 1 hr. series in August 2019.

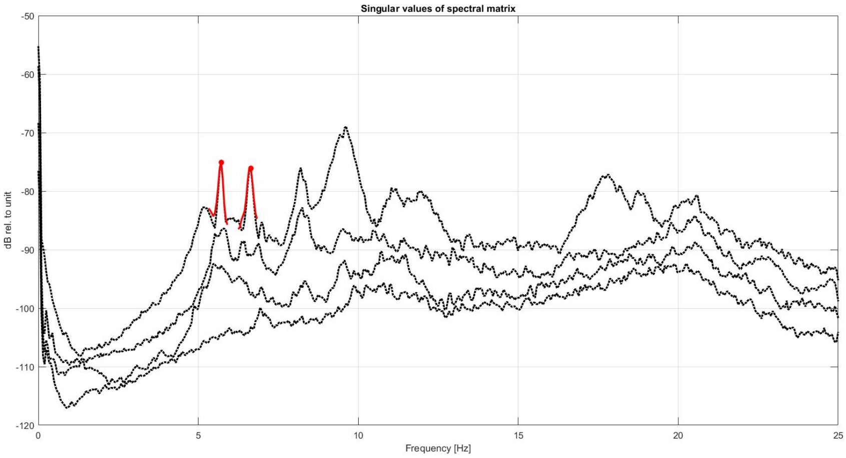

(c) 30 min. series in July 2019

Figure 3.10: Results from using FDD to identify the first two modes on each of the three data sets tested. The singular values of the SD matrix ([dB rel. to m^2/s^3] as function of frequency [Hz]) are shown as black dotted lines. The modal decomposition corresponding to the mode shape vectors is shown by the red solid lines.

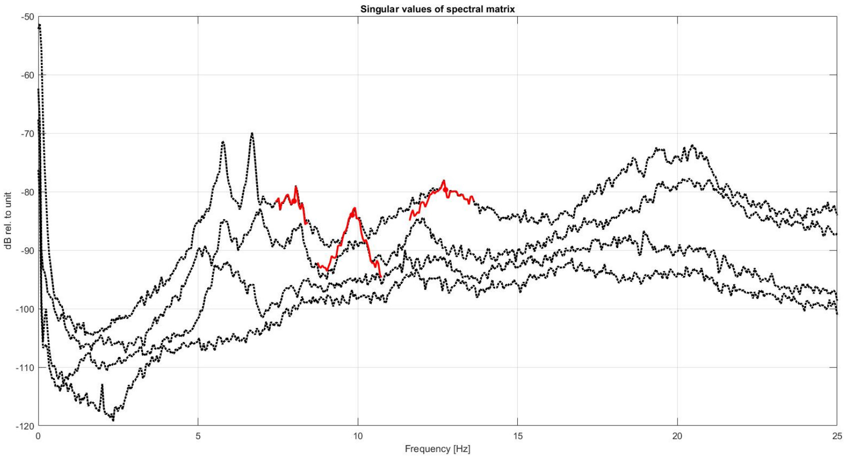

(a) 10 min. series in August 2019.

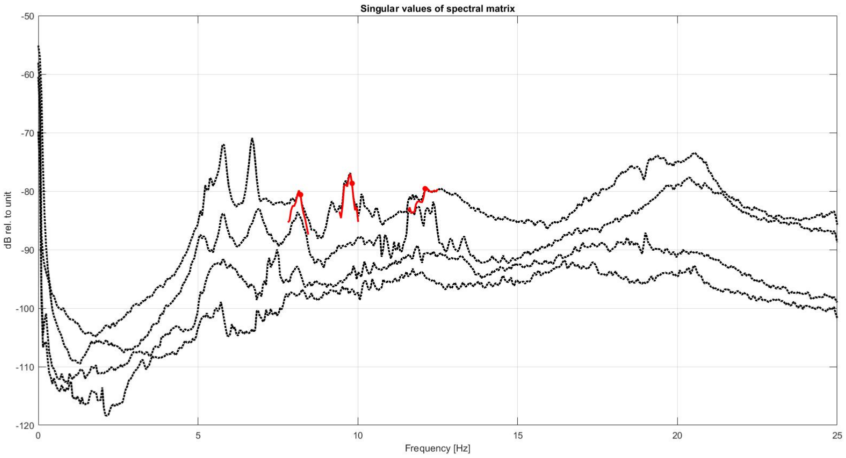

(b) 1 hr. series in August 2019.

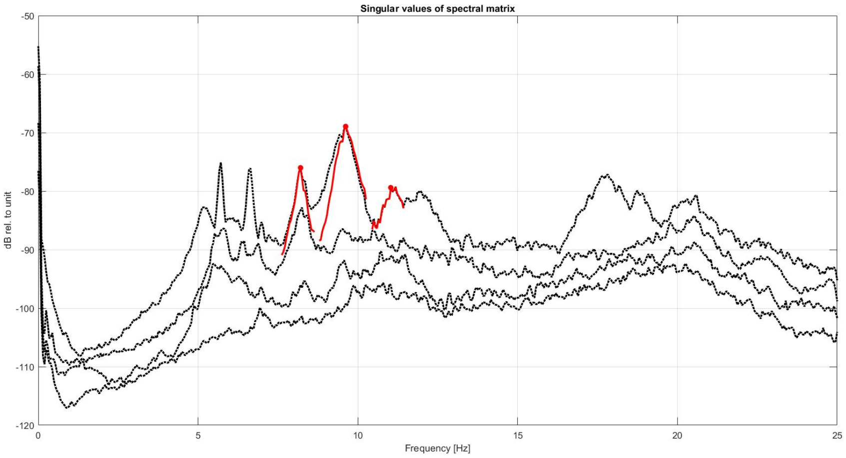

(c) 30 min. series in July 2019

Figure 3.11: Results from using FDD to identify modes 3, 4 and 5 on each of the three data sets tested. The singular values of the SD matrix ([dB rel. to m^2/s^3] as function of frequency [Hz]) are shown as black dotted lines. The modal decomposition corresponding to the mode shape vectors is shown by the red solid lines.

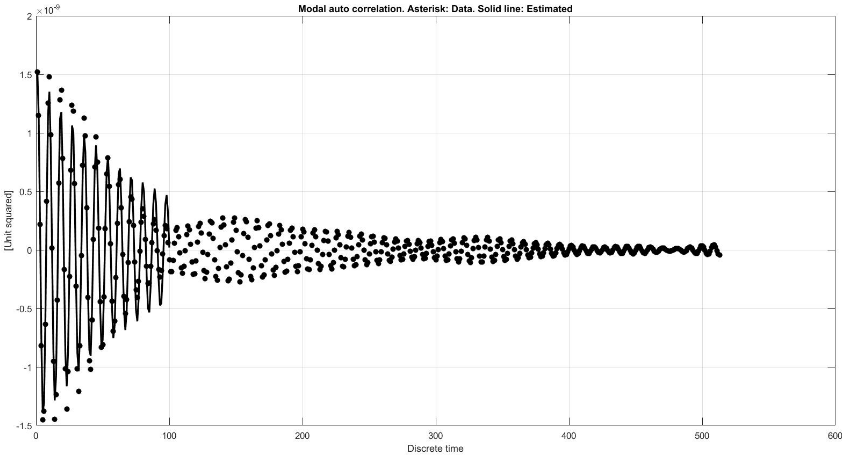

(a) 10-min data from August 2019.

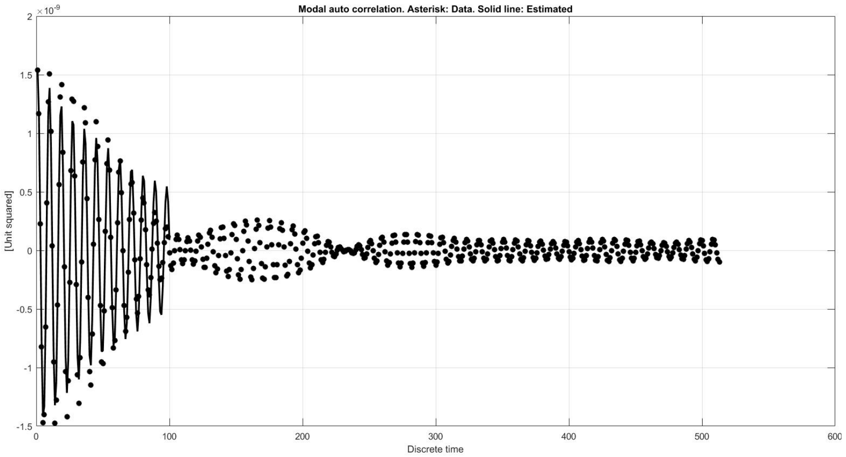

(b) 1-hr data from August 2019.

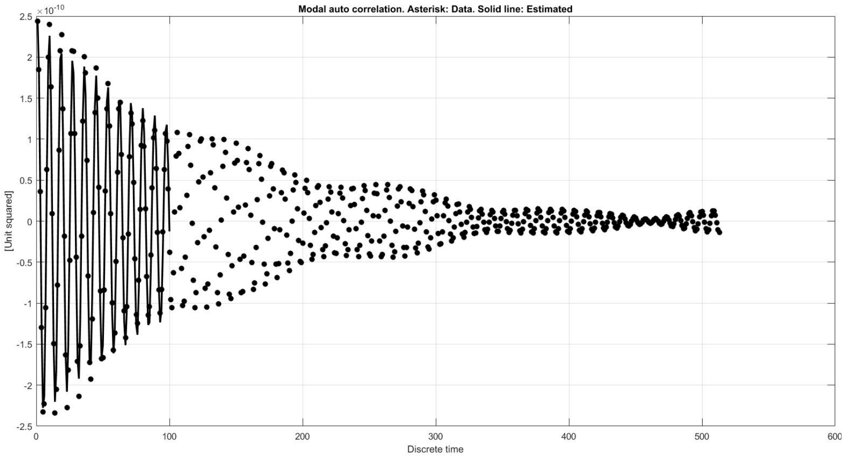

(c) 30-min data from July 2019.

Figure 3.12: The modal autocorrelation function $[(m/s^2)^2]$ for mode 1 (dotted line) as a function of time. The ITD fit on the SDOF system shown by solid line.

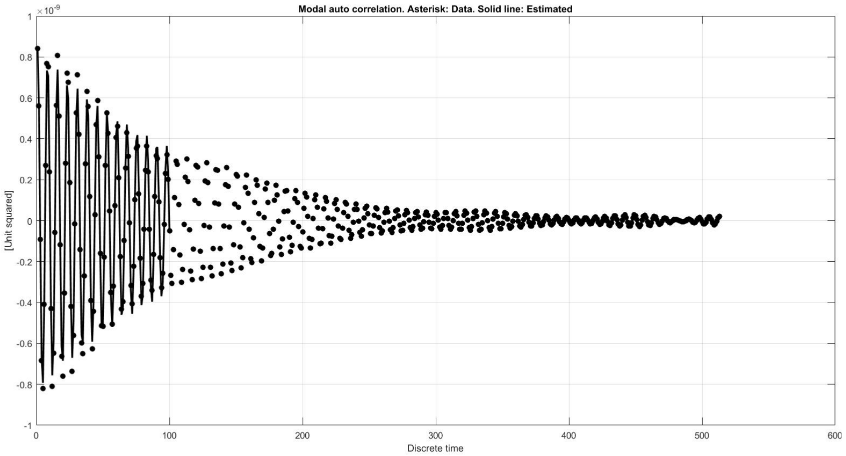

(a) 10-min data from August 2019.

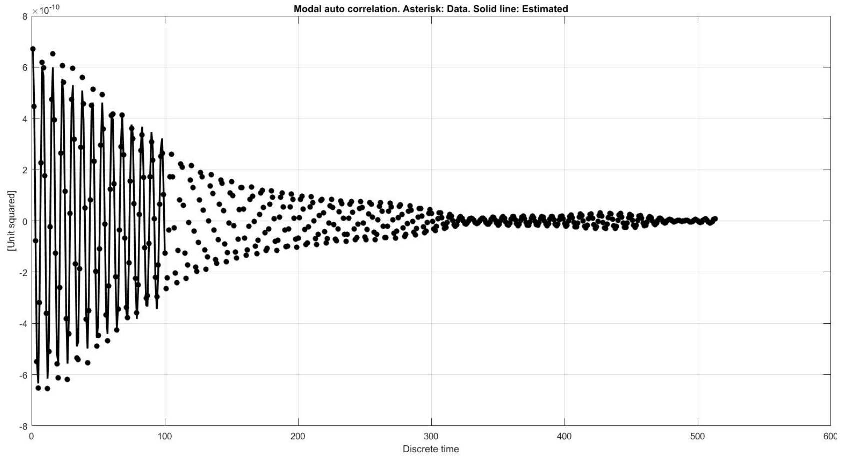

(b) 1-hr data from August 2019.

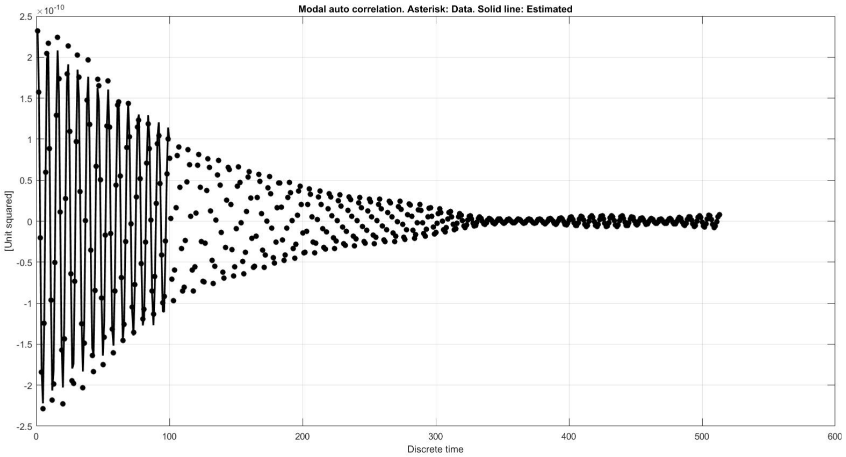

(c) 30-min data from July 2019.

Figure 3.13: The modal autocorrelation function $[(m/s^2)^2]$ for mode 2 (dotted line) as a function of time. The ITD fit on the SDOF system shown by solid line.

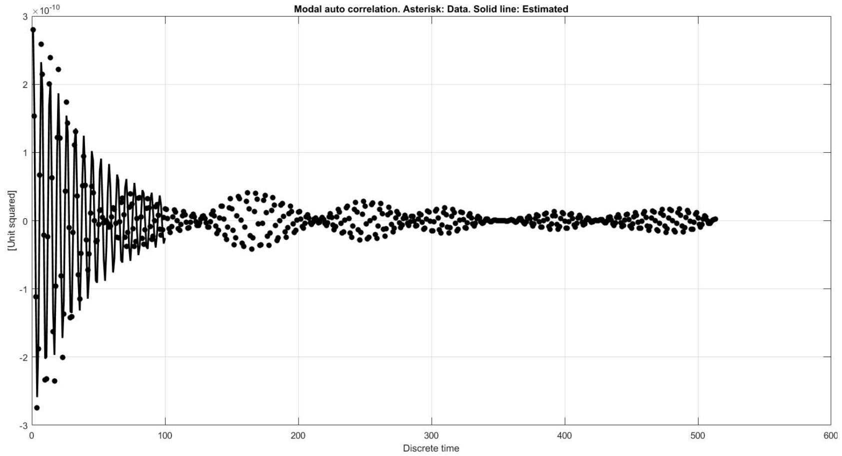

(a) 10-min data from August 2019.

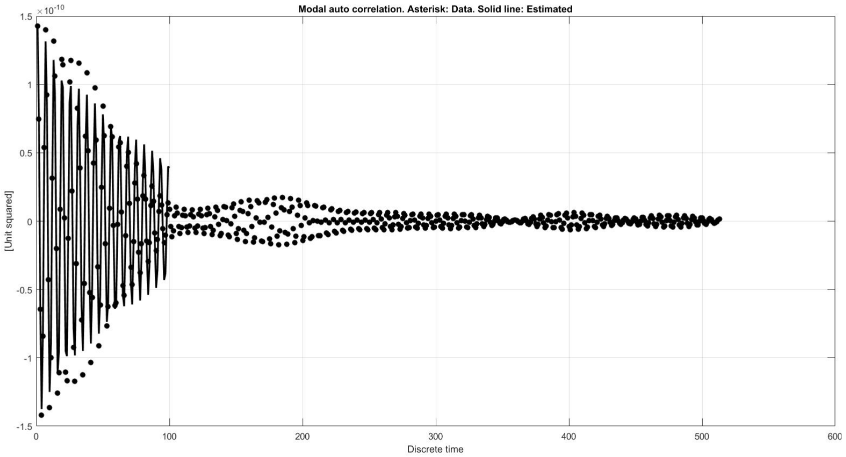

(b) 1-hr data from August 2019.

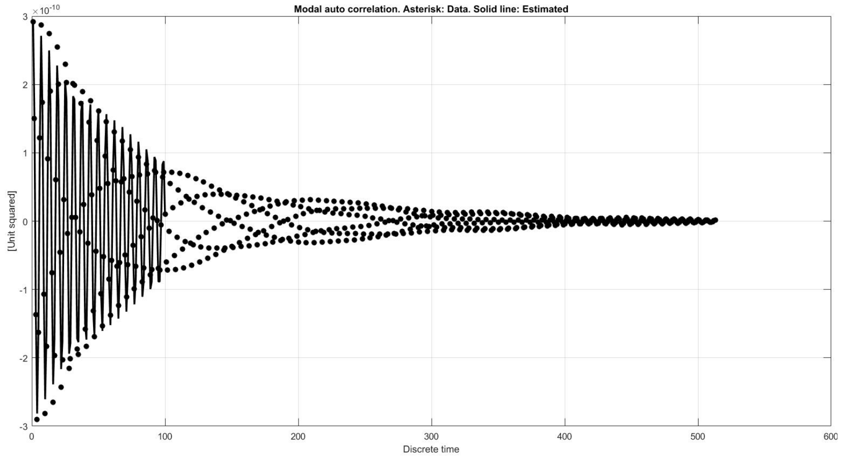

(c) 30-min data from July 2019.

Figure 3.14: The modal autocorrelation function $[(m/s^2)^2]$ for mode 3 (dotted line) as a function of time. The ITD fit on the SDOF system shown by solid line.

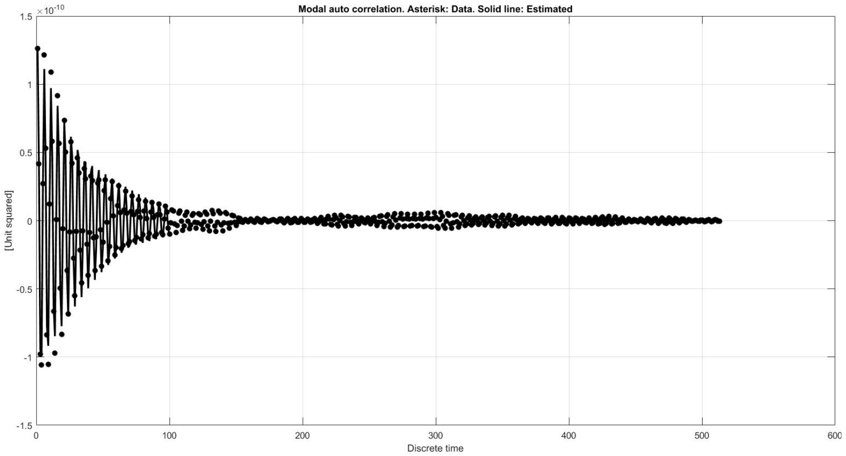

(a) 10-min data from August 2019.

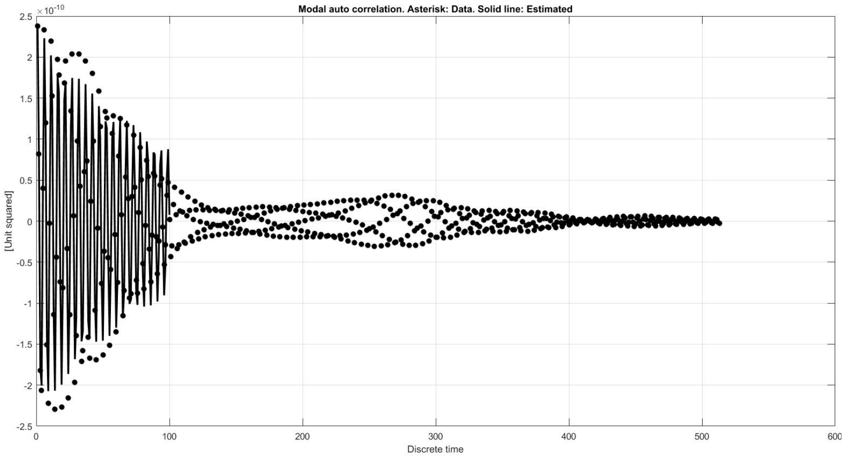

(b) 1-hr data from August 2019.

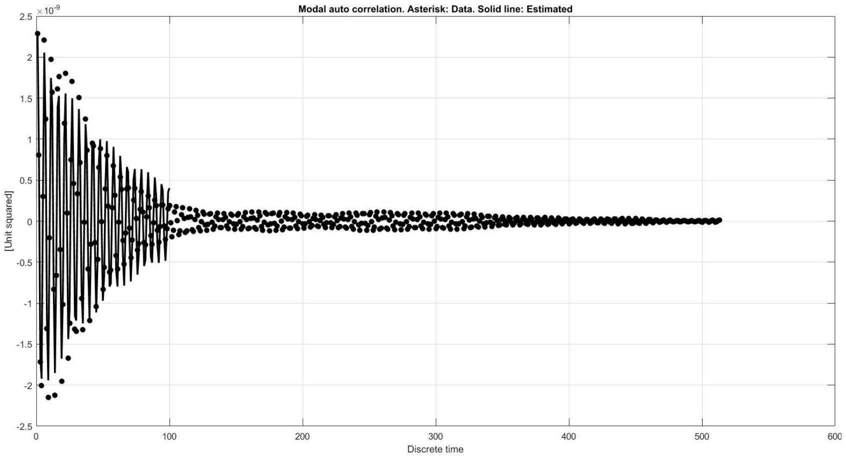

(c) 30-min data from July 2019.

Figure 3.15: The modal autocorrelation function $[(m/s^2)^2]$ for mode 4 (dotted line) as a function of time. The ITD fit on the SDOF system shown by solid line.

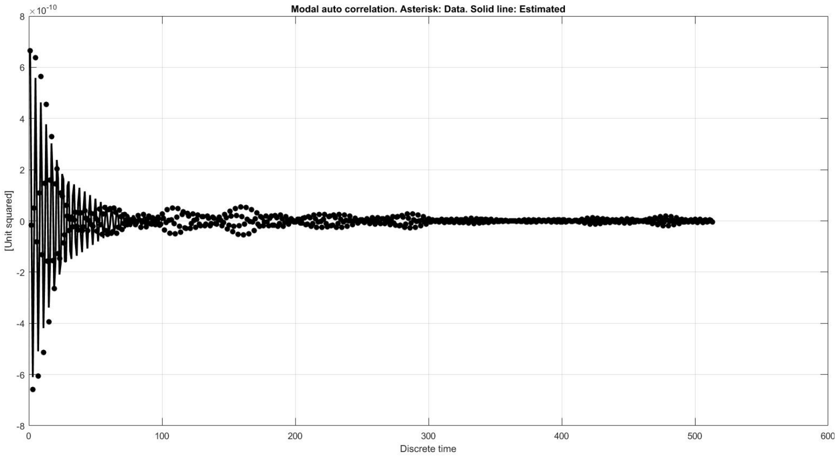

(a) 10-min data from August 2019.

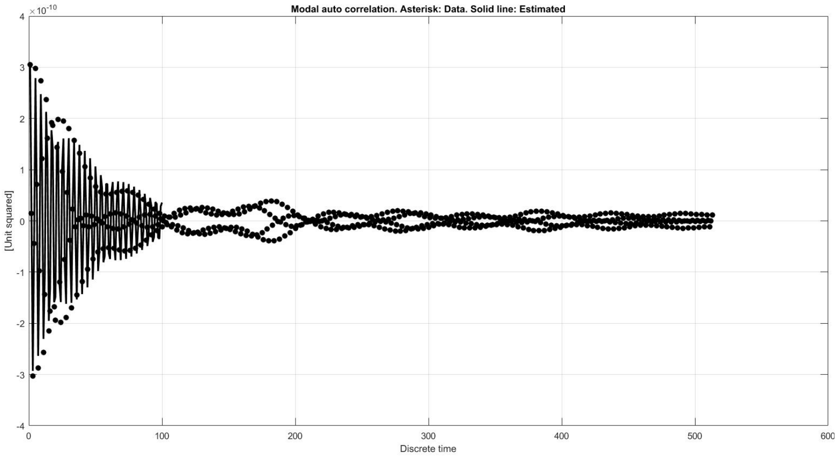

(b) 1-hr data from August 2019.

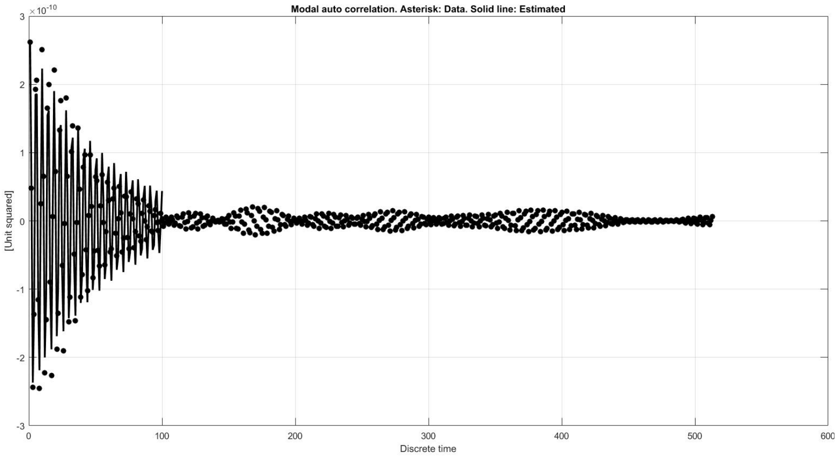

(c) 30-min data from July 2019.

Figure 3.16: The modal autocorrelation function $[(m/s^2)^2]$ for mode 5 (dotted line) as a function of time. The ITD fit on the SDOF system shown by solid line.

The results from the analysis discussed above are compiled in Tables 3.4, 3.5 and 3.6, where they are compared to analysis done on the same data using the ARTeMIS software, applying both the FDD and EFFD methods. More modes are identified through the ARTeMIS software, as the analysis are more automatic, and it is easy to pick out the spectral peaks in the singular value plot. For the modes selected for the MATLAB based FDD analysis, it is difficult to see any systematic difference between the two tools applied. However, there certainly is a variability in the identified parameters, both between the tools used and the datasets analysed. The variability is especially noticeable for the critical damping ratio, as could be expected since damping is generally a tricky parameter that is difficult to establish in exact terms. The variability is seen to be greater for the higher modes, than the lower modes, which is also to expected as they are not as prominent in the frequency spectrum or the SD matrix.

Table 3.4: Results from OMA analysis of a 10 min. segment of ambient acceleration data from August 2019.

ARTeMIS			Matlab based analysis [RB]		
FDD	EFDD		FDD		
Frequency [Hz]	Frequency [Hz]	Damping [%]	Frequency [Hz]	Damping [%]	Modal participation [%]
5.762	5.786	0.907	5.6791	1.70	72.9443
6.673	6.695	1.156	6.7018	1.02	27.0557
8.073	8.07	0.879	7.8881	2.15	94.4952
9.896	9.877	1.257	9.8588	1.98	0.0460
11.979	11.968	0.146			
12.695	12.684	2.356	12.2626	2.69	5.4588
15.234	15.225	0.218			
18.62	18.598	0.707			
19.564	19.496	0.998			
20.54	20.509	0.931			

Table 3.5: Results from OMA analysis of a 1-hour segment of ambient acceleration data from August 2019.

ARTeMIS			Matlab based analysis [RB]		
FDD	EFDD		FDD		
Frequency [Hz]	Frequency [Hz]	Damping [%]	Frequency [Hz]	Damping [%]	Modal participation [%]
5.794	5.785	0.966	5.6691	1.50	60.3854
6.706	6.695	1.168	6.7236	0.85	39.6146
8.171	8.153	0.678	8.1233	1.14	72.6606
9.18	9.196	1.023			
9.733	9.714	1.114	9.7157	0.80	0.3452
10.124	10.116	0.341			
11.589	11.589	0			
12.37	12.32	0.806	12.1736	1.27	26.9942
13.314	13.313	0.34			

Table 3.6: Results from OMA analysis of a 30 min. segment of ambient acceleration data from July 2019.

ARTeMIS			Matlab based analysis [RB]		
FDD	EFDD		FDD		
Frequency [Hz]	Frequency [Hz]	Damping [%]	Frequency [Hz]	Damping [%]	Modal participation [%]
5.697	5.71	0.931	5.6906	1.01	55.9774
6.641	6.623	1.047	6.6130	0.84	55.9774
8.203	8.193	0.834	8.2007	1.08	70.6293
9.603	9.576	1.808	9.6375	1.34	28.5961
11.165	11.147	1.538	11.0900	1.27	0.7746
11.979	11.906	1.817			
13.477	13.457	0.538			
17.676	17.788	2.227			
18.75	18.848	0			
20.573	20.535	0.47			

3.5 Study of the influence of different sensors and different components of motion

As mentioned in the previous section, the modal decomposition and identification of the first mode ($f_1 = 5.7$ Hz) was found to be somewhat ambiguous in the August data. The cause for this is unclear but might be related to some slight difference or shift in the spectral frequency of the lowest mode between different components of motion (x, y z), as mentioned in section 3.3. Or it could also be related to a lower quality of data from the two sensors located on the pillars in August, than the three sensors on the deck in July.

In this section, an attempt will be made to investigate this further. This is done by studying three cases for an OMA of a 1-hour segment of data from August 2019, using both ARTeMIS and MATLAB based analysis. The three cases studied are:

(i) Using only data from the three sensors on the deck, excluding the two on the pillars,
(ii) using only data from the x- and z-components of all five sensors,
(iii) using only data from the z-component of all five sensors.

The results are compared to the results from the FDD-analysis case (b) from the previous section, where all three components of ambient motion, recorded at all five available sensors, comprising 15 data channels, were analysed using a 1-hour data segment. For reference the singular values of the spectral matrix for each case (i, ii and iii) are shown in Figure 3.17. The graphs in Figure 3.17 can be compared with Figure 3.9b, which shows the singular values of the spectral matrix for all the 15 data channels available. It is seen from Figure 3.17, that excluding the sensors on the pillars, does not clarify the spectral matrix. Basically, the spectral peaks have the same form and position, the matrix only includes six less lines.

Excluding the y-component also has limited effect, as the transversal lateral modes have a higher frequency than the modes selected for study in the previous section. However, the second line (from top) of the spectral matrix now shows a very clear peak at the first mode. Perhaps indicating the influence of the x-component on that mode, as is further discussed in the Finite element analysis.

It may be of interest, that if Figure 3.17 (i & ii) are compared to Figure 3.9b, spectral peaks around 18 Hz that are noticeable in the second and fifth line from bottom of the spectral matrix in Figure 3.9b are now missing in Figure 3.17 (i & ii), indicating that a transversal-mode of vibration might have this frequency.

Excluding both the x- and y-component from the analysis, creates the clearest picture of the relevant lower modes or peaks in the spectral matrix. However, we now only have five data channels for the analysis which poses its own limits on the identification.

The results of these analysis are shown in Table 3.7, where the identified natural frequencies and critical damping ratios are listed. The results are very similar for all the cases studied.

The main difference is that when excluding the y components of motion (case ii and iii) then the frequency of mode 5, is found to be lower or 11.9 Hz instead of 12.2 Hz for all channels. Similarly when considering only the vertical data channels (case iii), then the frequency of mode 1 is found as 5.79 Hz instead of 5.67 for all channels.

The critical damping ratio is basically the same for all three cases except for mode 1 in case iii. Then because the frequency peak in the spectral matrix is very clear, the estimated damping ratio is considerably lower than for the other cases or 0.9% instead of 1.5%. This suggests that in previous MATLAB based FDD-analysis the damping ratio for the first mode has been overestimated.

Table 3.7: Results from OMA analysis of a 1-hour segment of ambient acceleration data from August 2019, considering different sensors and different components of motion.

All 15 channels.		Case (i): 3 sensors / 9 channels		Case (ii): x- & z-channels		Case (iii): z-channels only	
Frequency [Hz]	Damping [%]	Frequency [Hz]	Damping [%]	Frequency [Hz]	Damping [%]	Frequency [Hz]	Damping [%]
5.6691	1.50	5.6801	1.47	5.6704	1.48	5.7861	0.90
6.7236	0.85	6.7231	0.82	6.7211	0.82	6.7226	0.73
8.1233	1.14	8.1189	1.13	8.1236	1.11	8.1074	1.12
9.7157	0.80	9.7155	0.82	9.7177	0.80	9.7206	0.79
12.1736	1.27	12.1440	1.31	11.9940	1.31	11.9323	1.28

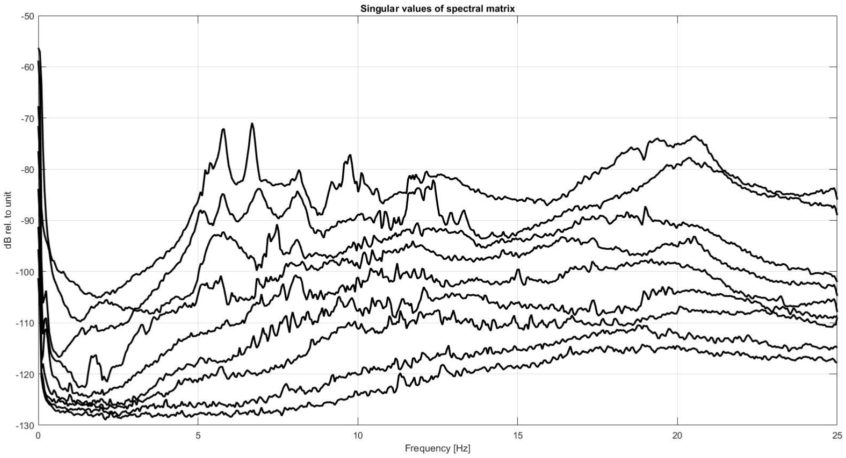

(i) Data from 3 deck sensors (9 channels).

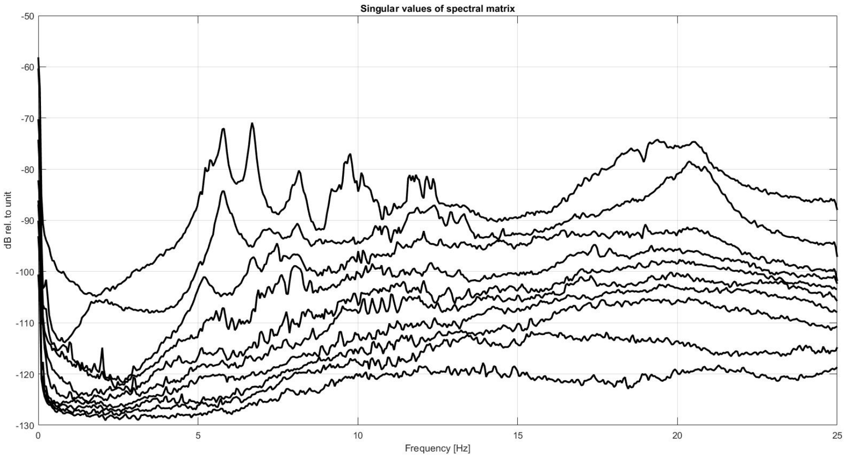

(ii) x- and z-components of all five sensors (10 channels).

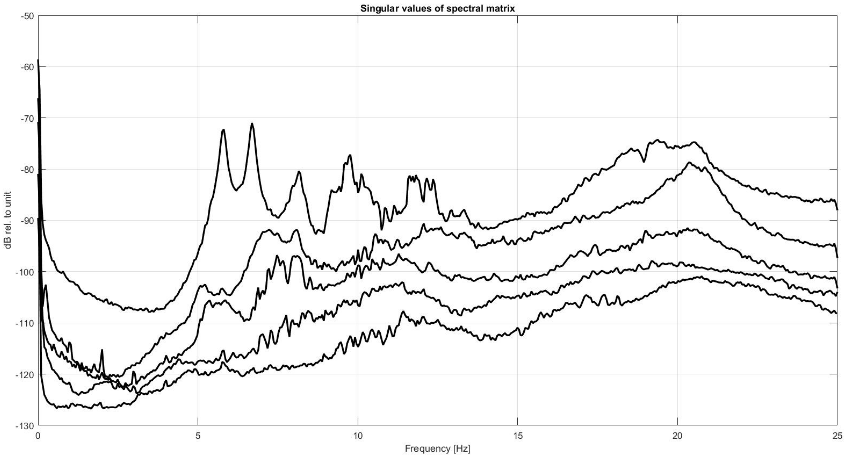

(iii) z-components of all five sensors (5 channels).

Figure 3.17: The singular values of the spectral matrix ([dB rel. to m^2/s^3] as function of frequency [Hz]) for the three cases studied using 1-hour data segment from August 2019.

4 Finite Element Modelling

This chapter describes the finite element modelling of the bridge. The modelling is based on linear analysis, since the objective is to investigate the basic dynamic properties of the bridge, in terms of mode shapes and natural frequencies to be compared with results from system identification of ambient data. The software used for the modelling is SAP2000 from Computers and Structures, Inc. [28].

4.1 The Finite Element Method

The finite element method was introduced to the field of civil engineering around 1960 by Ray Clough [29]. The finite element method is a numerical method for solving problems of engineering requiring the solution of ordinary or partial differential equations. Analytical solutions are usually unobtainable for complicated geometries, loadings, and material properties. Hence, we need to rely on numerical methods, such as the finite element method, for acceptable solutions.

A body is modelled by dividing it into an equivalent system of smaller bodies or units (finite elements) interconnected at points common to two or more elements (nodal points or nodes) and/or boundary lines and/or surfaces. This process is called discretization. Instead of solving the problem for the entire body in one operation, equations are formulated for each finite element and then combined to obtain the solution of the whole body. The finite element formulation results in a system of simultaneous algebraic equations for solution, which yields approximate values of the unknowns at discrete numbers of points in the continuum.

For structural problems, the solution typically refers to determining the displacements at each node and the stresses within each element of the structure that is subjected to applied loads. The displacement is the field variable, and the displacement field is approximated through polynomial shape functions, that depend on the type of element, number of nodes and the associated degrees of freedom. The shape functions interpolate the displacements across the element and are the bases for the development of the stiffness matrix, K, in addition to the material and geometrical properties (see [30]).

In static problems the nodal displacements and rotations, u, are evaluated based on the equation of equilibrium ($Ku = F$) for the loading vector F. Then reaction forces and strains/stresses at the nodes and within the elements can be evaluated, based on the calculated nodal and differential displacements across the element.

In dynamic problems, displacements, velocity, and acceleration are determined based on the equation of motion (see section 3.1). Generally, if the modal approach is used for the analysis, the starting phase is an eigen frequency analysis to establish the mode shapes and natural frequencies [22].

For structural analysis, the following element types are commonly applied: Bar/ Truss, Beam/ Frame, 2D-Plane/ Membrane, Plate, Shell and Solid. The most general elements are the beam element and the shell element, which both have six degrees of freedom at each node, three perpendicular translations and three rotations about perpendicular axis (see Figure 4.1). SAP2000 also offers some special elements, such as Spring, Gap and Hinge, which is used for non-linear analysis. For the beam element, SAP2000 also offers an option to release some of the rotational degrees of freedom within the structure, to create a moment free connection between elements.

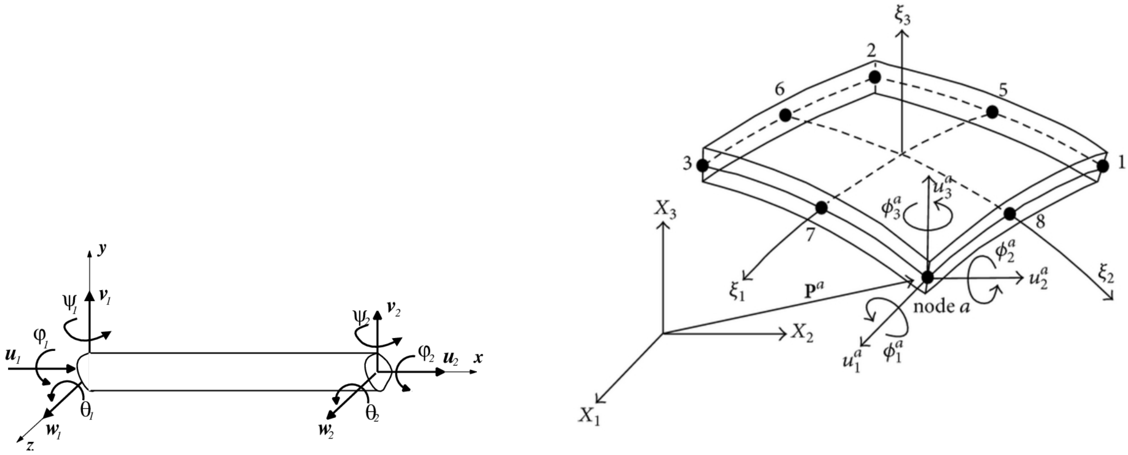

(a) A 3D two-node beam element.

(b) An eight-node shell element.

Figure 4.1: A schematic of a beam- and a shell-element, both have 6 degrees of freedom at each node

4.2 FE Modelling of the Bridge

Two distinctly different FE-models were made of the old Bridge over Steinavötn. On one hand the bridge was modelled as a 2D structure using 3D Beam (Frame) elements only and on the other hand, the bridge was modelled as a 3D structure using shell elements. Several variants of each model were made to investigate the dynamics of the bridge and fine tune the modelling with respect to the natural frequencies found through the acceleration data (see section 2.4). The analysis undertaken were primarily modal analysis to establish the natural frequencies and mode shapes of the structure. However, some static analyses were also done for the static load cases introduced in section 2.2, where various vehicles were driven onto the bridge and the bridge span was loaded with concrete blocks.

The next subsections will describe the different FE-models and the results from the various modelling tests made, are presented and discussed. The basic assumptions made for each model type are explained, including the key structural components involved and the boundary conditions applied. The geometric and structural modelling is based on the original design drawings, that can be found in Appendix A.

4.2.1 The foundation of the bridge pillars

The bridge pillars are founded on piles that are driven 5 m into a thick sandy gravel layer ([31], Appendix A). The soft sand/gravel layer has been estimated to be about 14 m thick, sustained by a stiffer layer below that point.

Direct measurements of the material properties of the actual soil layers are not available. However, similar locations have been investigated using the Spectral Analysis of Surface Wave (SASW) method to estimate the shear wave velocity, as discussed in section 2.4.4. Having obtained an approximate value for the shear wave velocity, Vs, the maximum shear modulus, Gmax, and the maximum modulus of elasticity, Emax, can be estimated through the following relationships:

$$G_{max} = \rho V_S^2 \tag{4.1}$$

and

$$E_{max} = G_{max} \cdot 2(1 + v) \tag{4.2}$$

Where the mass density, ρ, of the gravel is estimated to be 2000 kg/m^3 and its Poisson's ratio, ν, is taken as 0.35 [16]. The shear wave velocity was estimated to be around 160 m/s (see Chapter 2.4.4), which gives a shear modulus of 51 MPa and an elasticity modulus of 138 MPa. These parameters, along with the estimated material and geometrical properties of the timber piles, can then be used to evaluate equivalent stiffness levels for spring elements using pile-soil models like the ones presented by Gazetas [17] and Dobry and Gazetas [32].

Attempts were made to implement 3 DOF and/or 6 DOF "soft" spring elements, representing the pile-soil support, into the FE-models of the bridge. However, those tests were unsuccessful, in the sense that either the spring supports were ineffective compared to pinned supports, or the model behavior became unpredictable. For the Beam-element model the behavior was found to be more or less unaffected by the spring supports for the stiffness levels tested and therefore it was considered unnecessary to complicate the model with their presence. For the Shell-element model, which is more 3-dimensional, the objective was to use the spring stiffnesses to tune the internal difference between the modal frequencies of the model to fit the frequencies evaluated based on the measured data. However, the spring-model behavior was found to be unstable in the sense that at certain stiffness level, small changes in the stiffness of the foundation springs could change the model behavior to such an extent that consistent tuning of many frequencies through varying the foundation stiffness was unachievable.

In the end it was decided to use a simpler approach, both for the pillars and the end-supports, that is further documented in the upcoming sections. Regarding this decision, it should be noted that the excitation of the bridge during the observation period was of relatively low intensity and therefore direct soil-structure interaction should be minimal, perhaps excluding the pile-driving phase, but studies of that excitation phase are out of the scope of this study.

4.2.2 The boundary conditions of the deck at the end pillars

The deck rests on the end pillars as shown in Figure 4.2. As can be seen the support looks like a basic roller. The roller bearings are further described through Figures 4.3 and 4.4.

Based on the figures shown, the first assumption was to model the end supports as rollers on one side of the bridge and pinned on the other side, to insure stability. However, during the various modelling trials, it was discovered that the effective end conditions are slightly more complicated. This will be further discussed in sections 4.3 and 4.4. It should be noted that the end pillars are not included in the modelling, only the end boundary of the deck, which is controlled by the reaction of the bearings.

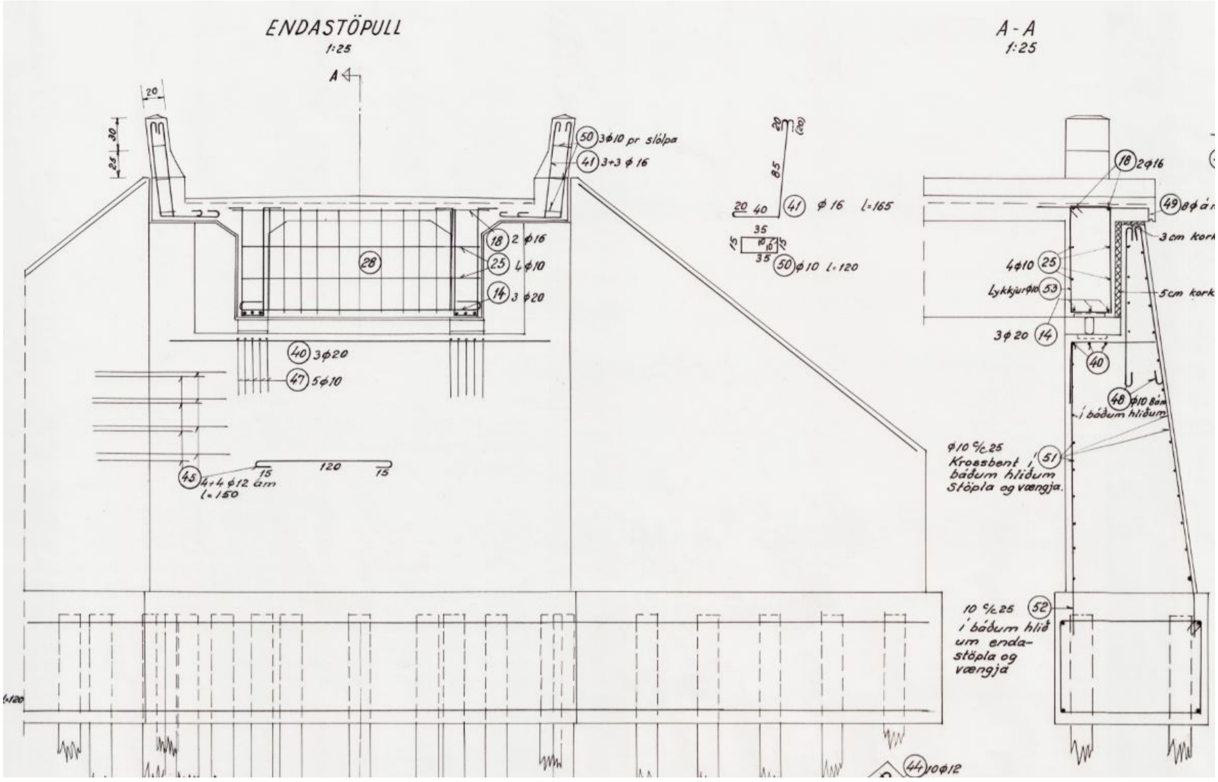

Figure 4.2: A cut out from a design drawing showing the end pillar and the support conditions (Appendix A.2).

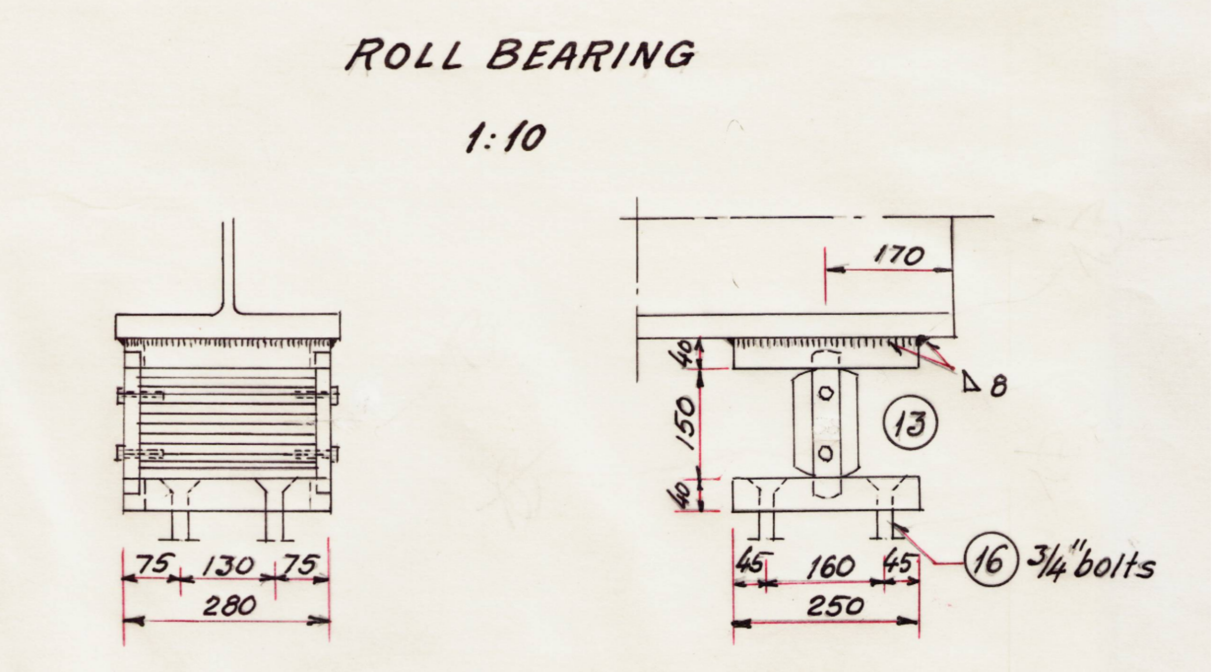

Figure 4.3: A drawing of a similar roll bearing from another bridge from the same era (provided by IRCA).

Figure 4.4: Photos of the end support rollers (photo Einar Óskarsson, IRCA).

4.2.3 The connection between the deck and intermediate pillars

The pillars supporting the bridge deck are semi-rigidly connected to the bridge via an internal reinforcement column going from the bottom of the pillars up into the web of the girder section, as shown in Figure 4.5, which is a cut out of the original design drawings (see Appendix A.1). Even though the pillars and deck are concreted separately, moments and shear forces are transferred between pillar and deck, to the extent of the capacity of the column. The dimension and stiffness of the deck section is however much greater than the internal column connecting to the pillar, therefore the connection can perhaps not be considered fully rigid. This was tested to some extend in the modelling phase. Furthermore, it has been suggested that the deck-pillar connection at the three pillars linked to the subsidence of pillar no. 3 from west, may have been damaged and now form a hinge, as mentioned in Chapter 1.1. This was also tested to some extend in the modelling phase.

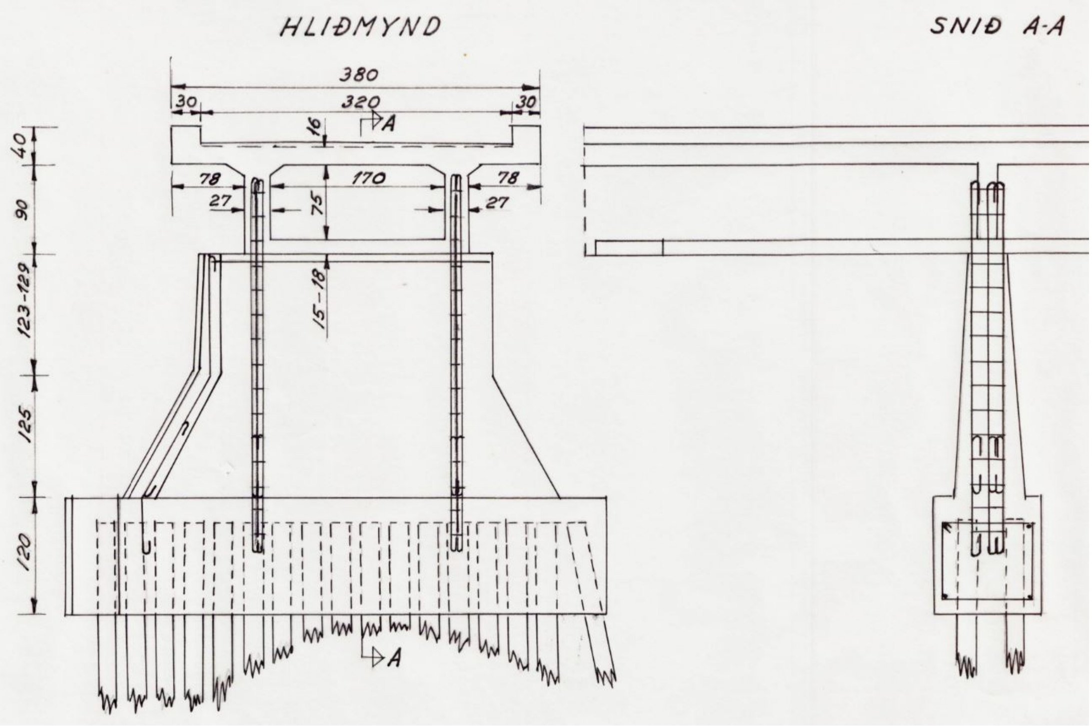

Figure 4.5: A view of the pillar deck connection.

4.2.4 Material properties of the bridge

Finite element modelling requires material properties for the elements used. For the case at hand the required properties are basically the density of reinforced concrete, the modulus of elasticity (E) and the Poisson ratio (ν). The material properties used were the traditional density of reinforced concrete, 2500 kg/m^3 and the Elasticity modulus was taken as 34 GPa. The elasticity modulus is based on two direct tests done on the bridge material.

After the shear- failure test mentioned in Chapter 2.1 had been performed, cylindrical cores were drilled out from the deck, and the compressive strength of the concrete tested [10]. The average compressive strength of the concrete samples from the deck was found to be around 37 MPa, which is indicative of concrete class C30/37 [11].

At the end of the initial testing in July, ultra-sonic measurements were undertaken on the concrete pillars and the side beams of the deck to establish the dynamic modulus of elasticity. The results are presented in Appendix C. The average value of the modulus was found to be 39 GPa, which can be considered to indicate the same concrete class of C30/37, taking into account that the dynamic modulus can be about 20% larger than the static one. According to the measurements presented in Appendix C, the pillars have a slightly higher E-modulus than the deck sections.

The key geometric and material properties used for the Beam-element bridge model are shown in Table 4.1. For the sake of simplicity, it was decided after some trials to use standard concrete properties of C34/45 (E=34 GPa) for the bridge in its entirety. This is somewhat higher grade than the compressive strength indicated, but since the study is primarily dynamic and the ultra-sonic measurements gave relatively high values for the modulus of elasticity, this is considered reasonable. The variation in the elasticity modulus between concrete grades is also not very large [11].

Table 4.1: Key geometric and material properties used for the Beam model of Steinavötn bridge (x, y and z are the global deck coordinates).

Bridge element	Concrete Properties (EN1992-1-1)	Material properties			Geometric properties			
		Elasticity modulus (GPa)	Density (kg/m^3)	Poisson ratio	Area (m^2)	Ix (m^4)	Iy (m^4)	Iz (m^4)
Closed deck sections	C35/45	34	2500	0.2	1.619	0.498	0.261	1.808
Open deck sections	C35/45	34	2500	0.2	1.364	0.028	0.142	0.175
Pillars (on average)	C35/45	34	2500	0.2	2.22	2.533	0.067	0.239

4.3 Beam-Element Model

The beam element requires the properties of the cross-sectional geometry to be modelled, in terms of the area (A) and the moment of inertia about all axes (Ix, Iy, Iz). The bridge cross-section was modelled using the section designer in SAP2000. Figure 4.6 shows the geometry of the closed and open part of the cross-section of the bridge deck. The section designer calculates the relevant geometrical properties (see Table 4.1), which can then be applied to the appropriate sections along the span of the bridge model.

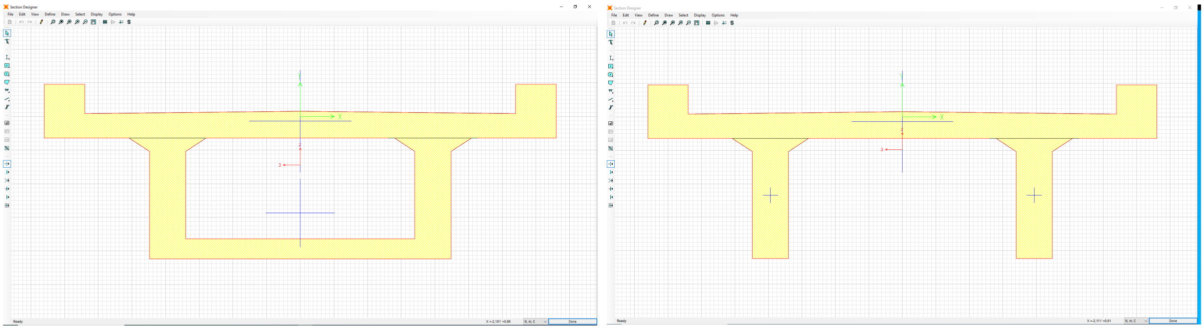

Figure 4.6: The geometry of the closed and open part of the cross-section of the bridge deck.

It should be noted that the thickness of the deck was taken as the structural design thickness of the girder (16 cm), plus 3 cm on average of the overlay that was originally concreted at the same time as the girder structure.

The pillars supporting the deck were modelled as five blocks, varying in size, one on top of the other, as shown for the extruded deck and pillar profiles in Figure 4.7. As seen in Figure 4.7, the deck sections around the pillars are closed box sections, whereas the middle deck sections are double T (TT) sections. The pillars are modelled all the way down into the sand towards the pile/sand level (see Figure 4.5). A “frame insertion point” is defined for the deck sections with a “cardinal point” at the bottom of the deck beams to introduce an offset for the deck beam, to account for the fact that the pillars connect to the deck at the bottom of the deck but not at the centroid of the deck sections [28].

The Beam element model consists of total 193 beam elements and has 1125 degrees of freedom. The average length of each element is about 67 cm.

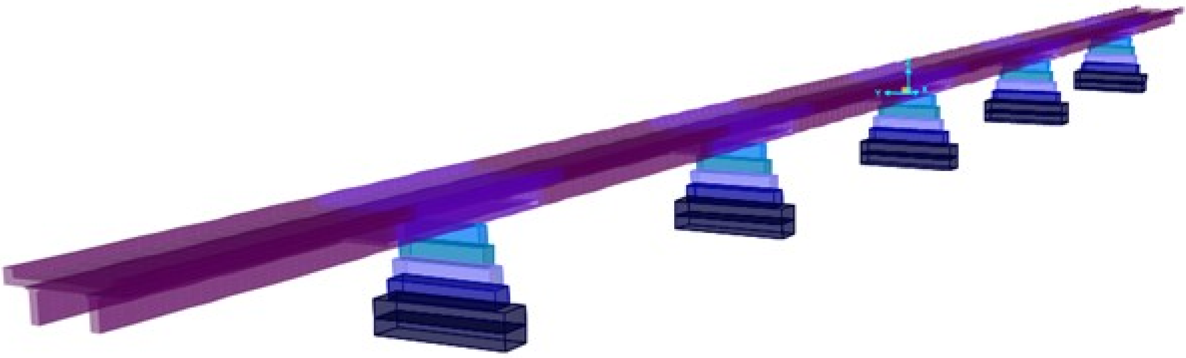

Figure 4.7: An extruded view of the deck sections and the pillar sections of the Beam-element model.

After the initial beam element-model was established, various boundary conditions were applied to the model to investigate how best to replicate the natural frequencies observed in the measured data. An overview of the various boundary conditions tested for the FE-model is given in Table 4.2. The natural frequencies evaluated for the different boundary conditions tested are then displayed in Table 4.3. The axis system of the model and notion used in Table 4.2 are as follows: The x-axis is longitudinal, the y-axis is transverse, the z-axis is vertical, u indicates displacement and r stands for rotation.

Going through Table 4.2, the initial choice of BC's was to pin both end-supports as well as the pillar supports (model A). However, in the Beam-element model it is necessary to fix the rotations at the pillar foundation about the x-axis, since the connection is only a single point and due to the width of the column, the rotation about the x-axis (rx) should be minimal, as should the vertical rotation (rz) at that point. So effectively the pillars are fixed except the rotation about the y-axis (ry). As seen in Table 4.3 this gave excessively high natural frequencies as expected.

The next option (model B) was to simply release the x-translation at the eastern end-support. This resulted in natural frequencies of the order expected from the OMA analysis in Chapter 3, except for the first mode, which was still high.

Then it was decided to release the x-translation at both ends (model C), which again gave reasonable results for all modes except the first one, which now had much to low frequency. To counteract this there were two options possible, i.e. to introduce rotational stiffness about the y-axis at the pillars (model D) or introduce an axial stiffness at the end-supports (model E). Both options are reasonable, as the piles underneath the pillars will create an axial force couple when the bridge vibrates and thereby some rotational stiffness about the transverse y-axis. Similarly, there is some resistance in the end support rollers to axial motion, that can be interpreted as axial stiffness.

The initial stiffness estimate for the rotational stiffness was based on the axial stiffness of the piles $(K_{pax} = \frac{E_p A_p}{L})$ using the formulation:

$$K_{ry} = \frac{b^2}{2} K_{pax} \tag{4.3}$$

where b is the distance between the two rows of piles underneath the pillars (b $\approx$ 0.825 m). This assumes small displacements and gives a stiffness of 360 MNm/rad, based on assumed modulus of elasticity for timber and the total area of piles. The actual stiffness required to get an acceptable value for the first natural frequency was however only 85 MNm/rad. The initial axial stiffness at the end supports was based on the same order of magnitude and then tuned to fit the first modal frequency. The resulting axial stiffness at the supports was 190 MN/m.

The next model tested included a settlement of pillar no. 2 from west, i.e. the damaged pillar. This was implemented through the following steps:

- releasing the pillar support,
- running a static load case with the dead weight of the bridge as loading,
- initiating a scaled undeformed geometry modification to get $\sim$ 200mm displacement of

the pillar based on the gravity load case,

- re-fix the pillar support,
- run the modal analysis.

The boundary conditions applied, and the modified geometry achieved by simulating the pillar settlement, is shown in Figure 4.8. The frequency result is shown in table 4.3 for model F. As can be seen the influence of this change in geometry is minimal for the Beam element model. It should be noted, that when the pillar was released, the gravity loading in linear state produced a settlement of 56 mm, or only roughly 1/4 of the observed settlement, the rest must therefore have been induced through non-linear behaviour, resulting in fractures in the tension zone of the deck at neighbouring pillars and consequently permanent deformations.

The two final versions of the Beam model include both axial springs at the end-supports and rotational springs at the pillars. It is believed that this is the most realistic case, as there definitely is some rotational stiffness at pillars and also some resistance in the end-supports. As seen in Table 4.2 and 4.3, some fine tuning of the springs applied was required to get the first natural frequency at 5.7 Hz. The tuning could have been done differently, depending on the importance placed on the two different boundaries. However, excluding the first mode, the details of the BC's are of fairly limited consequence. It is in fact noteworthy how stable the modal frequencies from mode 2 through 12 are for the entire process, although the mode shapes may be affected to some extent.

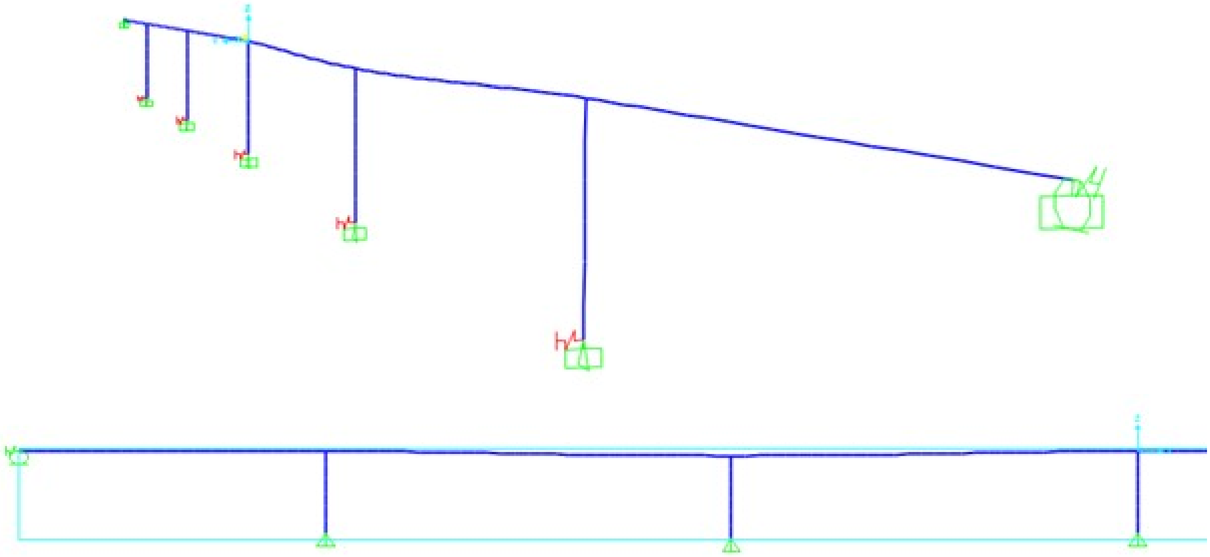

Figure 4.8: The boundary conditions applied, including rotational springs at pillars and axial spring at the end-supports. The settlement at pillar no. 2 from west can also be seen both in the partial 2D xz view (bottom, west end on the left) and the 3D view (top, west end on the right).

Table 4.2: The various boundary conditions (BC's) tested for the Beam element model.

Model id	West end support	East end support	Pillar supports	Settlement of pillar
A	Pinned	Pinned	Fixed – ry (free)	No
B	Pinned	Pinned – ux (free)	Fixed – ry (free)	No
C	Pinned – ux (free)	Pinned – ux (free)	Fixed – ry (free)	No
D	Pinned – ux (free)	Pinned – ux (free)	Fixed – ry (free) + ry-spring (kry=85 MNm/rad)	No
E	Pinned – ux (free) + ux-spring (kx = 190 MN/m)	Pinned – ux (free) + ux-spring (kx = 190 MN/m)	Fixed – ry (free)	No
F	Pinned – ux (free) + ux-spring (kx = 190 MN/m)	Pinned – ux (free) + ux-spring (kx = 190 MN/m)	Fixed – ry (free)	Yes (∼20 cm)
G	Pinned – ux (free) + ux-spring (kx = 190 MN/m)	Pinned – ux (free) + ux-spring (kx = 190 MN/m)	Fixed – ry (free) + ry-spring (kry=85 MNm/rad)	Yes (∼20 cm)
H	Pinned – ux (free) + ux-spring (kx = 170 MN/m)	Pinned – ux (free) + ux-spring (kx = 170 MN/m)	Fixed – ry (free) + ry-spring (kry=70 MNm/rad)	Yes (∼20 cm)

Table 4.3: The natural frequencies from the Beam element models tested.

Model id:	A	B	C	D	E	F	G	H
Mode nr.	f_n [Hz]	f_n [Hz]	f_n [Hz]	f_n [Hz]	f_n [Hz]	f_n [Hz]	f_n [Hz]	f_n [Hz]
1	6.87	6.76	3.44	5.69	5.70	5.70	5.91	5.72
2	8.05	7.06	6.89	7.07	6.90	6.90	6.92	6.91
3	9.01	8.16	7.91	8.06	7.96	7.95	7.97	7.96
4	10.89	9.58	9.43	9.56	9.50	9.50	9.51	9.50
5	11.34	11.33	11.20	11.29	11.26	11.26	11.28	11.27
6	12.35	12.41	12.49	12.49	12.49	12.39	12.39	12.39
7	12.89	13.02	13.04	13.10	13.15	13.08	13.08	13.08
9	13.62	13.11	13.15	13.15	13.32	13.31	13.32	13.29
10	14.17	13.72	13.29	13.30	13.69	13.69	13.69	13.66
11	14.31	14.20	13.80	13.80	13.80	13.75	13.75	13.75
12	15.90	14.55	14.22	14.22	14.22	14.18	14.18	14.18

The modal participation factors from Model-H are given in Table 4.4. The modal participation factors are the dot products of the six Acceleration Loads, associated with the 6 DOF at each node. These factors are the generalized loads acting on the mode due to each of the Acceleration Loads. These values are called "factors" because they are related to the mode shape and to a unit acceleration. Each mode shape is normalized, or scaled, with respect to the mass matrix such that the modal mass is equal to 1, as seen in Table 4.4.

Table 4.4: Natural frequencies & modal participation factors from beam-element Model-H.

Mode No.	Frequency (Hz)	Participaton factors						Modal Mass (N-mm-s2)	Modal Stiffness (N-mm)
		UX (N-mm)	UY (N-mm)	UZ (N-mm)	RX (N-mm)	RY (N-mm)	RZ (N-mm)		
1	5.72	21.34	0.00	0.01	0	-2154	0	1	1292
2	6.91	-1.26	0.00	-0.00	0	10534	0	1	1887
3	7.96	0.10	0.00	-0.88	0	-278	0	1	2503
4	9.50	-0.50	0.00	0.02	0	40840	0	1	3564
5	11.27	-0.01	0.00	-4.50	0	90	0	1	5015
6	12.39	0.00	-0.12	0.00	261	0	54779	1	6060
7	13.08	0.00	2.63	0.00	-1587	0	-2318	1	6749
8	13.29	-0.06	0.00	-0.02	0	-449167	0	1	6971
9	13.66	-0.01	0.00	15.15	0	-357	0	1	7372
10	13.75	0.00	1.01	0.00	222	0	-237149	1	7466
11	14.18	0.00	12.33	0.00	-7984	0	20055	1	7936
12	16.90	0.00	-6.3	0.00	4457	0	275261	1	11270

The modal participation factors give an information on the key directional and rotational components of the modes. As can be seen from Table 4.4 the dominant participation component of the first 4 modes is the rotation about the y-axis (RY), although mode 1 has also a strong axial-translational component (UX). Mode 5 is primarily a vertical translational mode, and then mode 6 and 7 are controlled by transverse displacement (UY) and rotation about the vertical axis (RZ) and the longitudinal axis (RX), indicating a torsional component. Mode 8 is again RY dominated and Mode 9 controlled by vertical displacement. Then modes 10, 11 and 12 are again transverse/torsional modes (UY, RX and RZ). The first ten mode shapes are shown in Appendix F.

Early in the modelling process, some attempts were made to simulate the supposed structural damage of the bridge that occurred in 2017. This was done through moment releases at the pillar that settled and the neighboring spans. This did not really work properly, the mode shapes became discontinuous, and the various modes that were introduced are not noticeable in the recorded low intensity ambient data. It is also recognized that full moment release is an unrealistic condition, even though there may have been some yielding and plastic deformation induced by the settlement of the pillar affected by the scouring.

One might also argue that it would be reasonable to introduce springs for the vertical displacement at the pillar supports, representing the axial stiffness of the piles/soil. This was tested but found to have a minor influence on the modes recorded and was therefore not pursued further, as it is difficult to evaluate the true vertical stiffness, unless there is a mode measured that depends upon it.

4.4 Shell-Element Model

Detailed 3-dimensional shell element models were built of the bridge, forming the sides of the box/double-T deck beam using shell elements representative of the thickness of the top, sides and bottom parts of the beam. The pillars were also modelled by shell elements, which followed the geometry and thickness of the pier columns and their foundation. The advantage of the Shell element model over the Beam element model, is that the Shell model provides a true three-dimensional geometric view of the modes of vibration for the bridge. This allows one, for example, to observe any torsional effects in a much clearer way than is possible for beam-model. The modelling of the deck girders is rather straightforward, as the shell elements basically follow the geometries given by the drawings in Appendix A. However, when modelling the pillar foundations there are some options to choose from. During the modelling phase, three slightly different models of the pillars were built.

Model I, was made without the lowest part of the pillars, that is the foundation element, connected to the piles and half buried in the sand. The idea was that this element was stiff enough to assume that the upper part of the pillar could possibly be assumed as fixed at the bottom.

Model II, included the foundation element as a vertical shell element (1.1 m thick and 1.2 m high), which was then assumed to have limited rotational stiffness about the transverse y-axis.

Model III, included the foundation element as two horizontal elements connected to the upper pillar elements at the center. This allows defining boundary conditions for nodal points lying along two transverse horizontal lines at the bottom of the foundation. If the BC's are defined as pinned, then the rotational stiffness is determined by the stiffness of the elements and the width and length of the foundation elements. However, the pillar configuration in Model III, was judged to be too stiff, as the physical height of the bottom elements was partly lost, and the model did not reflect the proper frequency difference between the modes of vibration when the boundary conditions of the pillars were defined in this way. The modelling of the required rotational flexibility was also more complex.

It was therefore decided to use Model II as the most proper model. The model, shown in Figure 4.9, consists of 4280 shell elements and has 27678 degrees of freedom. The model uses auto-meshing based on relatively few key elements, that limits the largest width of each sub-element to about 50 cm. It should be noted that the effective stiffness depends on the average element size, as a denser mesh results in added flexibility and thereby lower natural frequencies. After a convergence study, the mesh size used was judged to be a reasonable compromise between computational time and accuracy.

As discovered for the Beam element model, it was found that the free vibrations of the model were controlled by a delicate balance between the rotational stiffness of the pillars and the axial stiffness of the "rollers" at the end supports. Various experiments were made with regards to the boundary conditions of the model to get natural frequencies corresponding to the modes of vibration identified from the acceleration data. In the end, the same choice was made as for the Shell element model as for the Beam element model, that is to apply a spring with stiffness in the longitudinal direction (x-dir.) at the end supports, and a rotational spring providing resistance to the rotation about the y-axis.

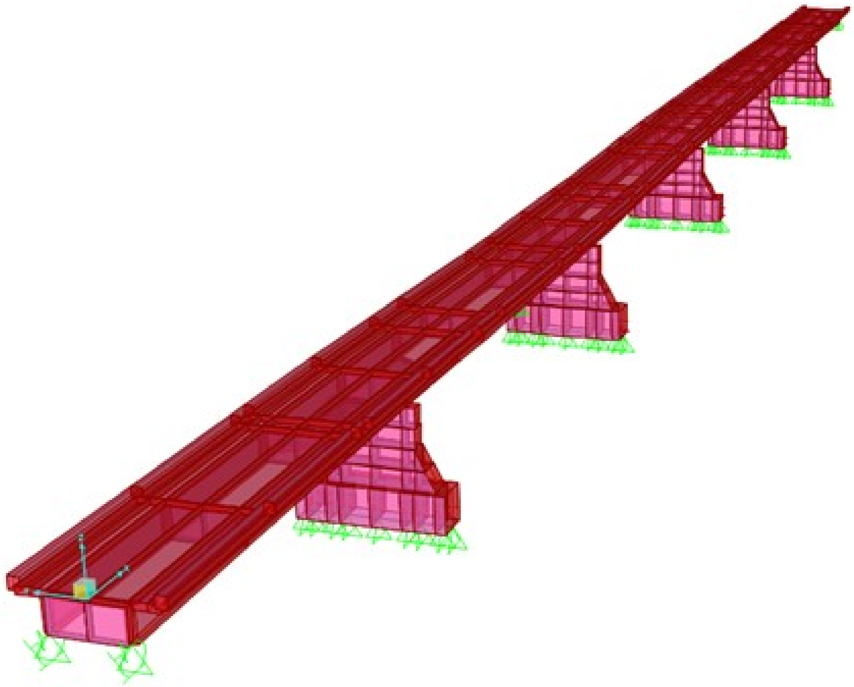

(a) View of model from top.

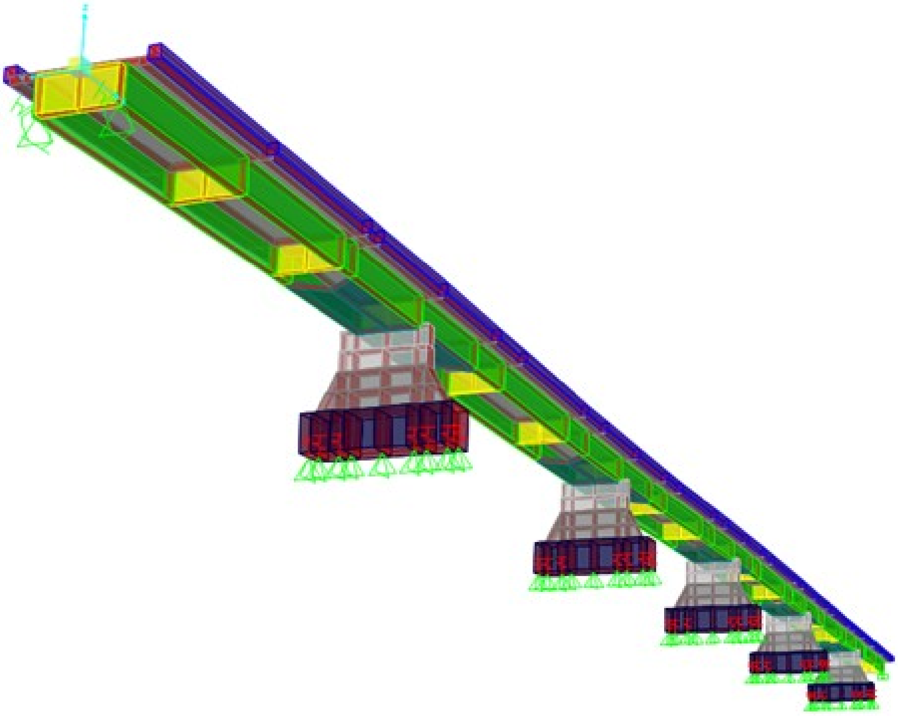

(b) View of the different element sections from below.

Figure 4.9: The Shell element model of the bridge over Steinavötn River.

Table 4.5 lists the boundary conditions applied to the Shell element model. The same material properties were used for the Shell element models as previously for the Beam element model (see Table 4.1). These conditions provided modal analysis that resulted in a good fit with the natural frequencies observed in the acceleration data.

Table 4.5: The boundary conditions (BC's) of the Shell element model (version II).

West end supports	East end supports	Pillar supports	Settlement of pillar
Pinned – ux (free) + ux-spring (kx = 2 x 850 MN/m)	Pinned – ux (free) + 2 ux-spring (kx = 2 x 850 MN/m)	Fixed – ry (free) + ry-springs (kry = 9 x 8 MNm/rad)	Yes (~20 cm)

Table 4.6 shows the natural frequencies evaluated for the final shell-model and the associated participation factors, modal mass, and stiffness. The first 10 mode shapes for the finalized model are shown in Appendix G.1. As seen in Table 4.6, the first modes of vibration are basically controlled by three components of motion, the x-component, z-component, and rotation about the y-axis. Of those three it is the x-component and the rotation that show the largest participation.

Using the basic boundary conditions, with the translations fixed for one end and the x-translation free for the other, could with limited tweaking, give a reasonable value for the first mode, that was comparable with the lowest frequency observed in the ambient data. However, the frequency values of the next modes did generally not fit particularly well with the observed values. That is why the axial resistance at the end supports, and rotational resistance at the pillar supports is required to get an acceptable calibration of the FE models.

The key new information is that the Shell element model demonstrates, that above 14 Hz there are numerous torsional modes of vibration, whereas below 14 Hz there are 7 modes with a dominantly up-down motion, which is largely controlled by the rotation about the transverse y-axis. The torsional modes seen in the Shell-model are not well separated in frequency and are therefore not easily identified in the acceleration data, although a broad peak of energy can be seen in the power spectra below 15 Hz and around 20 Hz. The Shell element model does not show the transverse modes (y-displacement and z-rotation) seen in the results from the Beam element model. But as mentioned, the higher modes (above 14 Hz) are dominated by torsion, which is not unexpected for a double T section girder.

Table 4.6: Natural frequencies & modal participation factors from shell-element Model-II.

Mode No.	Frequency (Hz)	Participaton factors UX (N-mm)	UY (N-mm)	UZ (N-mm)	RX (N-mm)	RY (N-mm)	RZ (N-mm)	Modal Mass (N-mm-s2)	Modal Stiffness (N-mm)
1	5.62	4.09	0.00	-0.02	0	1002	-23	1	1245
2	6.80	-2.14	0.00	-1.21	1	13675	74	1	1828
3	7.97	-10.22	0.00	0.17	0	32514	-247	1	2509
4	9.59	13.94	0.00	-1.62	5	-255573	469	1	3632
5	10.06	-4.95	0.00	-5.70	-1	92933	-293	1	3997
6	12.43	-0.27	0.00	15.85	-6	14818	-215	1	6101
7	13.44	10.64	0.00	-0.28	2	380859	406	1	7129
8	15.81	0.00	-3.45	0.00	18515	1	-27078	1	9873
9	15.85	0.00	-1.31	0.00	7188	0	65490	1	9922
10	16.29	-0.03	0.74	0.00	-2251	-4	-12823	1	10470
11	16.32	0.02	-0.51	0.00	1453	-1	-11472	1	10519
12	17.43	0.09	-0.31	-0.02	914	-891	-71242	1	11988

4.5 The effect of pier settlement on the natural frequencies

The settlement of pillar no 2 from west was introduced into the Shell model of the bridge using the same approach as for the Beam element model. The displaced shape is shown in Figure 4.10. For the Beam element model the settlement had no apparent effect on the modal values evaluated, neither the frequency nor the mode shape. The case for the Shell element model was different, as introducing the settlement reduced the natural frequencies by 3% to 11% depending on modes. The effect was only 3-5% for modes 1, 2, 3, 4 and 7, slightly higher or 7-9% for modes 5 and 6, and then 8-11% for the torsional modes above 15 Hz.

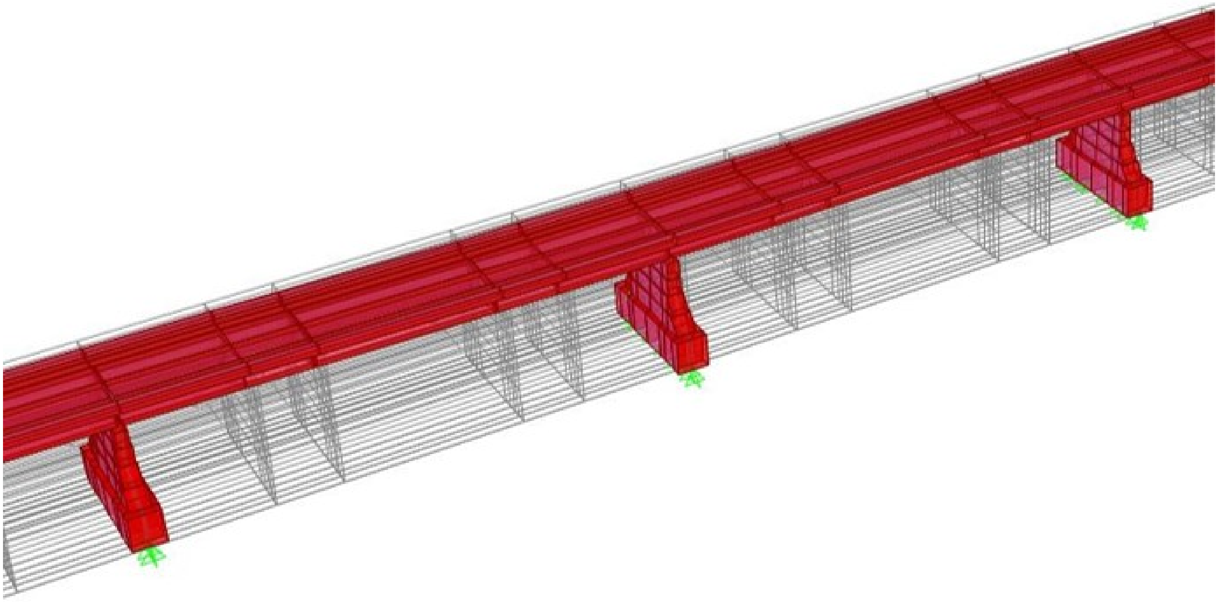

Figure 4.10: The pier settlement introduced to the Shell element model, version II.

This change also affects the mode shapes of the higher modes, which show a slightly different behavior then for the undeformed structure. The mode shapes of the lower frequency modes are not affected. The mode shapes of a model of a straight bridge can be seen in Appendix G.2 for comparison with the mode shapes from the deformed model shown in Appendix G.1. This effect was unexpected and has not been explained.

4.6 Static Analysis

Two static load cases were analyzed using the two element models (Beam and Shell). That is the case of a distributed concrete block loading at the center of span 2 from east and the nodal force loading of the Roto Merlo Truck on the same span. The static displacements from the Beam-element model and the Shell-element model are shown in Table 4.7 and compared with the displacement values from the LVDT full-scale measurements, presented in Chapter 2.

The FE models, both the Beam-element model and the Shell-element model, underestimate the displacements. The Beam model by 30% and the Shell model by 20%. The fact that the Shell model gives higher displacements than the Beam model indicates that the Shell element model provides a better simulation of the bridge behavior. Although it should be kept in mind that the displacement from the Shell model is taken from the bottom of the double T section where it was measured, whereas the beam displacement is based on the centroid of the girder section.

This difference between calculated and measured results might imply that the elasticity modulus used is too high for static analysis and should be lowered by about 20%. This is especially relevant since the bridge girder is cracked and fractured after about 65 years of use, and therefore the effective elastic modulus is surely lower than both the dynamic and static modulus which are primarily valid for unfractured sections.

However, the difference between calculated and measured displacements, may also suggest that the on-site displacement measurements include a rigid body displacement of the bridge section, meaning that when loaded, the pillars are displaced into the sand at the same time as the deck deforms, and the differential displacement between the sand and the deck is affected by this.

Table 4.7: Static displacements from the FE models and the LVDT measurements.

Load	Load type	Displacements, [mm]		
		Sap 2000 Beam model	Sap 2000 Shell model	Measured
Concrete blocks	Area load	0.7	0.8	1.0
Merlo Truck	Nodal loads	1.7	2.1	2.5

Appendix H provides some key diagrams from the static loading analysis which show the shear-force and moment distributions for both load cases (concrete blocks & truck) as calculated by the Beam-element model as well as the bending stresses due to the same two load cases and the dead-weight of the bridge, as evaluated by the Shell-element model.

4.7 Summary of the FE Modelling Process

The FE analysis of the bridge has focused on modal analysis to verify and consolidate the natural modes of vibration of the bridge. Two distinctly different finite element models have been created, using on one hand Beam elements and on the other Shell elements. Both models are found to show in principle similar dynamic behavior and provide comparable modal analysis results, at least for the lower modes of vibrations. However, the Shell element model has a natural three-dimensionality and is better equipped to demonstrate torsional tendencies, which are found to dominate the higher modes of vibration in the bridge.

To achieve a good comparison of natural frequencies with an OMA of the recorded acceleration data it was found imperative, for both the Beam model and the Shell model, to provide some longitudinal (axial) resistance at the end supports, and rotational stiffness about the transverse y-axis at the pillar supports. This was achieved by introducing appropriate spring elements at the supports.

Although both the Beam element model and the Shell element model gave in the end similar natural frequencies for the modes of vibration, the mode shapes for the first mode are seen to be quite different (see Appendix F and G). The Beam element model exaggerates the longitudinal movement associated with the mode, whereas the Shell model has a much more natural form. This is probably related to the offset created in the Beam model between the centroid of the deck cross-section and the top of the pillars. However, increasing the axial stiffness at the supports in the Beam model resulted in a natural frequency of the first mode that was too high. Perhaps a better approach than simply introducing the offset between pillar and deck, would have been to introduce a pseudo beam-column from the top of the pillars to the centroid of the section based on the reinforcement column built into the girder sides connecting them to the pillars. The effect of the offset between pillar and deck may also explain why a 10 times higher axial stiffness is required for the supports of the Shell model, than for the Beam model.

As the settlement of the second pillar from west induced some non-linear deformation behaviour of the deck girder at the neighbouring pillars, moment releases with a spring fixity were introduced at connection between the affected deck sections and the pillars in the Beam model, in order to investigate the influence of a possible "softness" of the deck girder passing over the pillars at the damaged end of the bridge. The resulting behaviour did not fit with the SI analysis, indicating that all pillars are currently supported in the same way and the deck girder responded elastically to the induced vibrations during both testing periods. The detailed analysis were therefore not described specifically in the previous sections.

Static analysis comparing measured and calculated displacements, from vehicle and concrete block loading on the second bridge span from east, gave lower values for the calculated loading. This is not unexpected due to several reasons, such as the effect from the choice of elastic modulus for the calculations and the imperfect measurement setup. The Shell model was found to give a better estimate of the maximum displacement than the Beam model.

5 Conclusion

5.1 Summary and discussion of results from FE- and OM-analysis

In Chapters 3 and 4, the bridge structure was analysed using operational modal analysis (OMA) based on recorded ambient acceleration response on one hand and secondly through finite element analysis (FEA). In this section the key results from each of the two chapters are compared and discussed further.

Naturally both these analysis phases were performed interactively, in the sense that in the finite element analysis notice was taken of the OMA results and vice versa the finite element analysis influenced to some extend the peak picking of the singular values in the spectral matrix. The results from each of the two methods are therefore not entirely independent.

The modal analysis results for both the final Beam-element model and Shell element model are compared in Table 5.1 in terms of the natural frequency. Table 5.1 further shows the natural frequencies and damping ratios from the OM analysis in Chapter 3, both from the MATLAB FDD toolbox and the ARTeMIS software. The OMA values in Table 5.1 are chosen from the results in Chapter 3 based on what is believed to be the best identification. For instance, the values for mode 1 are based on the analysis of the z-components of motion only, as the x-component was seen to disturb the proper estimation of the damping for that mode.

Table 5.1: Comparison of modes of vibration identified by OMA and FEA.

Finite Element Analysis				ARTeMIS OMA		MATLAB OMA	
Mode no.		BEAM	SHELL	FDD & EFFD		FDD/ITD	
Beam	Shell	f (Hz)	f (Hz)	f (Hz)	ζ (%)	f (Hz)	ζ (%)
1	1	5.72	5.62	5.73	0.94	5.68	1.40
2	2	6.91	6.80	6.67	1.09	6.68	0.90
3	3	7.96	7.97	8.13	0.82	8.07	1.46
4	4	9.50	9.59	9.73	1.29	9.74	1.37
-	5	-	10.06	10.12	0.34	-	-
5	-	11.27	-	11.16	1.54	11.09	1.27
-	-	-	-	11.96	1.57	12.17	1.27
6	6	12.39	12.43	12.42	1.17	12.26	2.69
7	-	13.08	-	-	-		
8	7	13.29	13.44	13.41	0.46		
9	-	13.66	-	-	-		

Only the first 7 to 9 modes evaluated by the FE models and the OMA are listed. This is because it was found during the FE-modelling that there were many closely spaced eigen frequencies above 13 Hz in the Beam element model and in the shell-element model there were many modes with closely spaced eigen frequencies and influenced by torsion, found above 15 Hz. These modes are not easily extracted from or identified by the ambient acceleration response data, although they could be noticed in some of the data-series studied using the ARTeMIS Software (see Table 3.1 and 3.2). They were however not pursued in the MATLAB based FDD analysis. Even so, it is seen that basically only the first 4 modes are consistently estimated by the OMA analysis. The visibility and identifiability of the higher modes depends on the data series and the frequency selection of the user. They are seen and picked in some of the recorded data series analysed but not in others.

The difference between the OMA and FEA results are considered to be within an acceptable range. There are some modes that are seen in the Beam-element model but not in the Shell-element model, such as Mode 5, with a frequency of 10.6 Hz in the Shell model but 11.27 Hz in the Beam model. Modes with similar frequencies are seen by the ARTeMIS software. Also, a mode with a frequency around 12 Hz is seen in the ambient data but not in the FE-models. Then a mode with frequency of 12.4 Hz is seen in both FE-models and the OMA. That mode is followed by a mode with frequency of 13.4 Hz, which is given by the Shell-element model and the ARTeMIS OMA, but not pursued in the MATLAB based analysis. The Beam element model on the other hand has many modes above 13 Hz, but not exactly at 13.4 Hz. The closest ones are at 13.29 Hz and 13.66 Hz, i.e. on either side of 13.4 Hz.

The estimated damping ratio is generally higher from the MATLAB based FDD analysis than from the EFDD analysis in ARTeMIS. On the average the damping is found to be in the expected range between one and two percent, and not a significant difference between the individual modes of vibration.

The ambient vibration data studied comes from two measurement periods, July 4, and August 28, 2019. The setup of the sensors was different on those two occasions, as shown in Appendix B. Also, there was much more water in the river and on the sand around the bridge in late August than in early July, as seen in Figures 1.1 and 1.2. The different water level may affect the foundation properties, as the sand/gravel is more saturated with water in August than in July. Furthermore, the measurements in July were taken during the day, with traffic on a nearby bridge and other minor activities around the bridge, whereas the measurements that were used from the August campaign were taken during the middle of the night, when the only source of environmental noise was the river and the weather. This explains the subtle differences in the two datasets and consequently the system identification, but the higher frequencies are more prominent in the July data than in the data from the night in August.

5.2 Conclusions

The objectives of this study were threefold. Firstly, to describe the bridge structure, the full-scale experiments, and available data. Secondly, to study the dynamic characteristics of the bridge based on recorded ambient acceleration data using the FDD method. Thirdly, to create finite element models of the bridge to interpret and simulate eigenvalues and mode shapes with the aim to find models that give a reasonable fit to the measured data. These objectives have largely been achieved, as described, and discussed in the preceding sections of this report.

The full-scale experiments that took place in the summer and fall of 2019 are summarized and reviewed in Chapter 2. The main focus has been on the measurements undertaken by RU staff, as those are the data that has been accessible for this study. In particular, it was decided in the early phases of this study to only make use of the ambient vibration response recorded at the site, rather than attempting some type of load modelling of a forced excitation, such as vehicles on the bridge, impact of concrete blocks or pounding by pile driving.

Operational modal analysis of the ambient response is discussed in Chapter 3, and a summary of the results is given in Table 5.1. The emphasis was on using the Frequency Domain Decomposition method [[33],[34], [23]]. On one hand the tried and tested ARTeMIS software was used, but for comparison and a more hands on experience, the MATLAB based Toolbox provided by Rune Brincker [23] was also applied. Basically, it can be said that the system identification provides reliable results for the first four modes, which are also those that are most prominent in the overview spectral plots shown in Chapter 2. Those four modes are vertical modes, controlled by rotation of the deck at the pillars and vertical displacement of the deck. However, mode 1 is also heavily influence by a longitudinal (x-component) motion, which is influenced by the longitudinal resistance at the end supports and the rotational stiffness of the pillar foundations. This characteristic was discovered through finite element-modelling of the bridge, which is discussed in Chapter 4.

Subtle differences were found between in the ambient acceleration data-sets used in the OMA which influenced the results of the system identification, with the higher frequency modes being more prominent in the July data than in the data from the night in August, as discussed in Chapter 3. This is thought to be related to the time of day of the measurements influencing the various activities around the bridge and different water levels in the river which may influence the stiffness of the foundation as well as the character of the dominant ambient excitation.

After various trials and testing, two different FE models were produced a Beam-element model and a Shell-element model. Both models give a good fit to the first four modes, but then for the higher modes they start to behave somewhat differently. Mainly because the Beam-element model lacks the three dimensionality of the Shell-element model, which has the capability of demonstrating the influence of torsion on the modes of vibration. This is particularly important for the open double-T cross sections of the bridge, but such cross-sections are quite prone to torsional vibrations. The shell model shows many closely spaced torsional modes at frequencies between 15 and 20 Hz, which were not investigated further, as they are not easily identified in the recorded ambient data. Possibly with more sensors, it would have been possible to track them in more detail.

5.3 Further Work

In a project like this there are always things that could have been done differently or more extensively, plus the various tasks that were not addressed at all. In the following paragraphs few of things of interest are mentioned for further work on the analysis of the bridge utilizing the data that has been gathered.

In this study, only selected time series of acceleration data have been analysed using the OMA approach. It would be of interest now that the key properties of the data have been established to do a systematic run through of all suitable acceleration data. This would require eliminating data with any direct forced vibration, as well as unexplained spikes in acceleration to insure adequate stationarity. The result should be a more reliable estimates of modal frequencies and modal damping through statistics of the evaluated values for all the data segments tested. It would further add to this picture if the acceleration data from the ETH sensors could be included. Especially regarding an accurate description of the vertical modes of vibration.

In this context it would also be of interest to try other system identification methods for comparison, such as some of the time-domain methods discussed in chapter 9 of [23]. For instance, the Stochastic subspace identification, which is also available in ARTeMIS.

The established modal information could be used for frequency response analysis of a model of the bridge. This would require load modelling of the forced excitation applied to the bridge, such as for the vehicles on the bridge, impact of concrete blocks or pounding by pile driving. Thereby the established modal damping could be validated, through comparison of recorded and calculated acceleration response. For this exercise the pile driving would probably be the best option for excitation simulation, since the cars driving on and off the bridge as well as the the block impact have of a relatively short duration and uncertain function. The velocity measurements on the sand might also be used as a bases for ambient ground motion excitation. Developing the appropriate load model is, however, not a straightforward task.

The acceleration response recorded during the pile driving could also be used for an input-output system identification of the deck vibrations. Where the two sensors on the pillars on each side of the span could provide the input signal and the three sensors on the deck span would provide the output signal. This could give an interesting additional characterisation of the key modes of the instrumented span.

The ultimate shear strength test that was done on the bridge in September 2019, is out of the scope of this report. However, there is a considerable work to be done in analysing that data and comparing it to a calibrated non-linear FE model of the bridge span tested, as well as to the current standardised formulation of shear strength.

The strain data measured using the fiber-gauges, is of particular interest for the ultimate shear test, if and when it becomes available. The fiber strain gauges also have dynamic capabilities and their data acquisition system sampled strain data at high speed. Therefore the strain data could provide an interesting addition to the acceleration data for operational modal analysis.

References

[1] Þ. V. Jónasdóttir, *The Steinavötn Bridge - A Full-Scale Test and Analysis*. Department of Civil Engineering, Technical University of Denmark, 2021, Master Thesis. [Online]. Available: `https://findit.dtu.dk/en/catalog/2693203824`.

[2] H. Sousa, "Advanced FE modeling supported by monitoring toward management of large civil infrastructures: The case study of Lezíria Bridge," *Structural Concrete*, vol. 21, no. 4, pp. 1309–1320, 2020. DOI: `https://doi.org/10.1002/suco.201900382`.

[3] A. Cunha, E. Caetano, F. Magalhães, and C. Moutinho, "Recent perspectives in dynamic testing and monitoring of bridges," *Structural Control and Health Monitoring*, vol. 20, no. 6, pp. 853–877, 2013. DOI: `https://doi.org/10.1002/stc.1516`.

[4] H. Li and J. Ou, "The state of the art in structural health monitoring of cable-stayed bridges," *Journal of Civil Structural Health Monitoring*, vol. 6, pp. 43–67, 2016. DOI: `https://doi.org/10.1007/s13349-015-0115-x`.

[5] J. Snæbjörnsson, J. Jakobsen, E. Cheynet, and J. Wang, "Full-scale monitoring of wind and suspension bridge response," *IOP Conference Series: Materials Science and Engineering*, vol. 276, p. 012 007, Dec. 2017. DOI: `10.1088/1757-899X/276/1/012007`.

[6] G. Webb, P. Vardanega, and C. Middleton, "Categories of SHM Deployments: Technologies and Capabilities," *Journal of Bridge Engineering*, vol. 20, p. 04 014 118, Nov. 2015. DOI: `10.1061/(ASCE)BE.1943-5592.0000735`.

[7] J. M. W. Brownjohn, P. Moyo, P. Omenzetter, and S. Chakraborty, "Lessons from monitoring the performance of highway bridges," *Structural Control and Health Monitoring*, vol. 12, no. 3-4, pp. 227–244, 2005. DOI: `https://doi.org/10.1002/stc.67`.

[8] D. Inaudi and B. Glisic, "Continuous monitoring of concrete bridges during construction and service as a tool for data-driven bridge health monitoring," Proceedings of the 3rd International Conference on Bridge Maintenance, Safety and Management - Bridge Maintenance, Safety, Management, Life-Cycle Performance and Cost, Taylor and Francis/ Balkema, 2006, pp. 421–422, ISBN: 0415403154. DOI: `10.1201/b18175-168`.

[9] G. V. Guðmundsson, "Burðargetumat steyptra brúa - Álagsprófun brúar á Steinavötn," ser. Rannsóknaráðstefna Vegagerðarinnar (Icelandic conference presentation), `https://www.vegagerdin.is/vefur2.nsf/Files/guemundur_valur_glaerur/$file/1115-1130%20Gu%C3%B0mundur%20Valur%20019.10.-Bur%C3%B0argeta%20steyptra%20br%C3%BAa.pdf`, 2019.

[10] A. Ragnarsson, *Burðarþolsrannsókn á brú yfir Steinavötn í Suðursveit*. Háskólinn í Reykjavík, 2019, Lokaverkefni í Tæknifræði (in Icelandic).

[11] CEN, *EN 1992-1-1:2004 Eurocode 2: Design of concrete structures*. European Committee for Standardization, Brussels, 2004.

[12] A. M. Neville, *Properties of Concrete*, 4th ed. John Wiley & Sons Inc., 1997.

[13] *MATLAB version 9.10.0 (R2021a)*. The MathWorks Inc., 2021, Natick, Massachusetts.

[14] S. Bonnefoy-Claudet, C. Cornou, P.-Y. Bard, F. Cotton, P. Moczo, J. Kristek, and D. Fäh, "H/v ratio: A tool for site effects evaluation. Results from 1-D noise simulations," *Geophysical Journal International*, vol. 167, pp. 827–837, Nov. 2006. DOI: `10.1111/j.1365-246X.2006.03154.x`.

[15] T. Kennedy, B. Halldorsson, J. Snæbjörnsson, and R. Green, "Influence of gravel fill on the seismic response characteristics of sites in Iceland," 17th European Conference

on Soil Mechanics and Geotechnical Engineering (ECSMGE - 2019), Reykjavik, Iceland, Sep. 2019. DOI: `10.32075/17ECSMGE-2019-0471`.

[16] B. Bessason, *SAWS Mælingar*. University of Iceland, (website in Icelandic). [Online]. Available: `https://notendur.hi.is/~bb/sasw/`.

[17] G. Gazetas, "Foundation Vibrations," in *Foundation Engineering Handbook*, H.-Y. Fang, Ed. Boston, MA: Springer US, 1991, pp. 553–593, ISBN: 978-1-4757-5271-7. DOI: `10.1007/978-1-4757-5271-7_15`.

[18] CEN, *EN 1997-2:2007 Eurocode 7 - Geotechnical design - Part 2: Ground investigation and testing*, 3rd ed. European Committee for Standardization, Brussels, 2007.

[19] H. Abuel-Naga, A. Bouazza, and M. Holtrigter, "On use of dynamic probing in sandy soils," *Lowland Technology International*, vol. 13, pp. 40–50, Dec. 2011.

[20] A. K. Chopra, *Dynamics of Structures: Theory and applications to earthquake engineering*, 3rd ed. Berkeley: Pearson Education, Inc., 2007.

[21] R. W. Clough and J. Penzien, *Dynamics of Structures*, 2nd ed. McGraw-Hill Inc., 1993.

[22] E. L. Wilson, *Three-Dimensional Static & Dynamic Analysis of Structures: A Physical Approach with Emphasis on Earthquake Engineering*, 3rd ed. Computers and Structures, 2002, ISBN: 0-923907-00-9.

[23] R. Brincker and C. E. Ventura, *Introduction to Operational Modal Analysis*. John Wiley & Sons, Ltd, 2015, ISBN: 9781118535141. DOI: `https://doi.org/10.1002/9781118535141.ch1`.

[24] L. Meirovitch, *Fundamentals of Vibrations*. McGraw-Hill Book Co., 2001.

[25] C. E. Beards, *Structural Vibration: Analysis and Damping*. Arnold, 1996, ISBN: 0 340 64580 6.

[26] R. Brincker, C. Ventura, and P. Andersen, "Damping estimation by frequency domain decomposition," In proceedings of the 19th International Modal Analysis Conference (IMAC), February 5–8, Kissimmee, Florida, 2001, pp. 698–703.

[27] *ARTeMIS Modal Pro, version 7.0.0.5*. Structural Vibration Solutions A/S, 2021, NOVI Science Park, Aalborg Denmark.

[28] *Sap2000, version 19.2, Structural Analysis and Design*, Computers & Structures Inc. [Online]. Available: `https://www.csiamerica.com/products/sap2000`.

[29] R. W. Clough, "Early history of the finite element method from the view point of a pioneer," *International Journal for Numerical Methods in Engineering*, vol. 60, no. 1, pp. 283–287, 2004. DOI: `https://doi.org/10.1002/nme.962`.

[30] D. L. Logan, *A first course in the finite element method*, 4th ed. Thomson, 2007, ISBN: 0-534-55298-6.

[31] H. Bogason, *Tjónagreining á brúnni yfir Steinavötn í Suðursveit*, Icelandic. Umhverfis- og byggingarverkfræðideild, Háskóli Íslands, 2018, (Msc thesis in Icelandic).

[32] R. Dobry and G. Gazetas, "Simple method for dynamic stiffness and damping of floating pile groups," *Géotechnique*, vol. 38, no. 4, pp. 557–574, 1988. DOI: `10.1680/geot.1988.38.4.557`.

[33] R. Brincker, L. Zhang, and P. Andersen, "Modal Identification from Ambient Response Using Frequency Domain Decomposition," Proceedings of the 18th International Modal Analysis Conference. San Antonio, TX, 2000.

[34] R. Brincker, L. Zhang, and P. Andersen, "Modal identification of output only systems using Frequency Domain Decomposition," *Smart Materials and Structures*, vol. 10, p. 441, Jun. 2001. DOI: `10.1088/0964-1726/10/3/303`.

A Bridge Geometry

The following drawings of the bridge geometry are provided by the Icelandic Road and Coastal Administration and are the original drawings from the year 1964.

A.1 Bridge layout

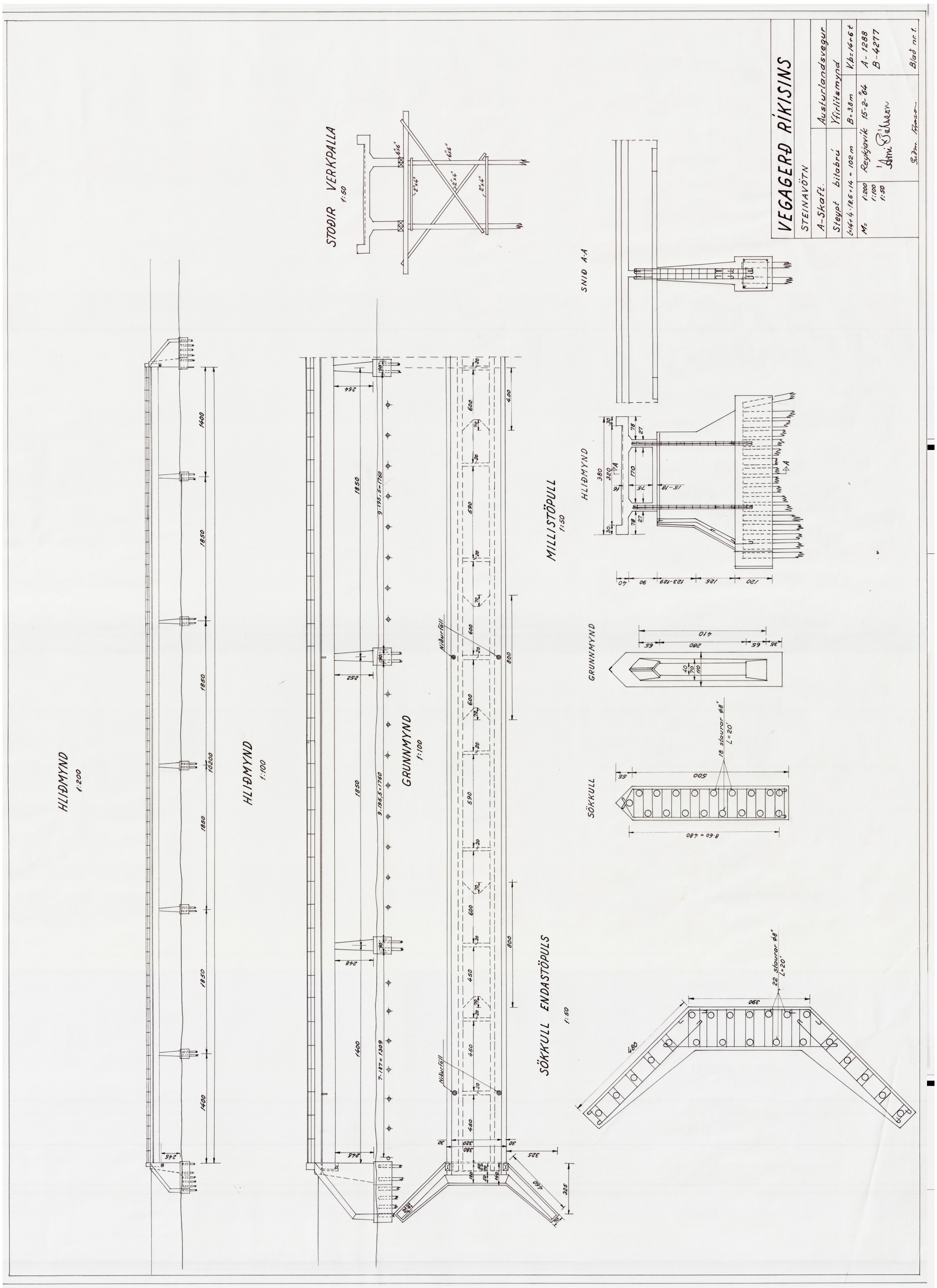

A.2 Reinforcement of end- and intermediate-pillars

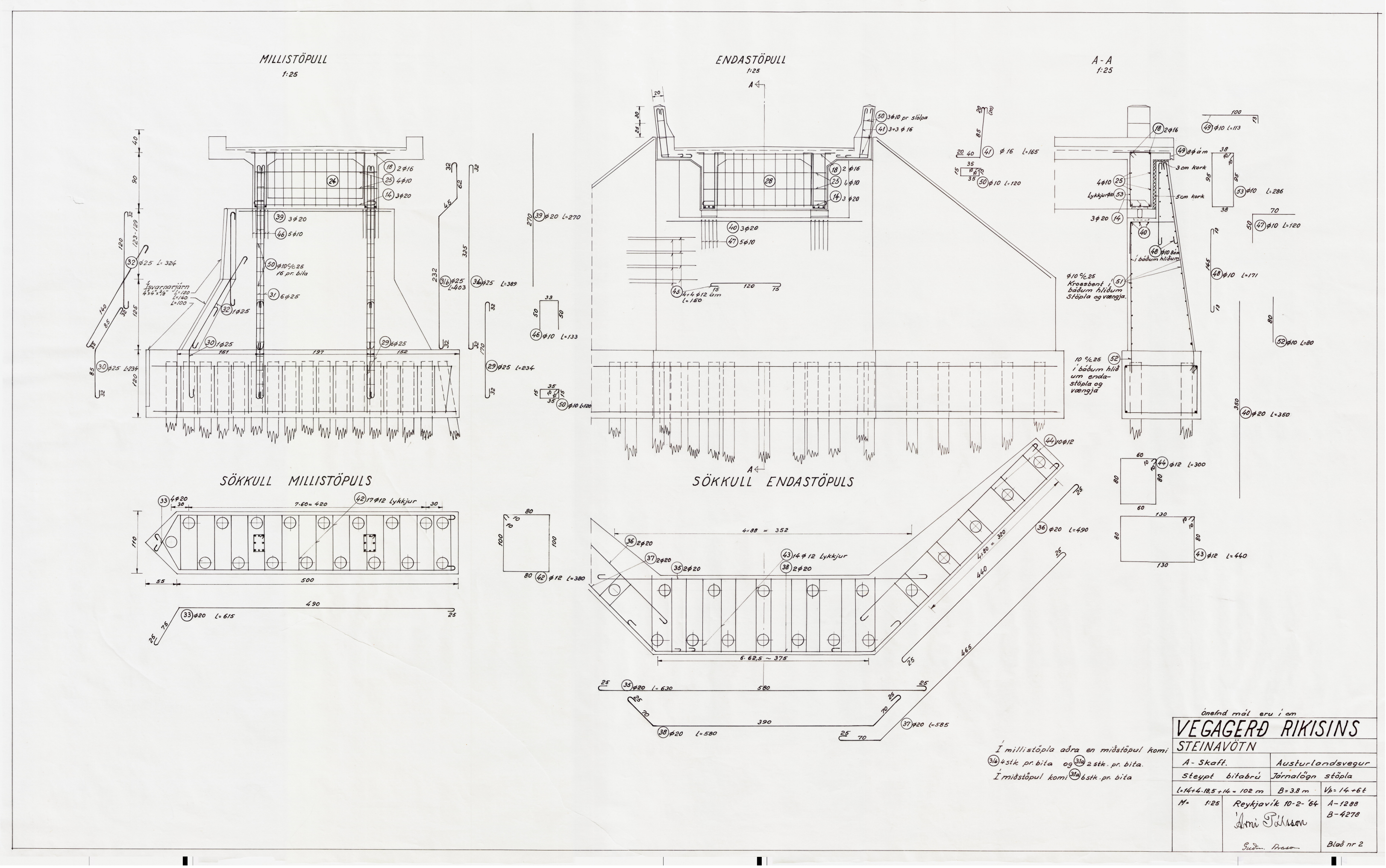

Í millistöpla aðra en miðstöpul komi (31b) 4stk pr. bita og (31a) 2 stk. pr. bita.
Í miðstöpul komi (31a) 6stk. pr. bita

A.3 Reinforcement of beam- and deck-elements

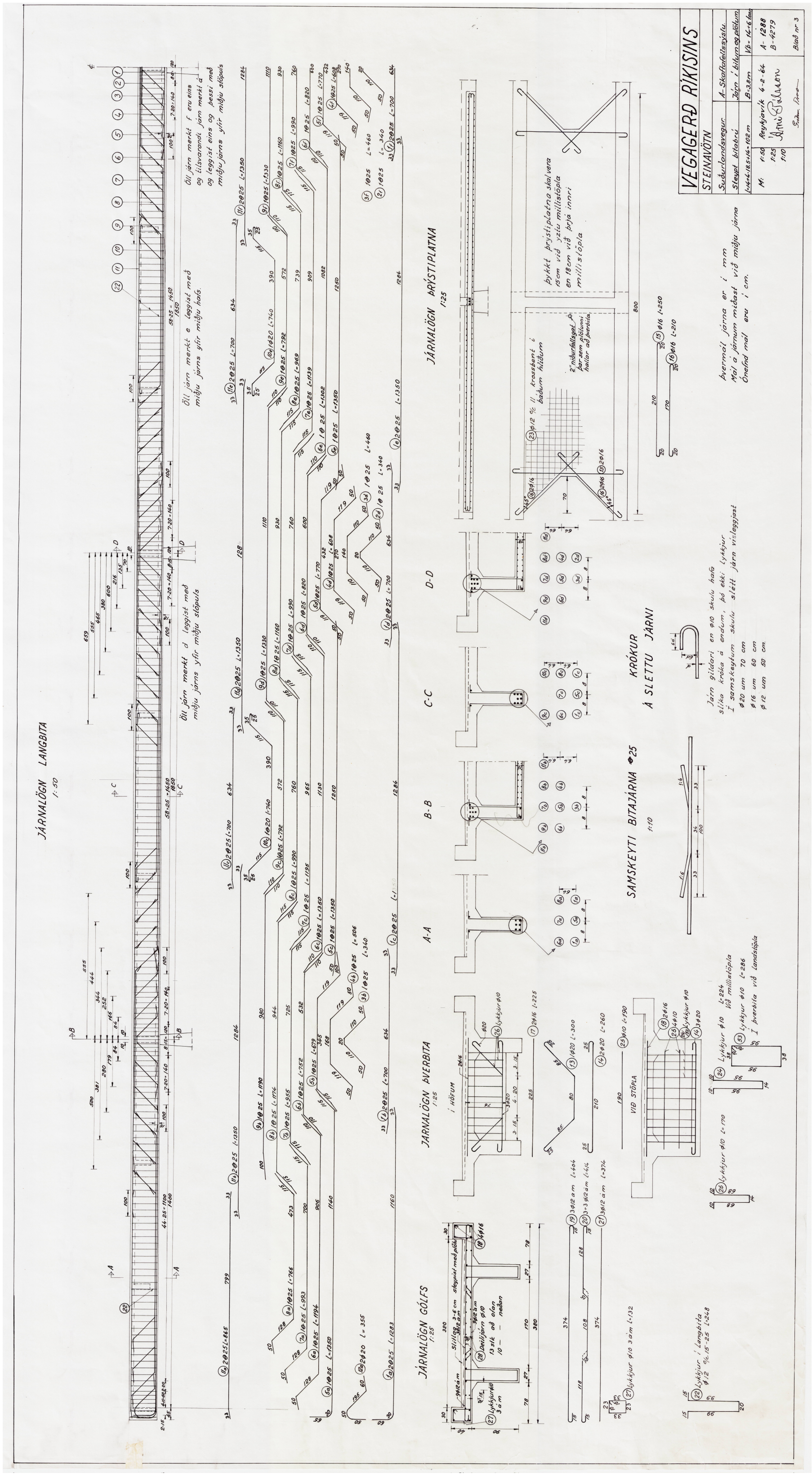

B Positioning of Accelerometers

The following drawings are The following drawings are provided by the Icelandic Road and Coastal Administration and have been modified to show the positioning of the accelerometers during testing in July and August.

B.1 July positioning of accelerometers

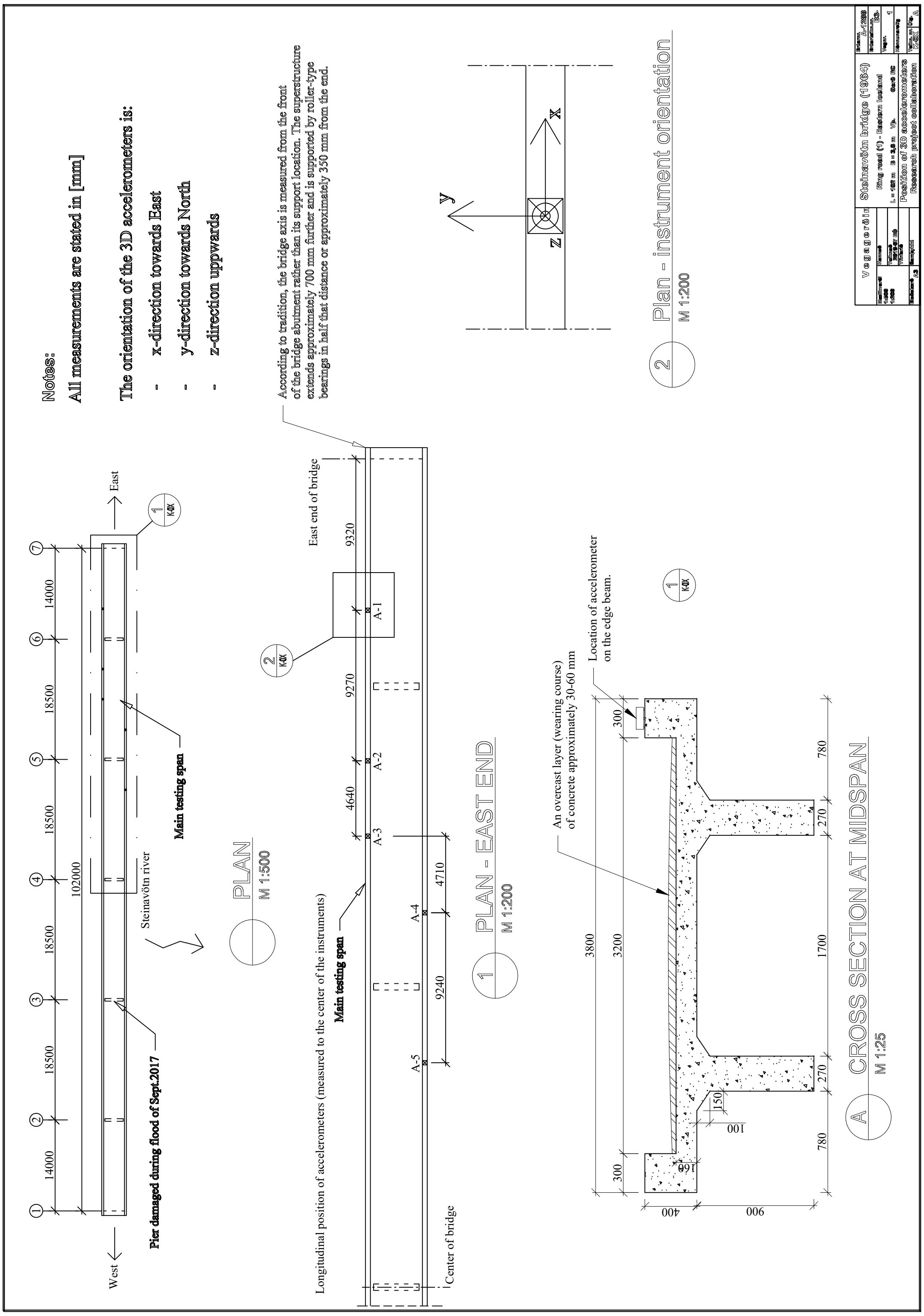

B.2 August positioning of accelerometers

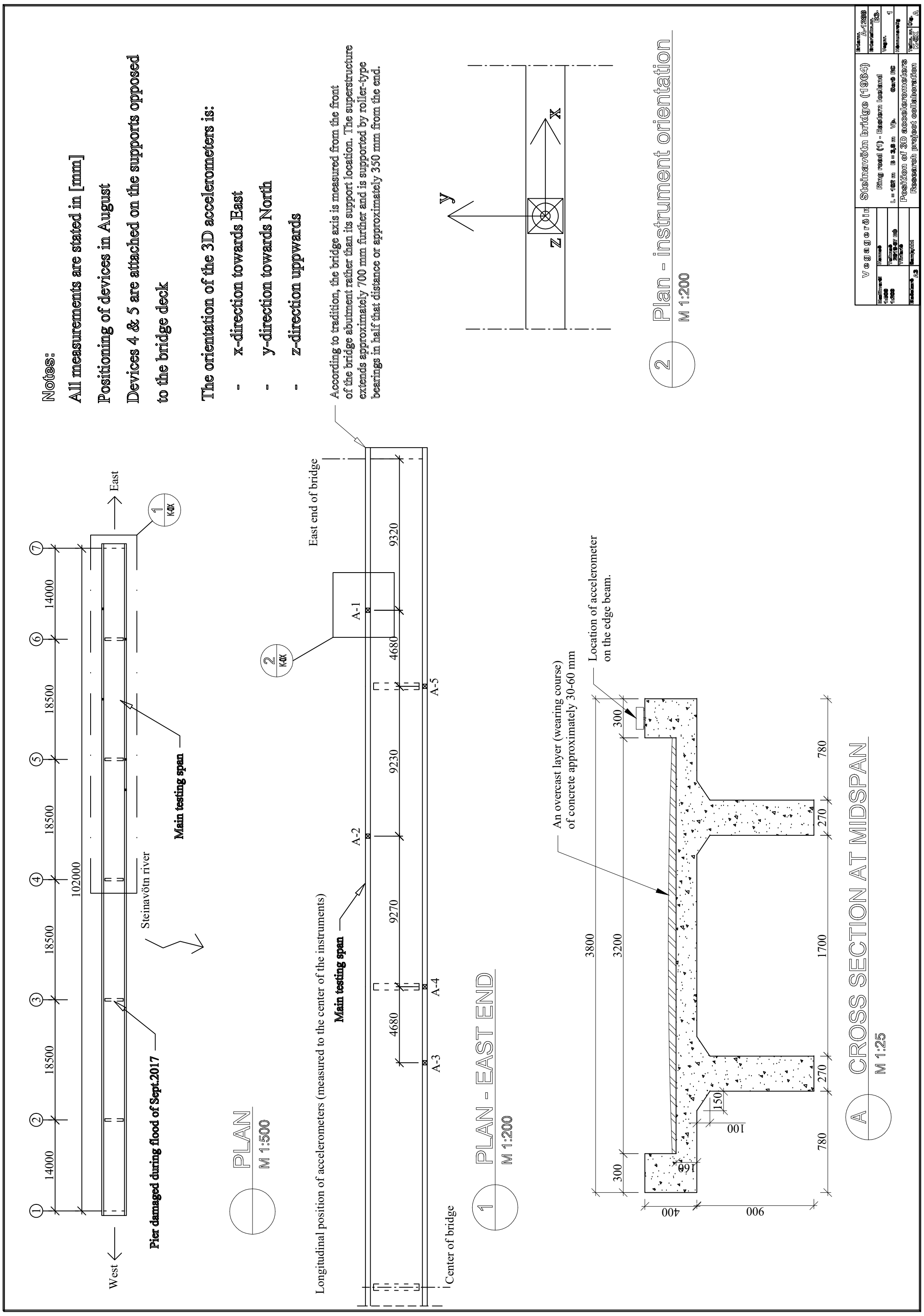

C Measurements of the dynamic elasticity modulus

Table C.1: Measurement results from Ultrasonic measurements of different concrete sections of the bridge over Steinavötn (July 4, 2019).

Location	**Time**	**Thickness**	**Velocity**	**Poisson's ratio**	**Density**	**Elasticity modulus**
	µs	mm	m/s	-	kg/m^3	GPa
1st pillar from eastern end	117.0	535	4572.65	0.2	2500	47.05
	133.9	565	4219.57	0.2	2500	40.06
	127.4	540	4238.62	0.2	2500	40.42
	117.3	515	4390.45	0.2	2500	43.37
	133.9	590	4406.27	0.2	2500	43.68
2nd pillar from eastern end	132.4	620	4682.78	0.2	2500	49.34
	129.5	580	4478.76	0.2	2500	45.13
	142.6	560	3927.07	0.2	2500	34.70
Deck beam from top						
By accelerometer #1	73.5	300	4081.63	0.2	2500	37.48
By accelerometer #2	72.8	300	4120.88	0.2	2500	38.21
By accelerometer #3	76.7	300	3911.34	0.2	2500	34.42
By accelerometer #4	69.8	300	4297.99	0.2	2500	41.56
By accelerometer #5	73.3	300	4092.77	0.2	2500	37.69
Deck beam from bottom						
South side, center span #2 from east.	66.5	270	4060.15	0.2	2500	37.09
	63.5	270	4251.97	0.2	2500	40.68
North side, center span #2 from east.	69.5	270	3884.89	0.2	2500	33.96
	68.7	270	3930.13	0.2	2500	34.75
	68.4	270	3947.37	0.2	2500	35.06

Table C.2: Average values for the modulus of elasticity for the different bridge sections.

	The bridge deck	The Pillars	Combined value
Average value (GPa)	37.1	43.0	39.70
Standard deviation (GPa)	2.6	4.6	4.6
Median value (GPa)	37.3	43.5	39.1
Minimum value (GPa)	34.0	34.7	34.0
Maximum value (GPa)	41.5	49.3	49.3

D Borro Drilling

The following document shows the result from a soil-mechanical testing in the form of a Borro drilling test performed by IRCA in October 2017. The location of the test was 16m away from the eastern end of the bridge.

Vegagerdin

Hola 4

Fskj. 2

Unnið af Vegagerðin

Heiti verks Steinavötn

Verknúmer

Staðsetning Suðursvæði

Upplýsingar um borholu

Dagsetning borunar: 19.10.2017

Skráð af: AKS

Boraðferð: Borro borun

Hnit og hæð:
(ÍSN93/WGS84)
X= 649040
Y= 409855
Z=

Athugasemdir:

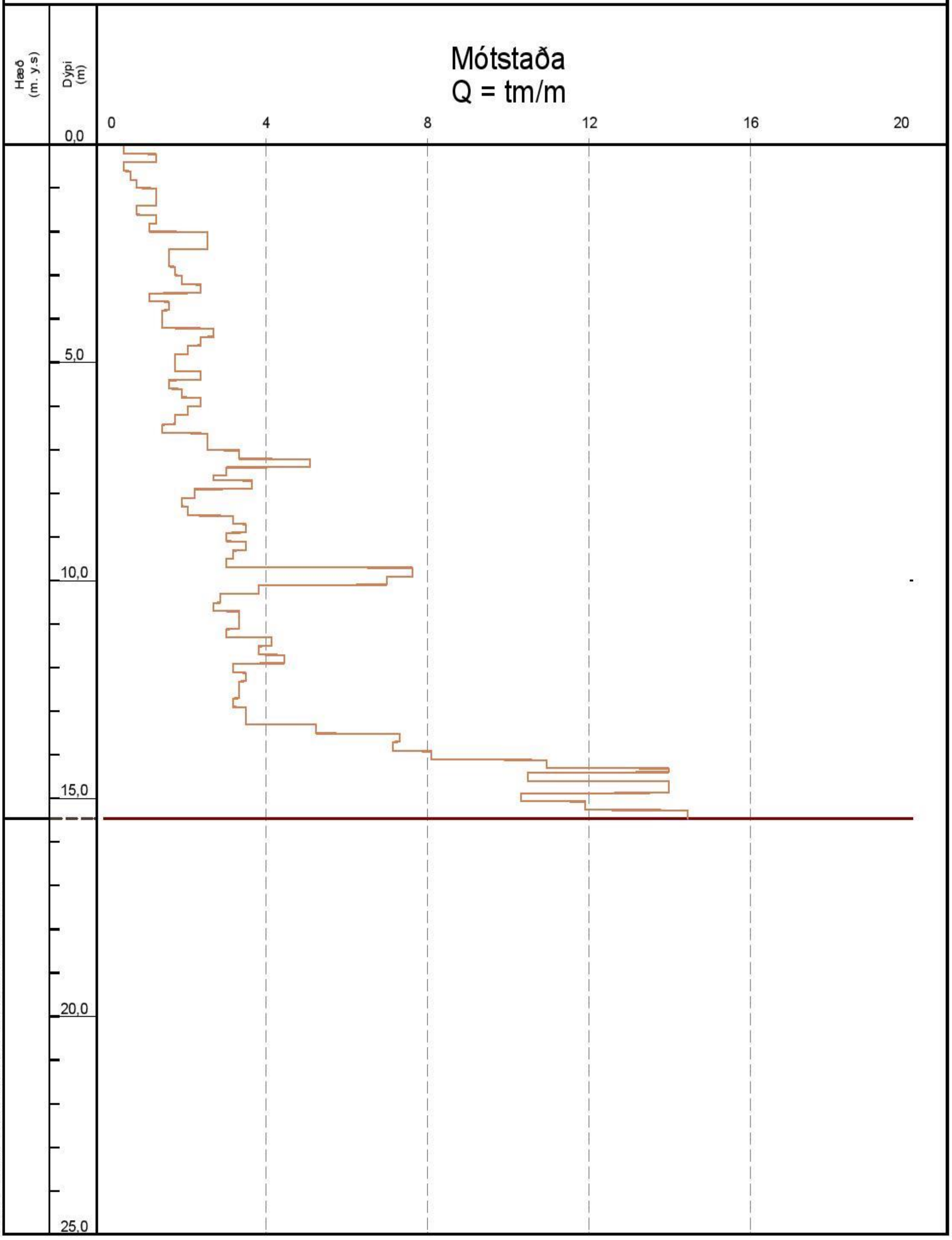

BORRO BORUN STEINAVÖTN.GPJ GINT STD A4.GDT 16.11.17

E Artemis - OMA Plots

Appendix E contains plots of Singular values of the spectral matrices of all the data series 1) before the peak picking, 2) after peak picking for the FDD analysis and 3) after peak picking for the EFDD analysis.

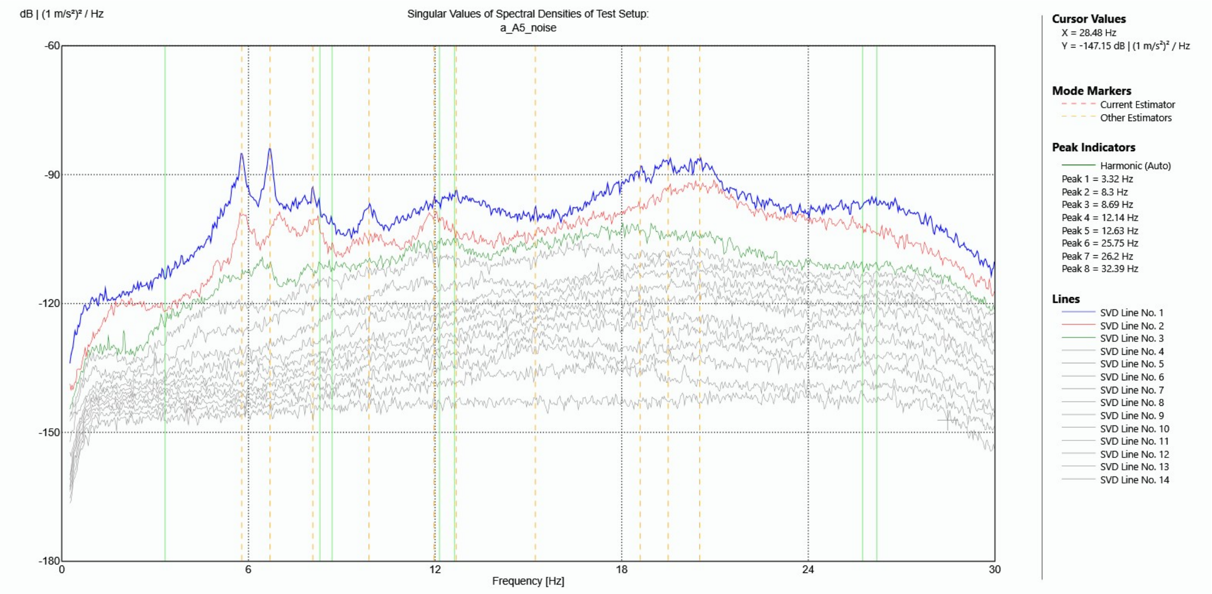

Figure E.1: Singular values of spectral densities [dB rel. to m^2/s^3] as a function of frequency [Hz] for the 10-minute data segment from August 2019 before peak picking of potential modal frequencies.

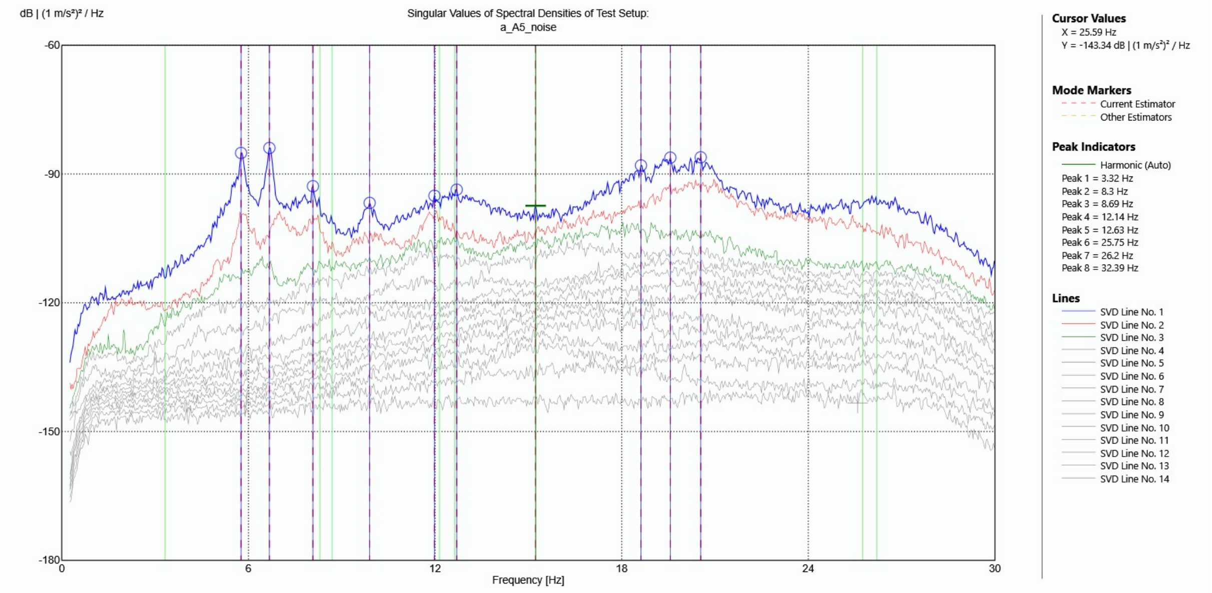

Figure E.2: Singular values of spectral densities [dB rel. to m^2/s^3] as a function of frequency [Hz] for the 10-minute data segment from August 2019 after peak picking of potential modal frequencies for the FDD.

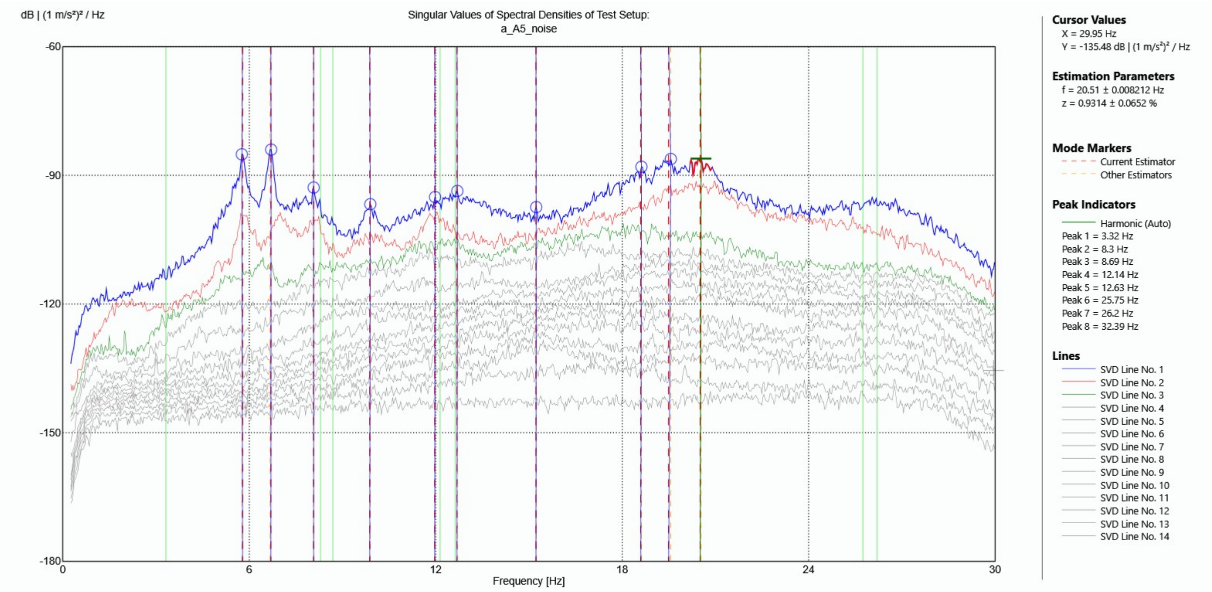

Figure E.3: Singular values of spectral densities [dB rel. to m^2/s^3] as a function of frequency [Hz] for the 10-minute data segment from August 2019 after peak picking of potential modal frequencies for the EFDD.

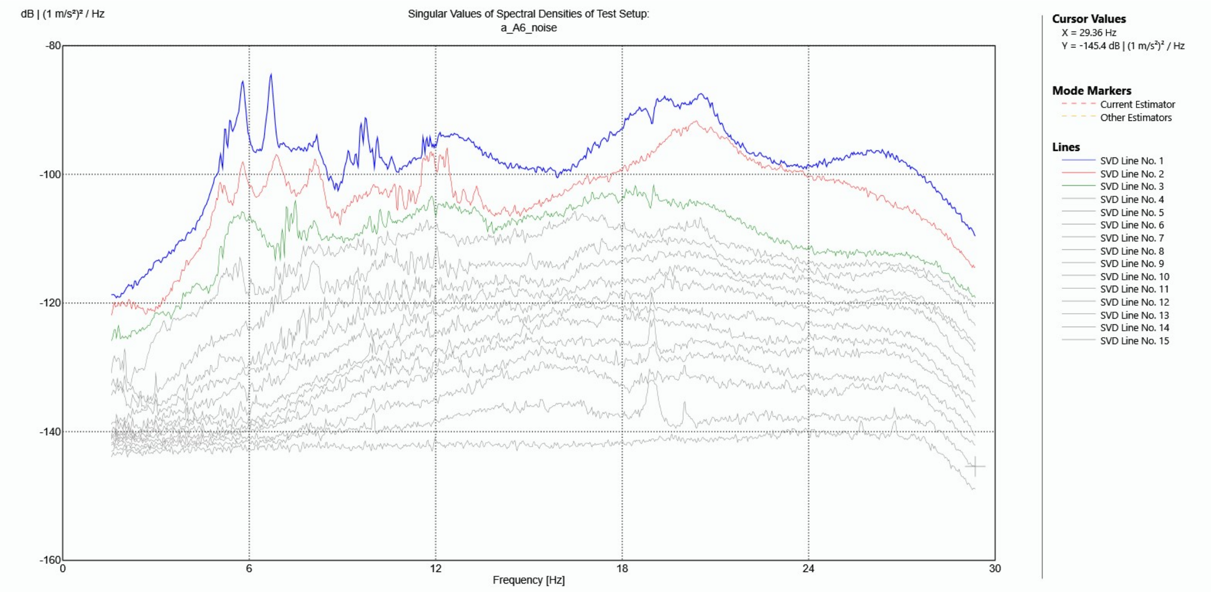

Figure E.4: Singular values of spectral densities [dB rel. to m^2/s^3] as a function of frequency [Hz] for the 1-hour data segment from August 2019 before peak picking of potential modal frequencies.

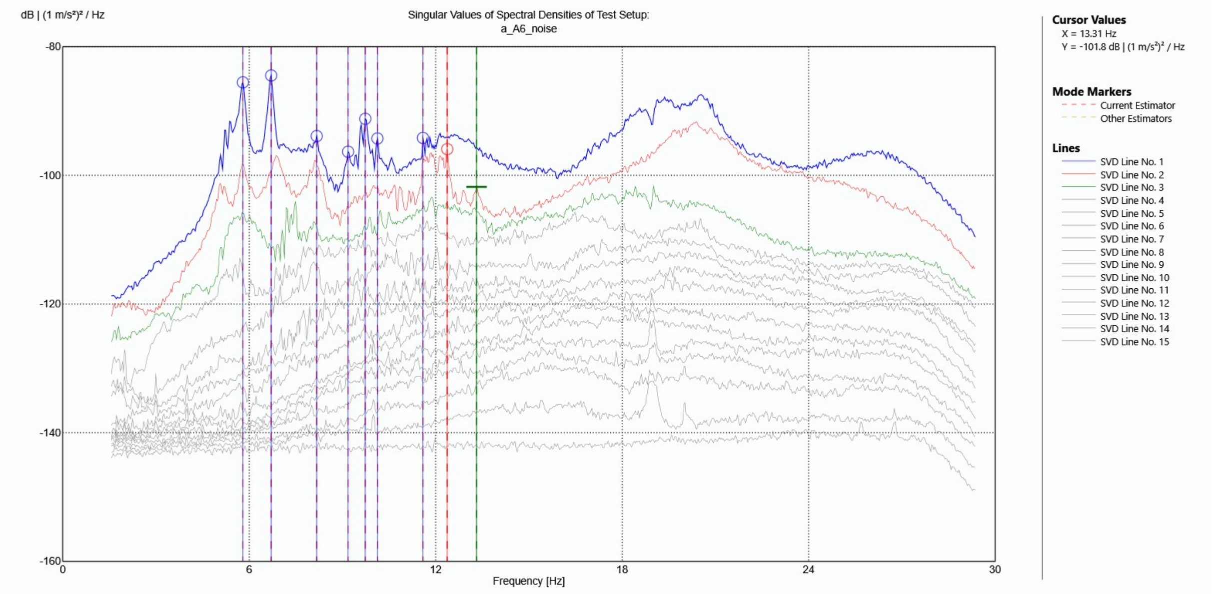

Figure E.5: Singular values of spectral densities [dB rel. to m^2/s^3] as a function of frequency [Hz] for the 1-hour data segment from August 2019 before peak picking of potential modal frequencies for the FDD.

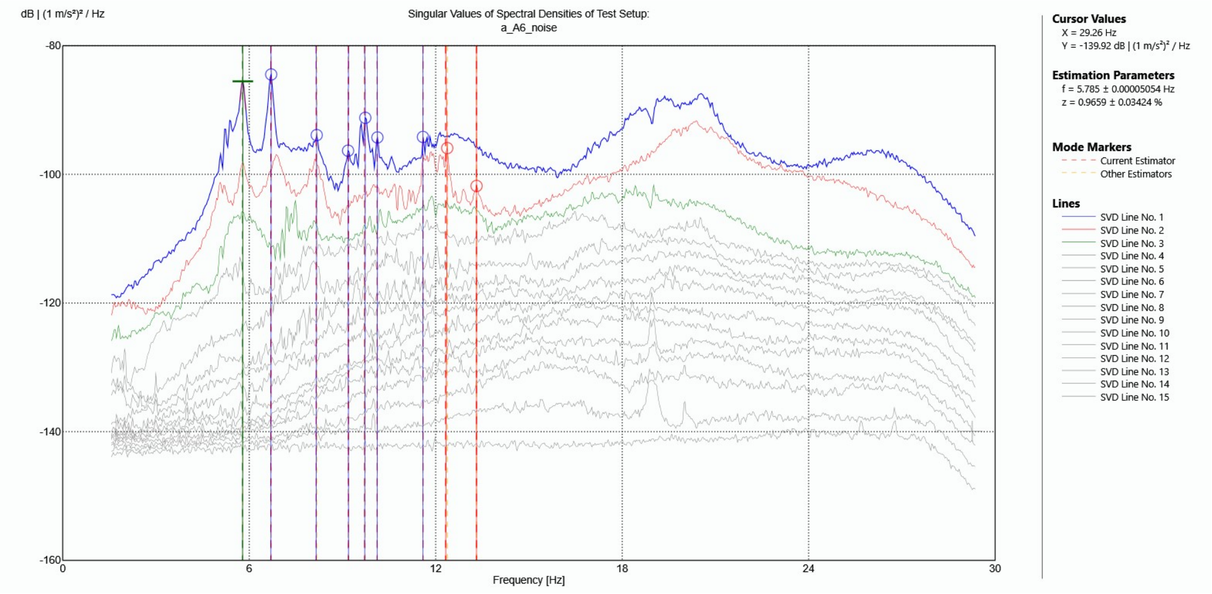

Figure E.6: Singular values of spectral densities [dB rel. to m^2/s^3] as a function of frequency [Hz] for the 1-hour data segment from August 2019 before peak picking of potential modal frequencies for the EFDD.

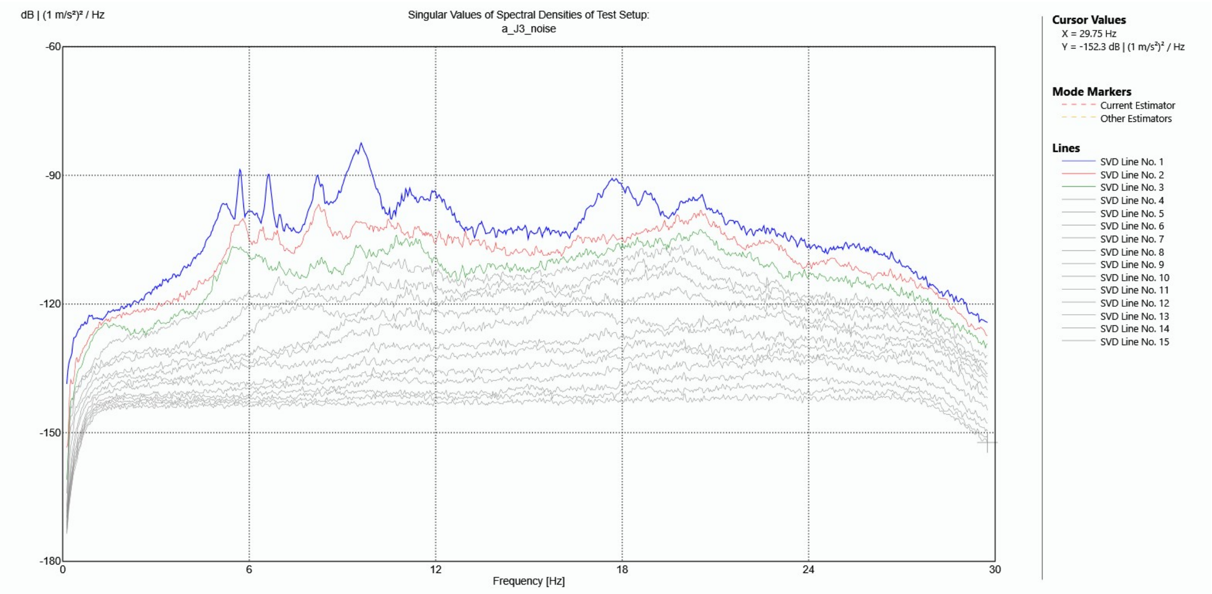

Figure E.7: Singular values of spectral densities [dB rel. to m^2/s^3] as a function of frequency [Hz] for the 30-minute data segment from July 2019 before peak picking of potential modal frequencies.

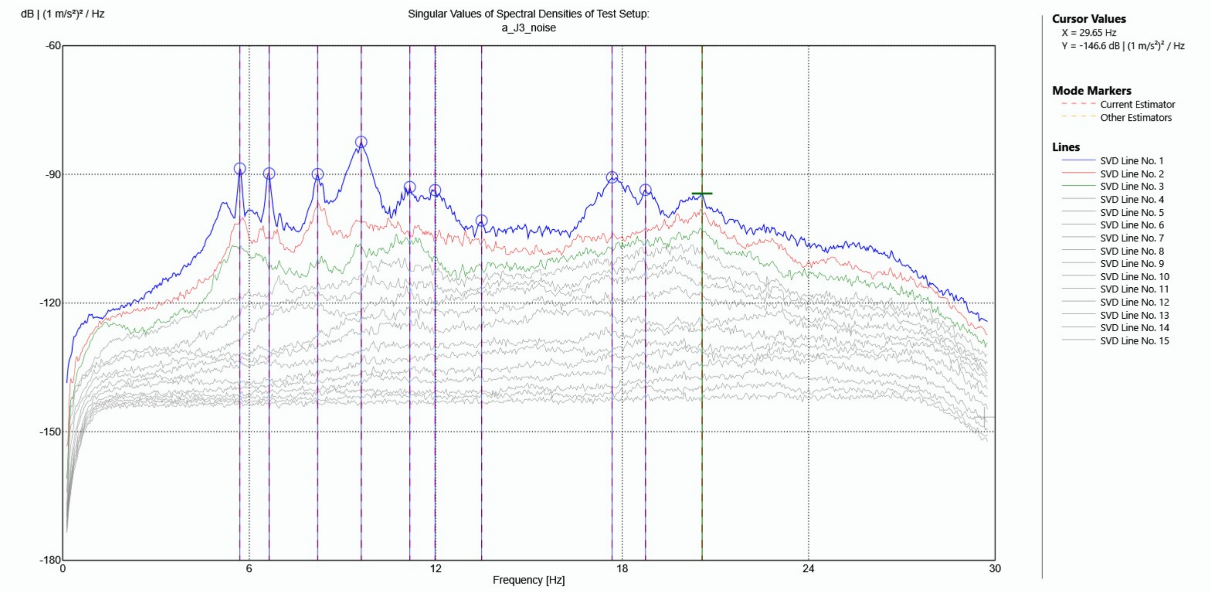

Figure E.8: Singular values of spectral densities [dB rel. to m^2/s^3] as a function of frequency [Hz] for the 30-minute data segment from July 2019 before peak picking of potential modal frequencies for the FDD.

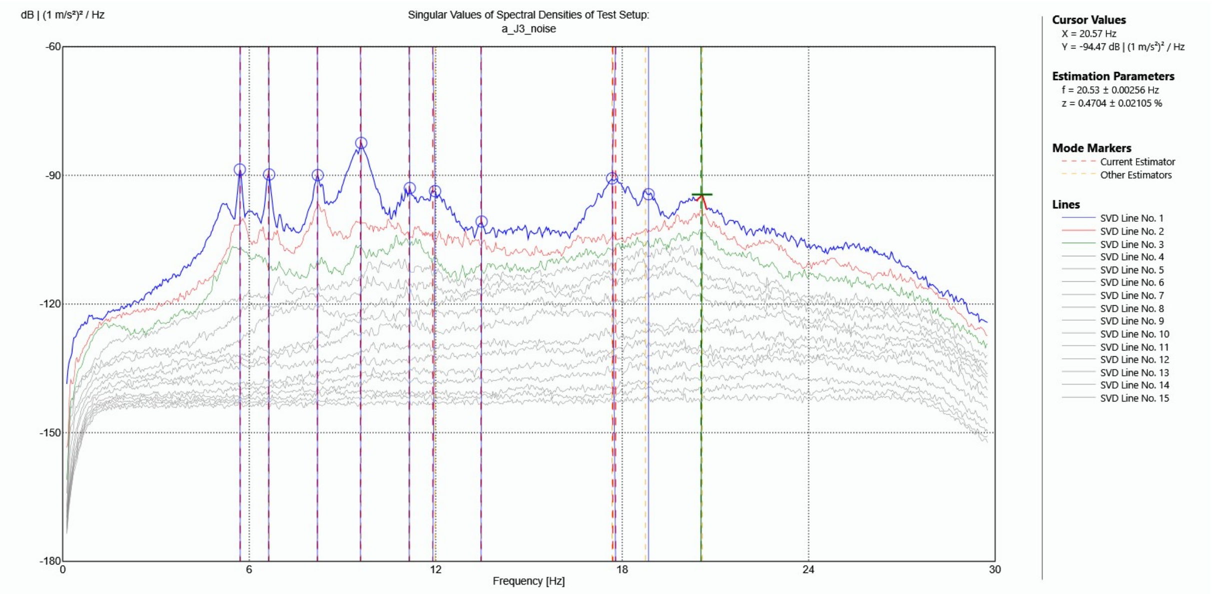

Figure E.9: Singular values of spectral densities [dB rel. to m^2/s^3] as a function of frequency [Hz] for the 30-minute data segment from July 2019 before peak picking of potential modal frequencies for the EFDD.

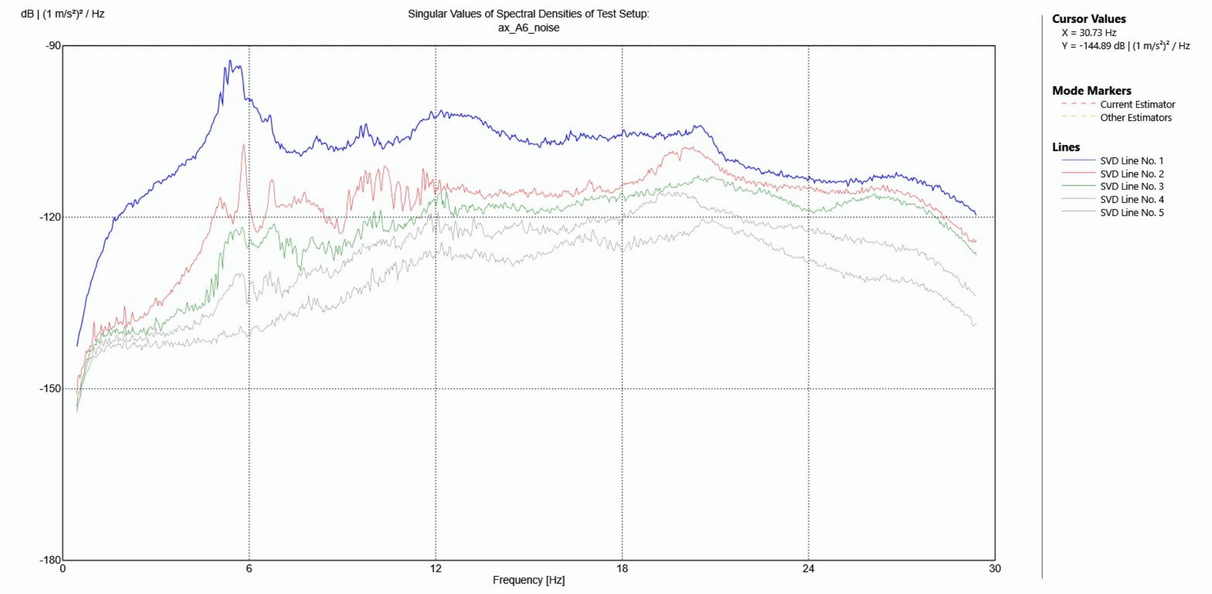

Figure E.10: Singular values of spectral densities [dB rel. to m^2/s^3] as a function of frequency [Hz] for the 1-hour data segment (x-direction) from August 2019 before peak picking of potential modal frequencies.

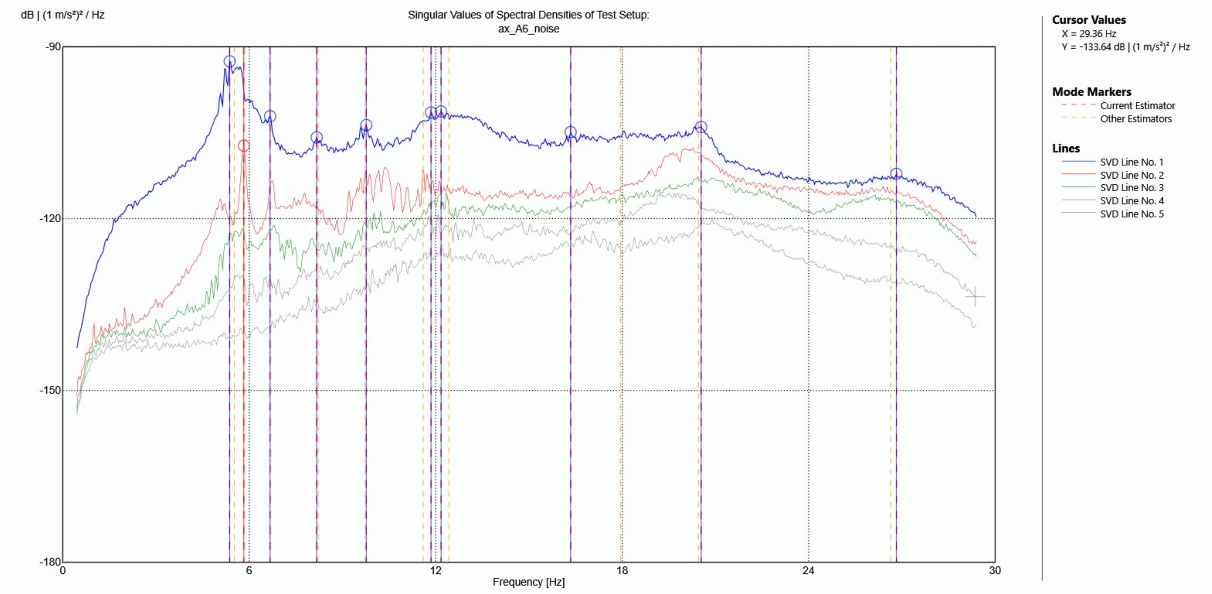

Figure E.11: Singular values of spectral densities [dB rel. to m^2/s^3] as a function of frequency [Hz] for the 1-hour data segment (x-direction) from August 2019 before peak picking of potential modal frequencies for the FDD.

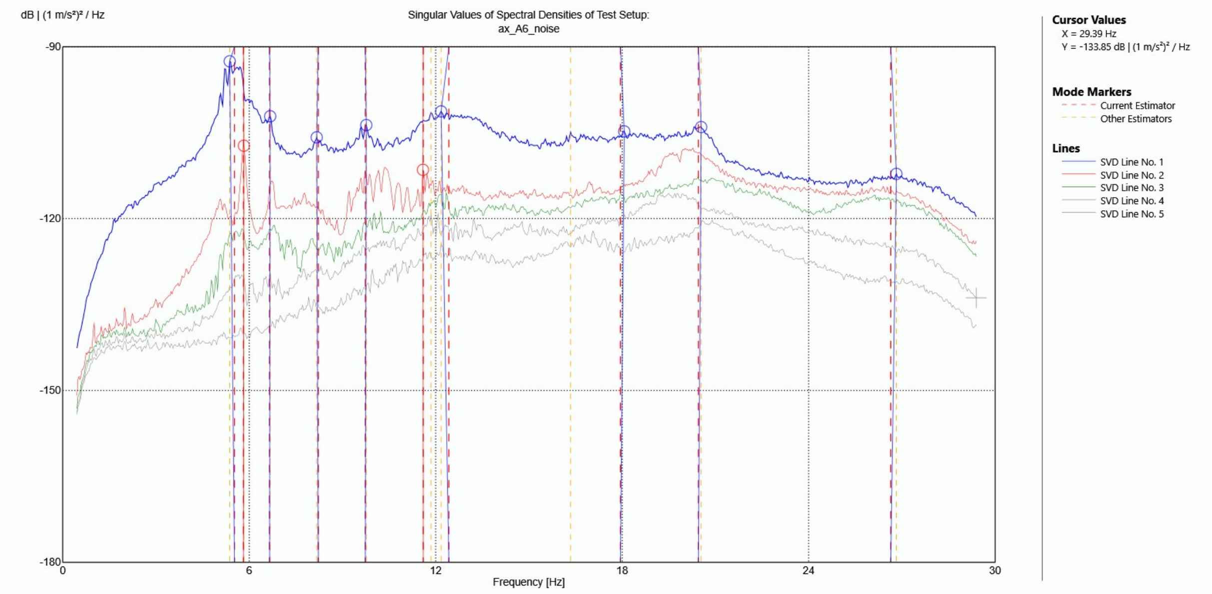

Figure E.12: Singular values of spectral densities [dB rel. to m^2/s^3] as a function of frequency [Hz] for the 1-hour data segment (x-direction) from August 2019 before peak picking of potential modal frequencies for the EFDD.

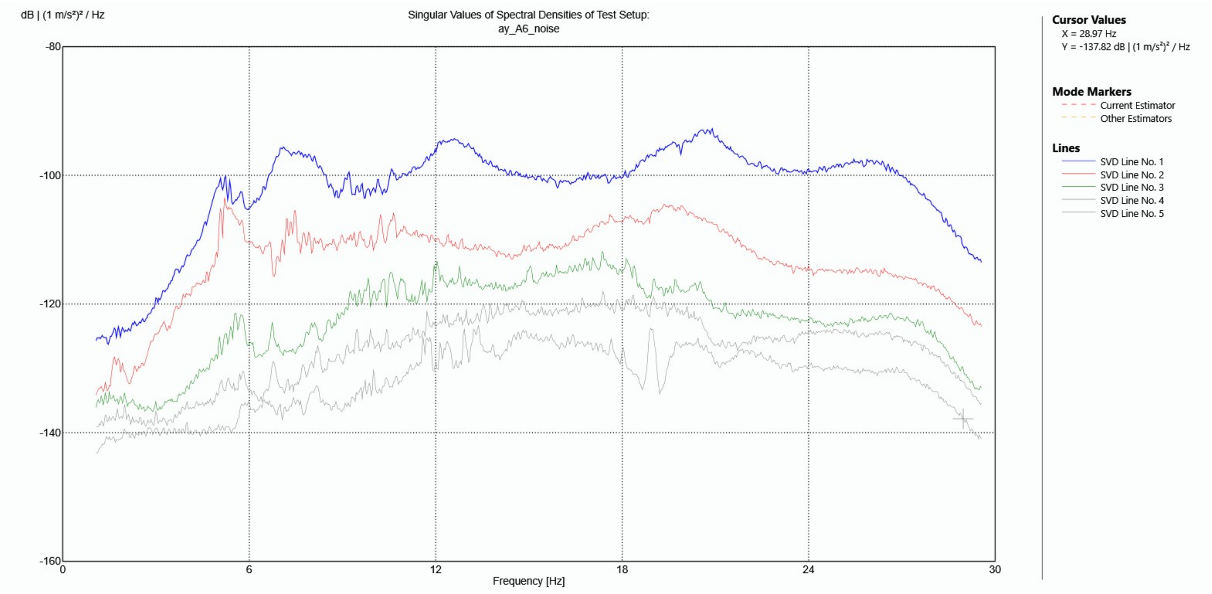

Figure E.13: Singular values of spectral densities [dB rel. to m^2/s^3] as a function of frequency [Hz] for the 1-hour data segment (y-direction) from August 2019 before peak picking of potential modal frequencies.

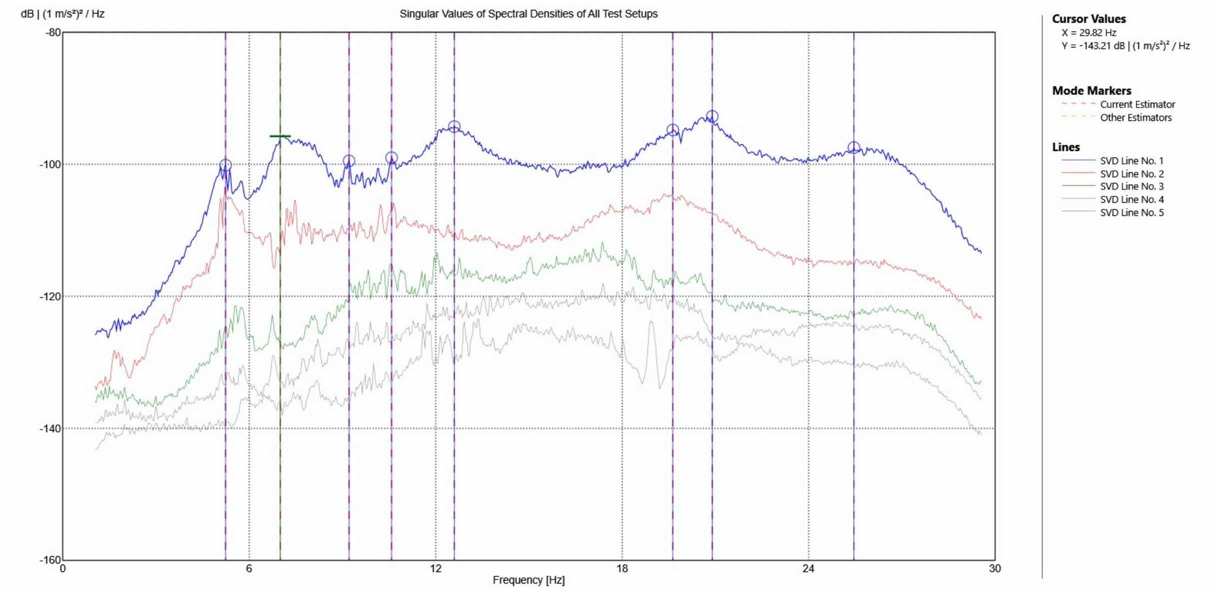

Figure E.14: Singular values of spectral densities [dB rel. to m^2/s^3] as a function of frequency [Hz] for the 1-hour data segment (y-direction) from August 2019 before peak picking of potential modal frequencies for the FDD.

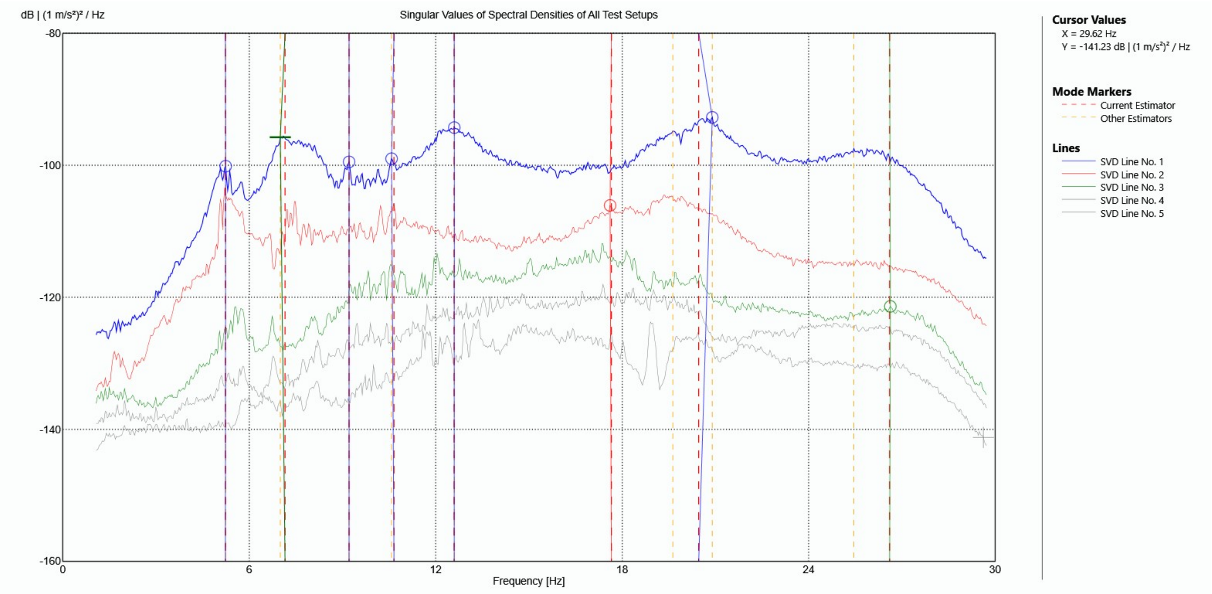

Figure E.15: Singular values of spectral densities [dB rel. to m^2/s^3] as a function of frequency [Hz] for the 1-hour data segment (y-direction) from August 2019 before peak picking of potential modal frequencies for the EFDD.

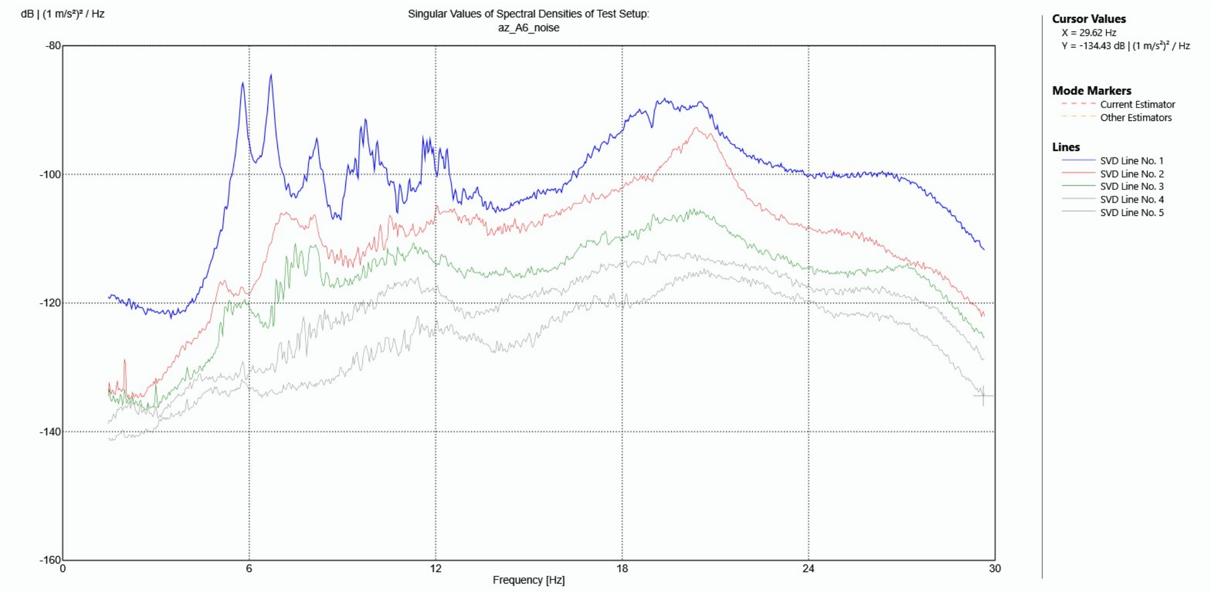

Figure E.16: Singular values of spectral densities [dB rel. to m^2/s^3] as a function of frequency [Hz] for the 1-hour data segment (z-direction) from August 2019 before peak picking of potential modal frequencies.

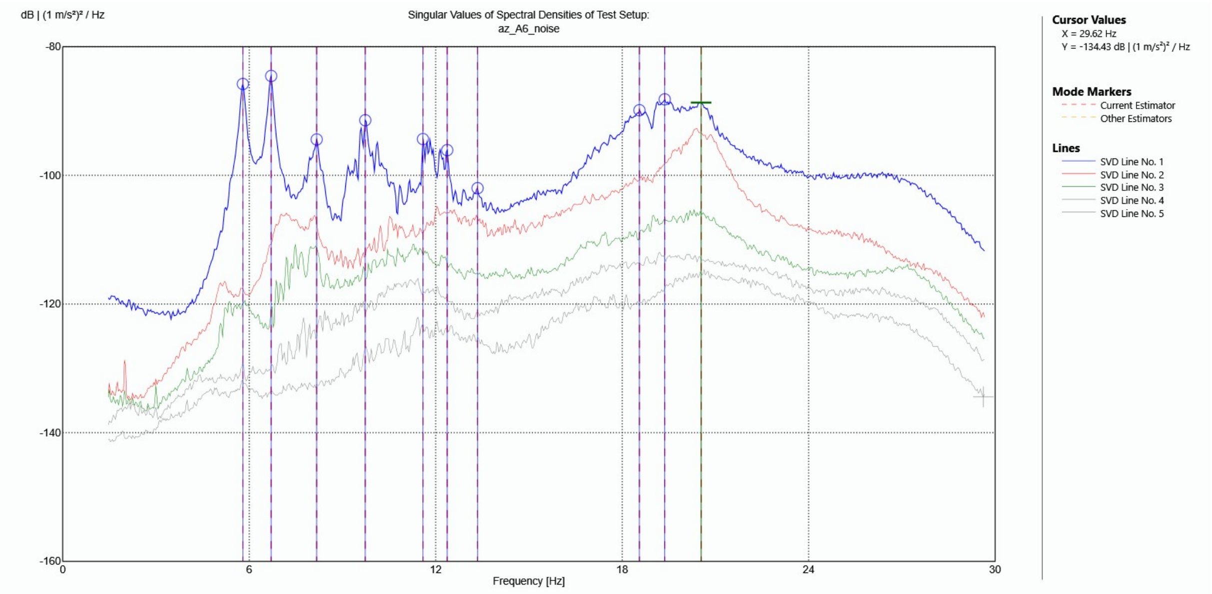

Figure E.17: Singular values of spectral densities [dB rel. to m^2/s^3] as a function of frequency [Hz] for the 1-hour data segment (z-direction) from August 2019 before peak picking of potential modal frequencies for the FDD.

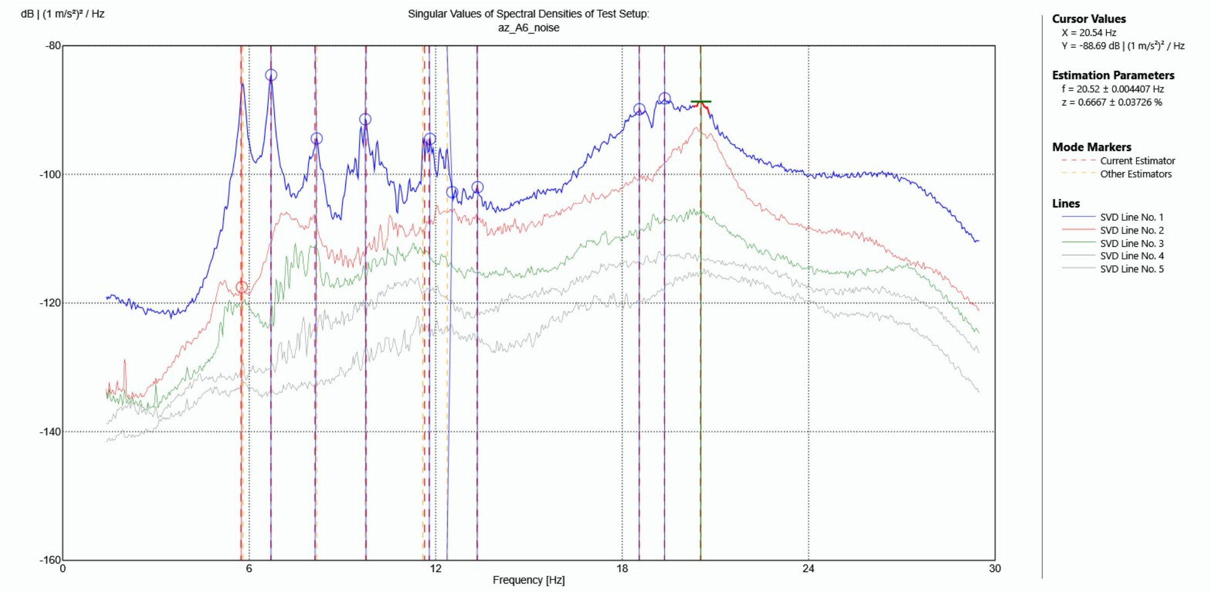

Figure E.18: Singular values of spectral densities [dB rel. to m^2/s^3] as a function of frequency [Hz] for the 1-hour data segment (z-direction) from August 2019 before peak picking of potential modal frequencies for the EFDD.

F Beam-Element Model Modeshapes

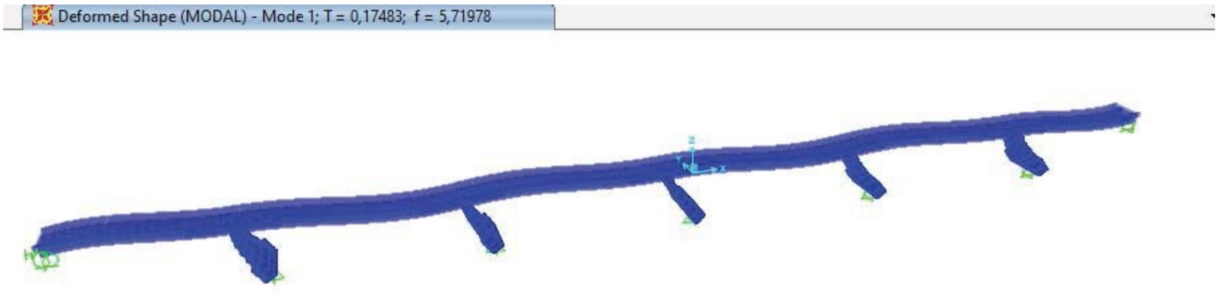
Deformed Shape (MODAL) - Mode 1; T = 0,17483; f = 5,71978

Figure F.1: Modeshape no.1, eigenfrequency 5.72 Hz.

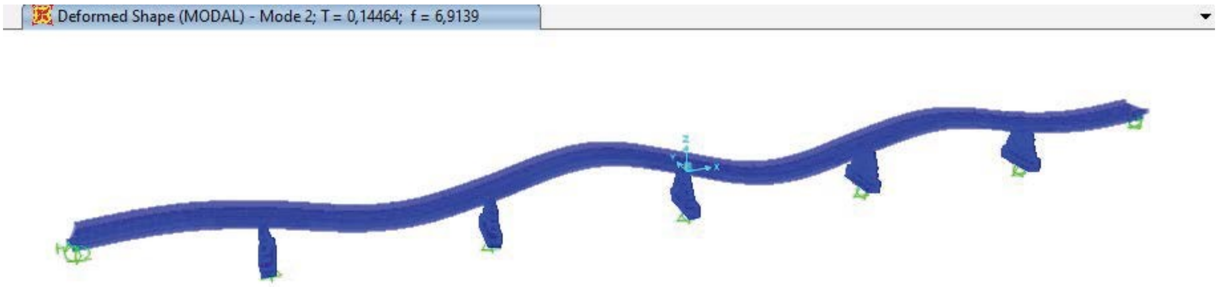
Deformed Shape (MODAL) - Mode 2; T = 0,14464; f = 6,9139

Figure F.2: Modeshape no.2, eigenfrequency 6.91 Hz.

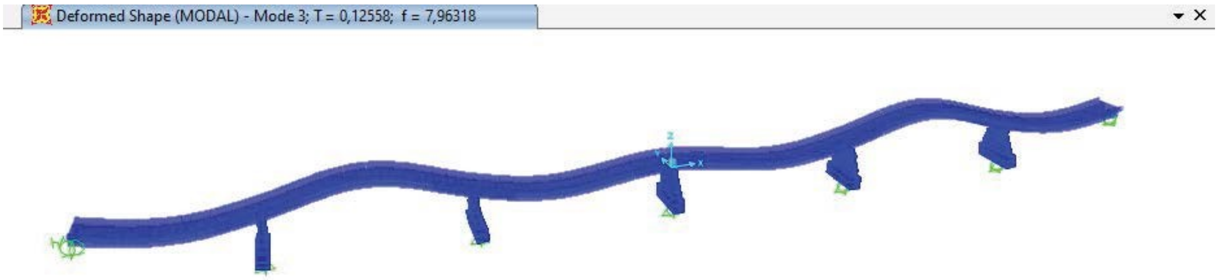
Deformed Shape (MODAL) - Mode 3; T = 0,12558; f = 7,96318

Figure F.3: Modeshape no.3, eigenfrequency 7.96 Hz.

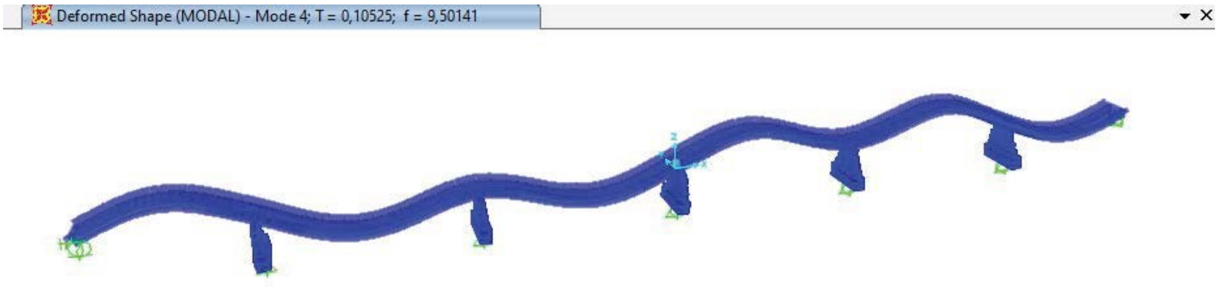

Deformed Shape (MODAL) - Mode 4; T = 0,10525; f = 9,50141

Figure F.4: Modeshape no.4, eigenfrequency 9.50 Hz.

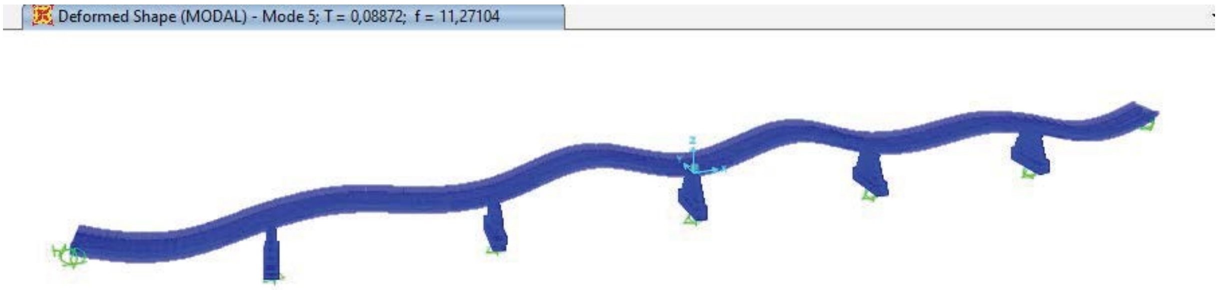

Deformed Shape (MODAL) - Mode 5; T = 0,08872; f = 11,27104

Figure F.5: Modeshape no.5, eigenfrequency 11.27 Hz.

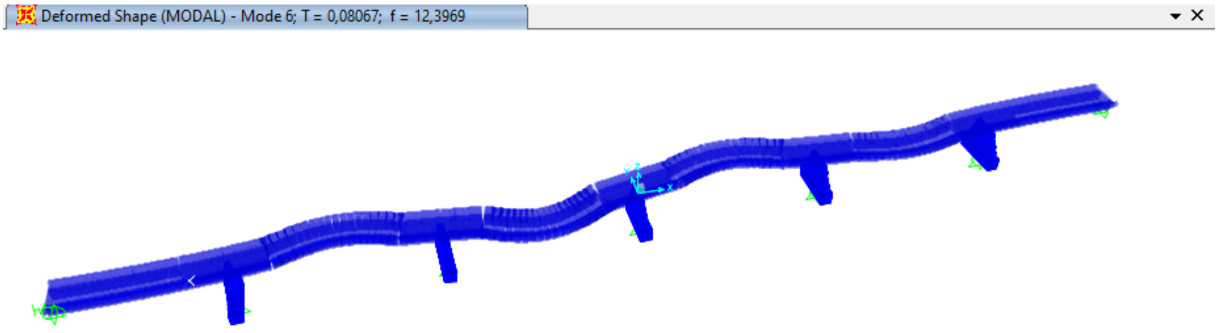

Deformed Shape (MODAL) - Mode 6; T = 0,08067; f = 12,3969

Figure F.6: Modeshape no.6, eigenfrequency 12.39 Hz.

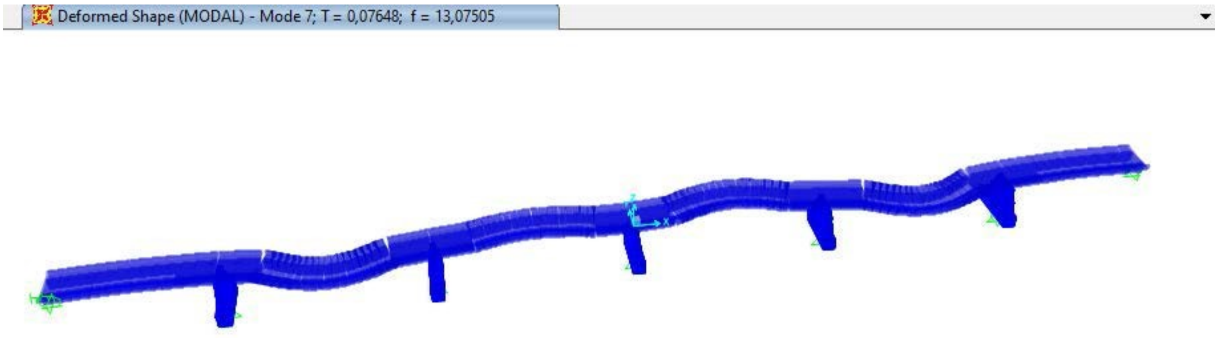

Figure F.7: Modeshape no.7, eigenfrequency 13.08 Hz.

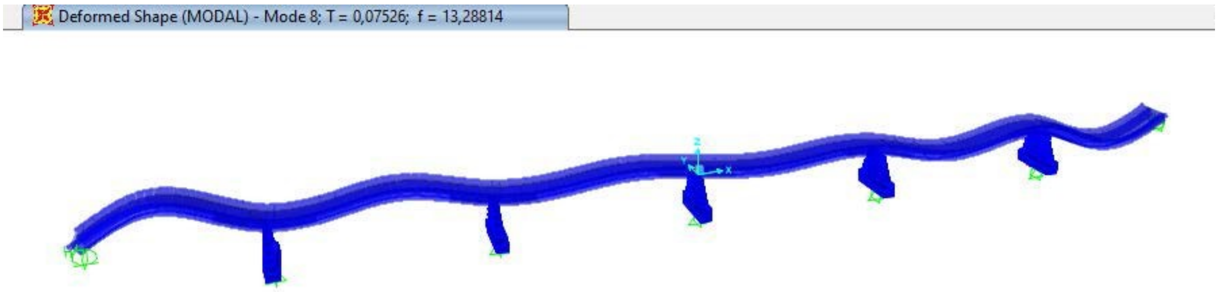

Figure F.8: Modeshape no.8, eigenfrequency 13.29 Hz.

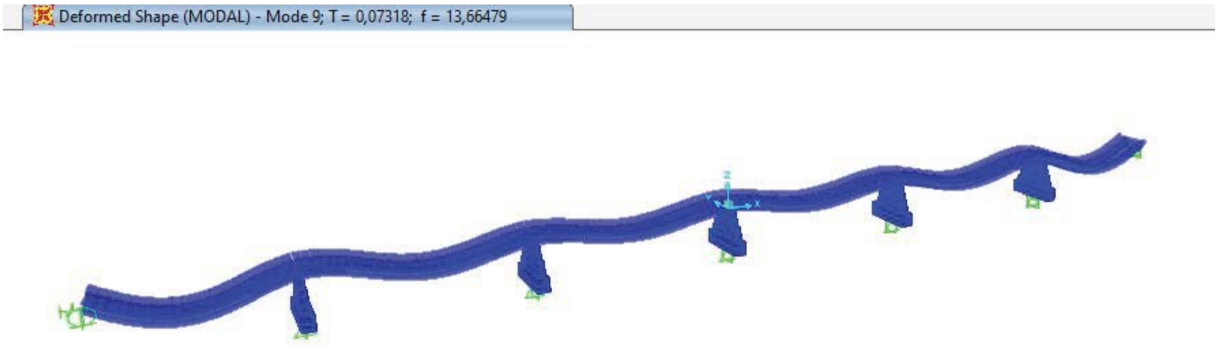

Figure F.9: Modeshape no.9, eigenfrequency 13.66 Hz.

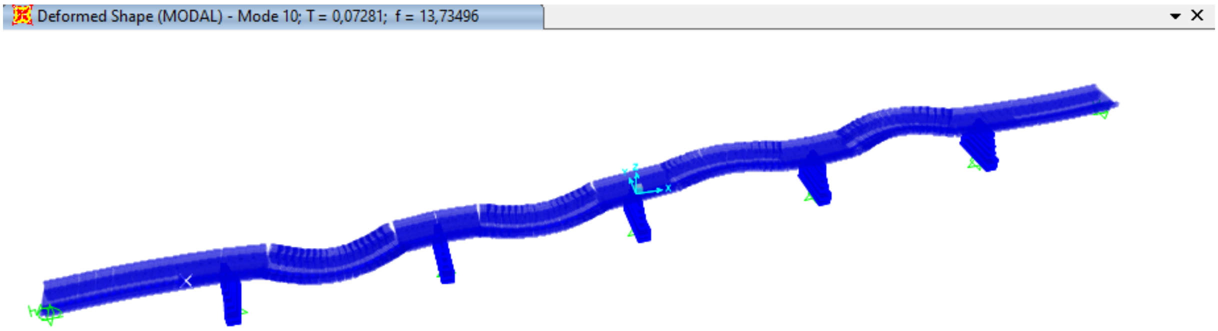

Figure F.10: Modeshape no.10, eigenfrequency 13.75 Hz.

G Shell-Element Model Modeshapes

G.1 Model II with settlement of pillar

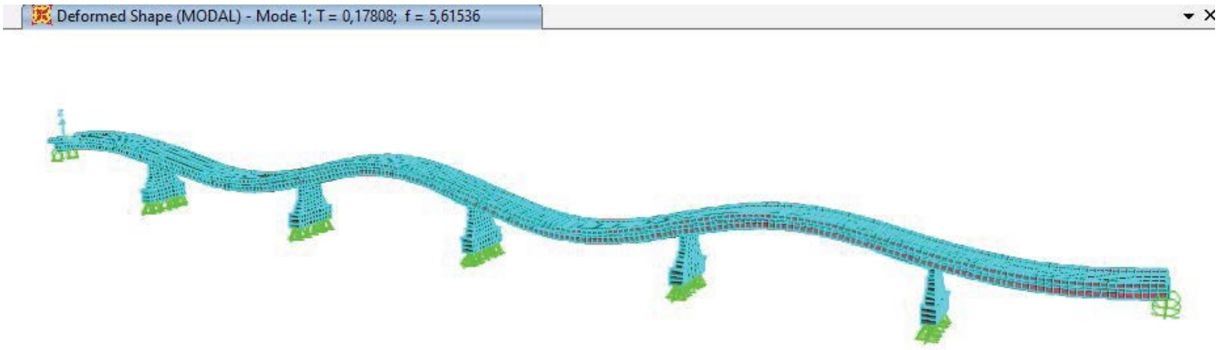

Figure G.1: Modeshape no.1, eigenfrequency 5.62 Hz.

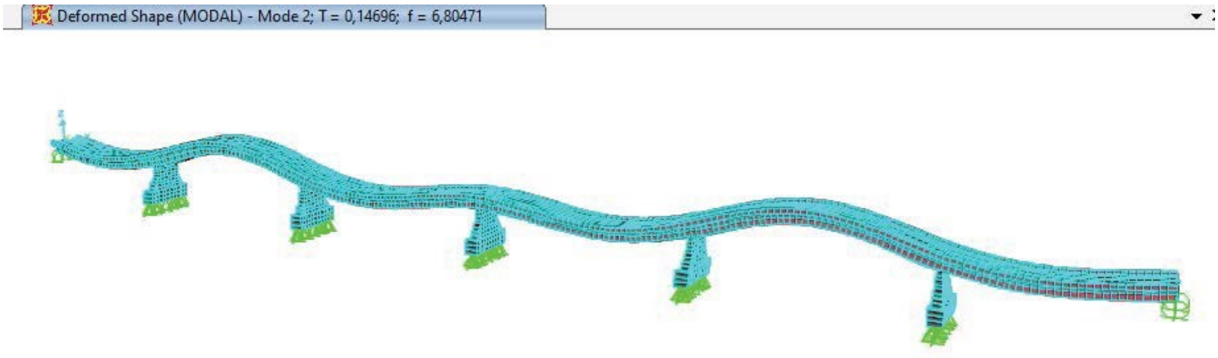

Deformed Shape (MODAL) - Mode 2; T = 0,14696; f = 6,80471

Figure G.2: Modeshape no.2, eigenfrequency 6.80 Hz.

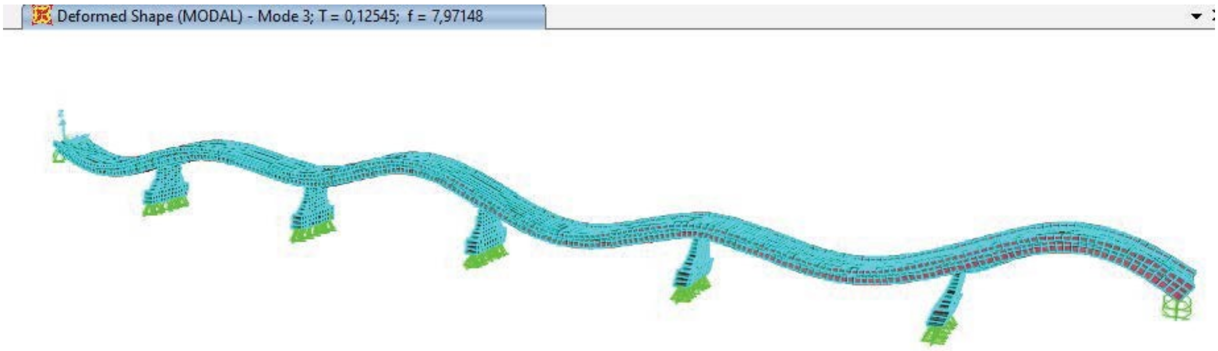

Deformed Shape (MODAL) - Mode 3; T = 0,12545; f = 7,97148

Figure G.3: Modeshape no.3, eigenfrequency 7.97 Hz.

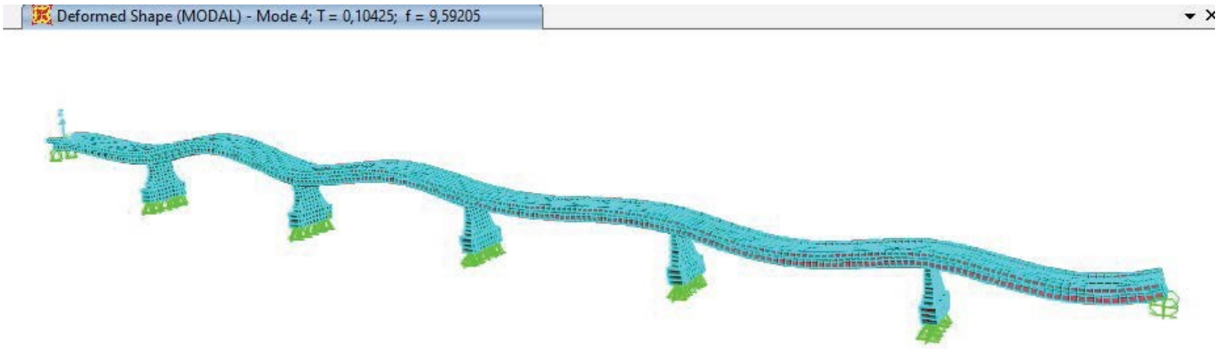

Deformed Shape (MODAL) - Mode 4; T = 0,10425; f = 9,59205

Figure G.4: Modeshape no.4, eigenfrequency 9.59 Hz.

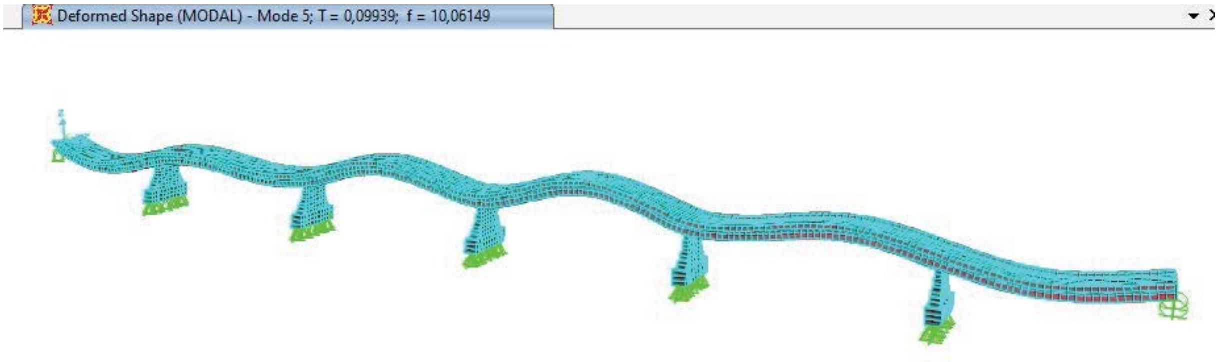

Deformed Shape (MODAL) - Mode 5; T = 0,09939; f = 10,06149

Figure G.5: Modeshape no.5, eigenfrequency 10.6 Hz.

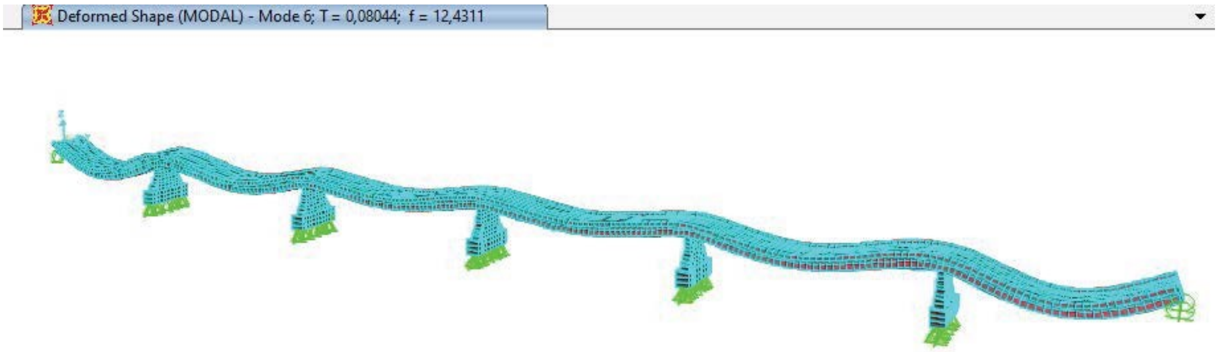

Deformed Shape (MODAL) - Mode 6; T = 0,08044; f = 12,4311

Figure G.6: Modeshape no.6, eigenfrequency 12.43 Hz.

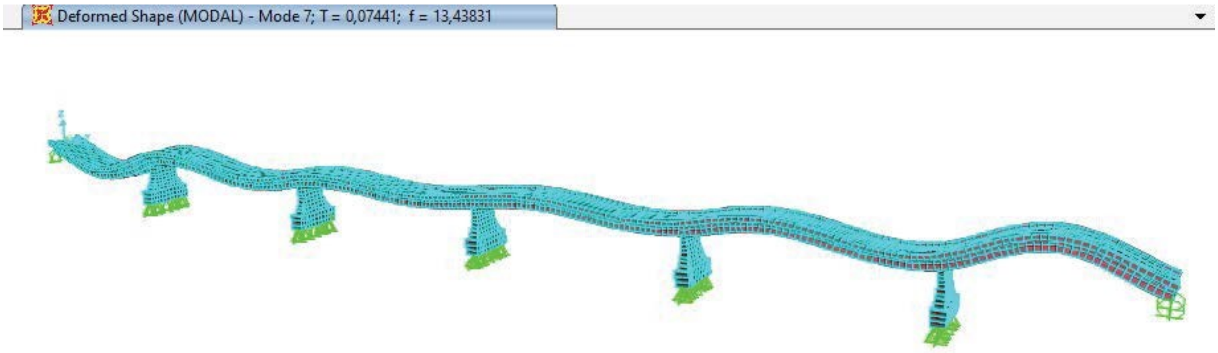

Deformed Shape (MODAL) - Mode 7; T = 0,07441; f = 13,43831

Figure G.7: Modeshape no.7, eigenfrequency 13.44 Hz.

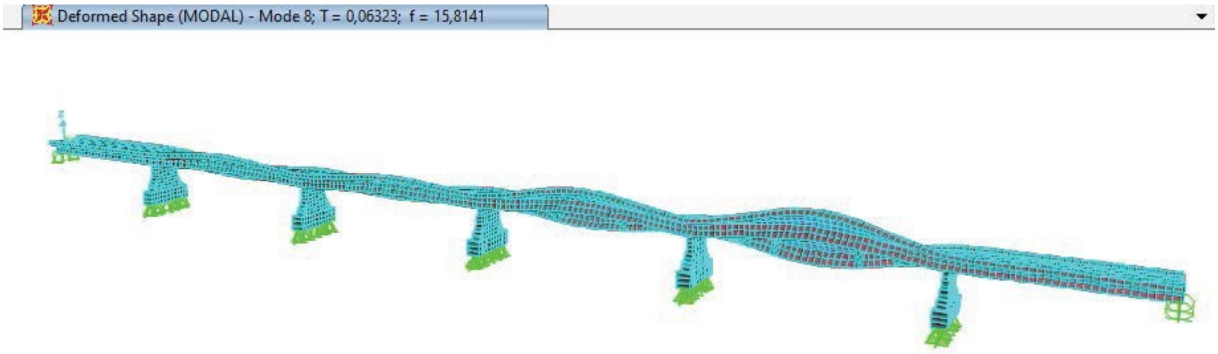

Deformed Shape (MODAL) - Mode 8; T = 0,06323; f = 15,8141

Figure G.8: Modeshape no.8, eigenfrequency 15.81 Hz.

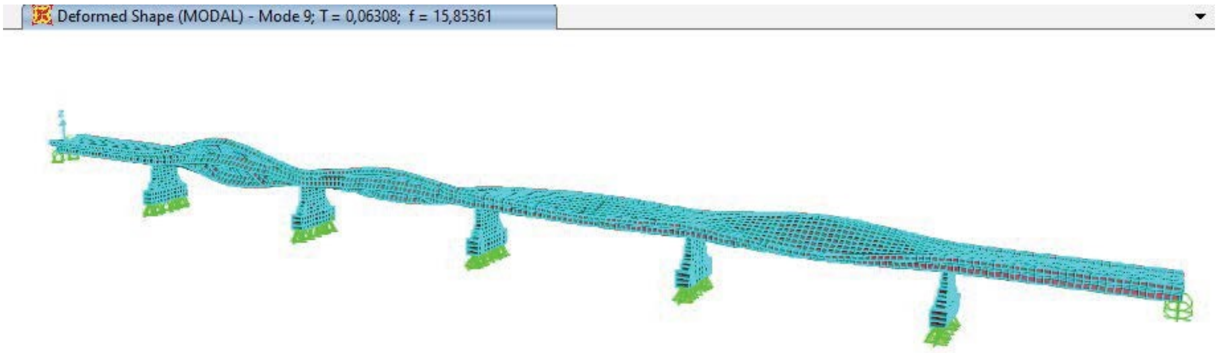

Deformed Shape (MODAL) - Mode 9; T = 0,06308; f = 15,85361

Figure G.9: Modeshape no.9, eigenfrequency 15.85 Hz.

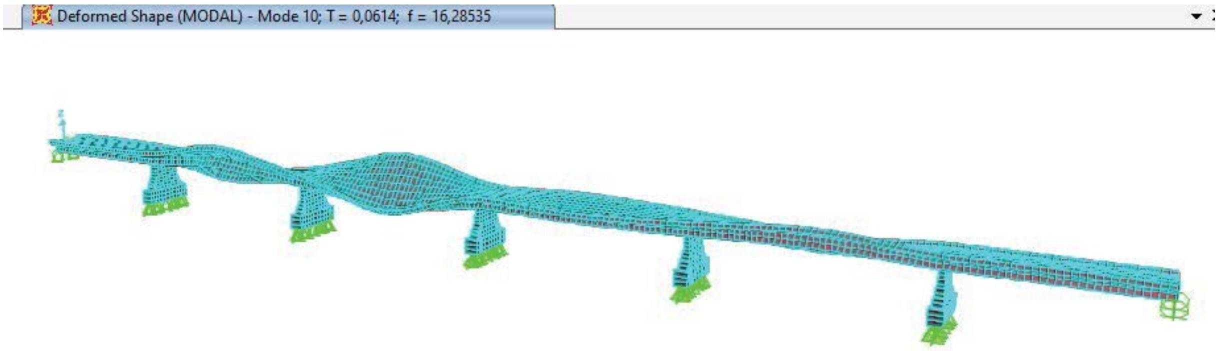

Deformed Shape (MODAL) - Mode 10; T = 0,0614; f = 16,28535

Figure G.10: Modeshape no.10, eigenfrequency 16.29 Hz.

G.2 Model II without settlement of pillar

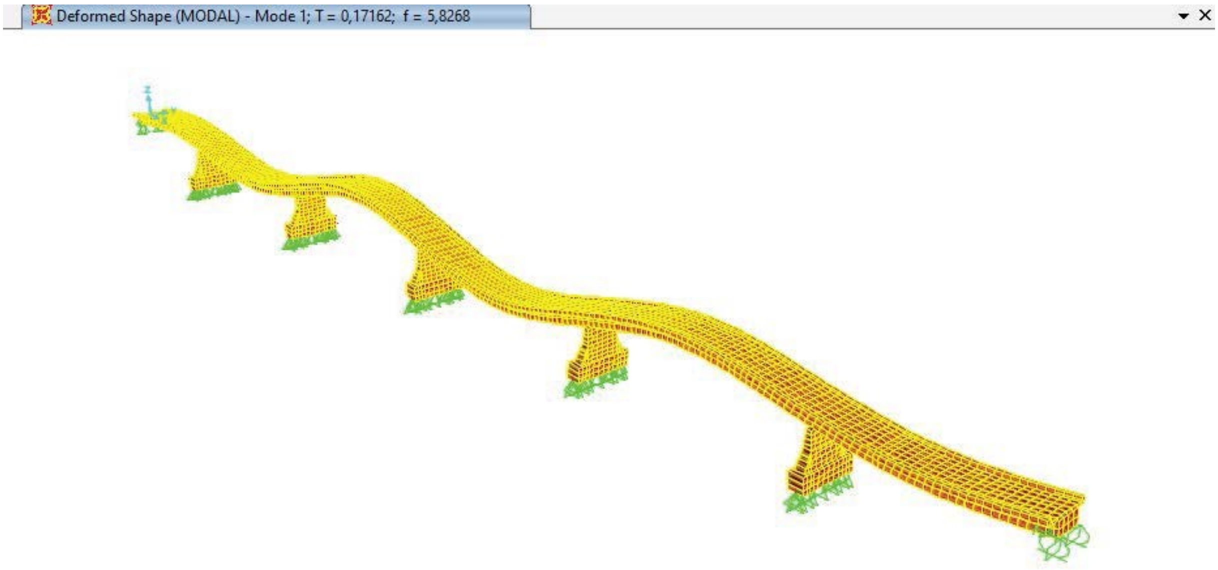

Deformed Shape (MODAL) - Mode 1; T = 0,17162; f = 5,8268

Figure G.11: Modeshape no.1, eigenfrequency 5.83 Hz.

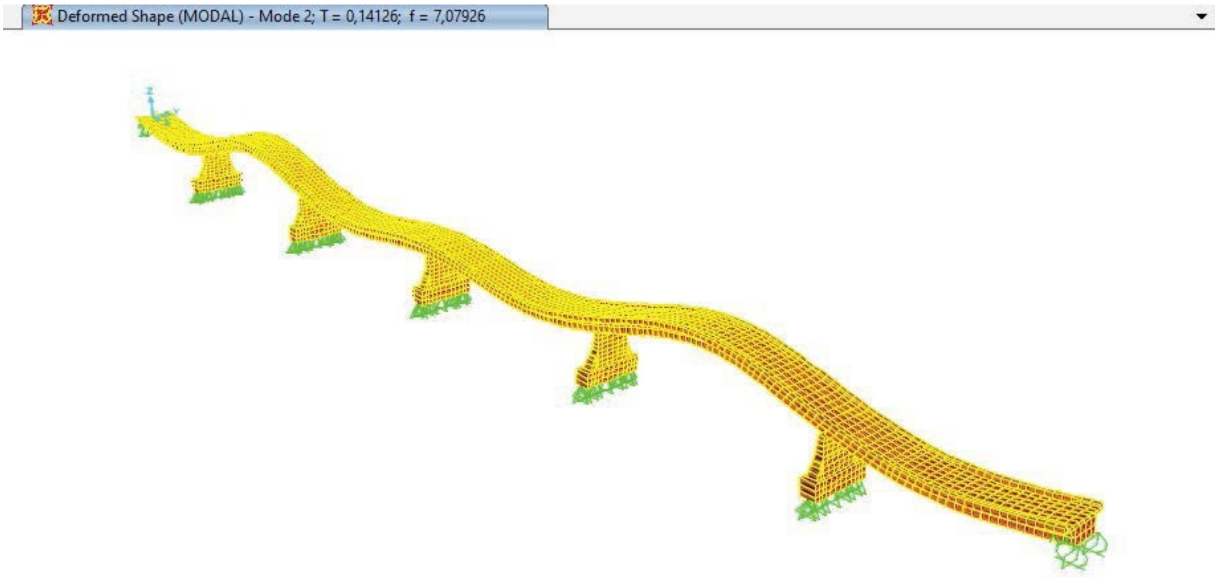

Deformed Shape (MODAL) - Mode 2; T = 0,14126; f = 7,07926

Figure G.12: Modeshape no.2, eigenfrequency 7.08 Hz.

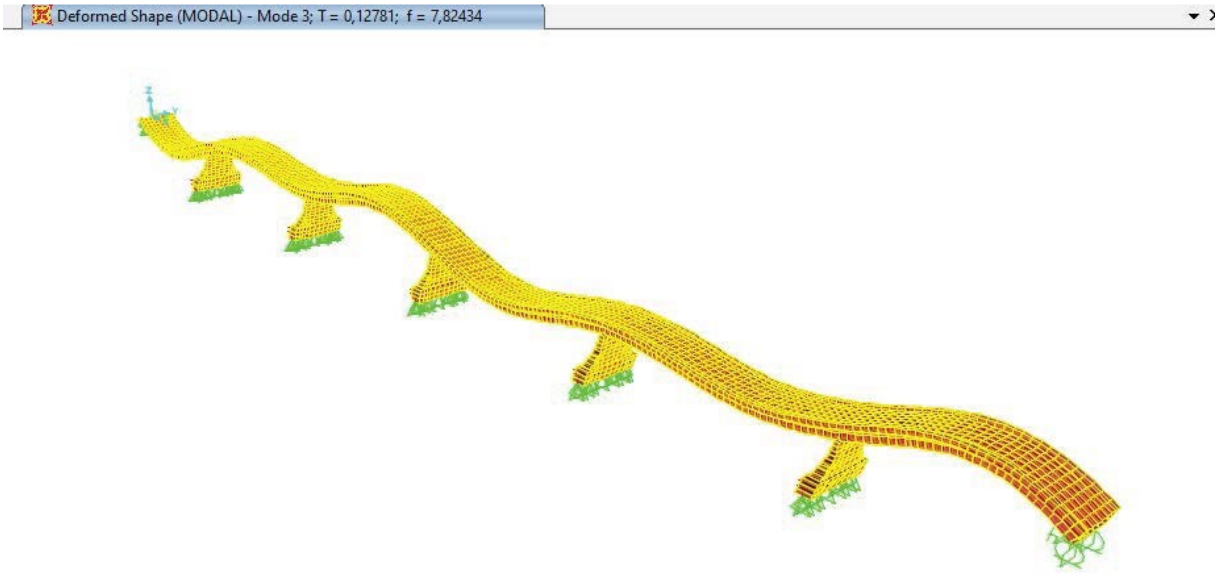

Figure G.13: Modeshape no.3, eigenfrequency 7.82 Hz.

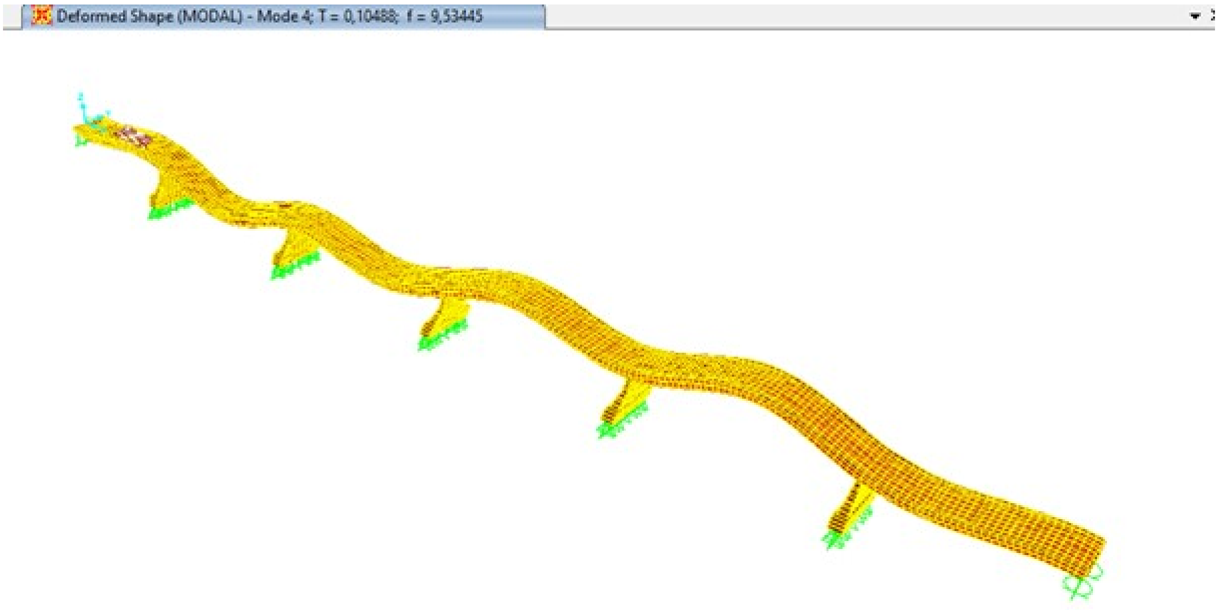

Figure G.14: Modeshape no.4, eigenfrequency 9.53 Hz.

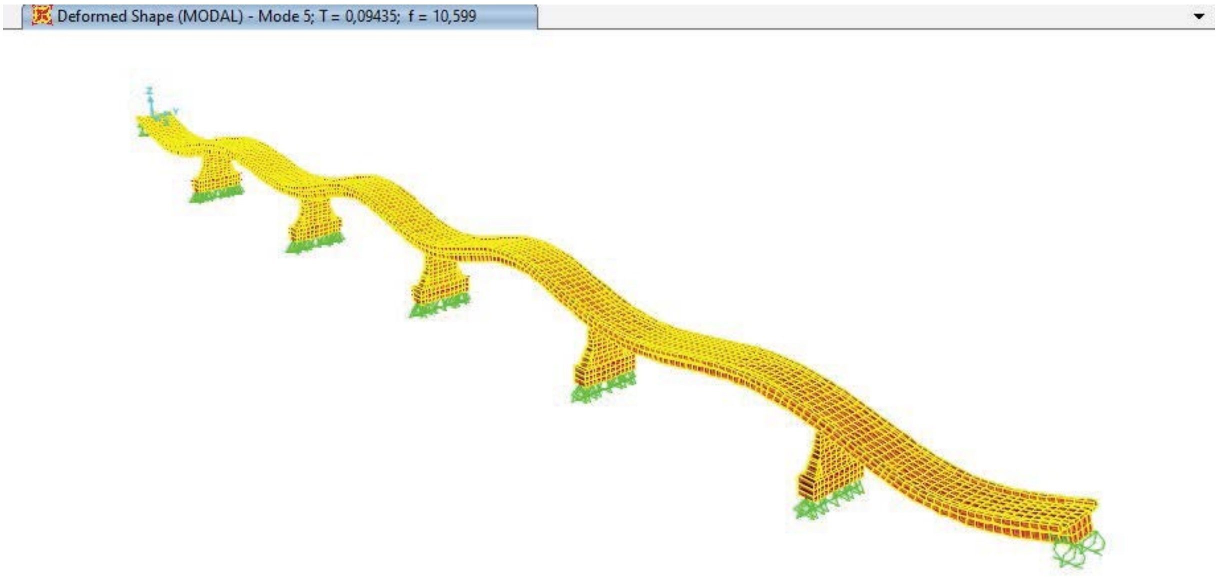

Figure G.15: Modeshape no.5, eigenfrequency 10.60 Hz.

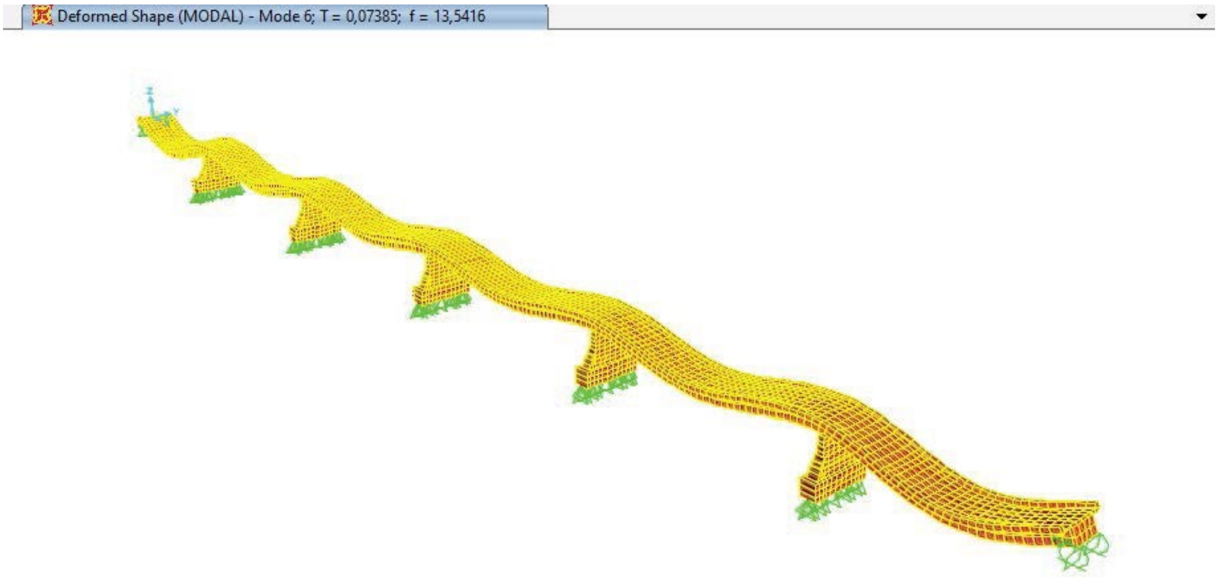

Figure G.16: Modeshape no.6, eigenfrequency 13.54 Hz.

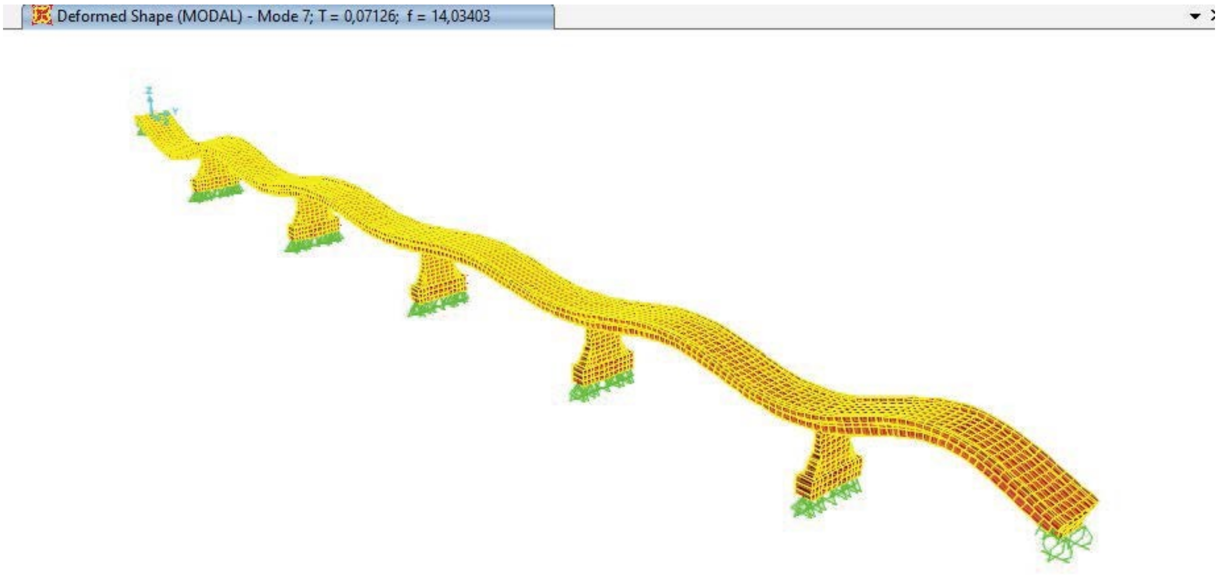

Deformed Shape (MODAL) - Mode 7; T = 0,07126; f = 14,03403

Figure G.17: Modeshape no.7, eigenfrequency 14.03 Hz.

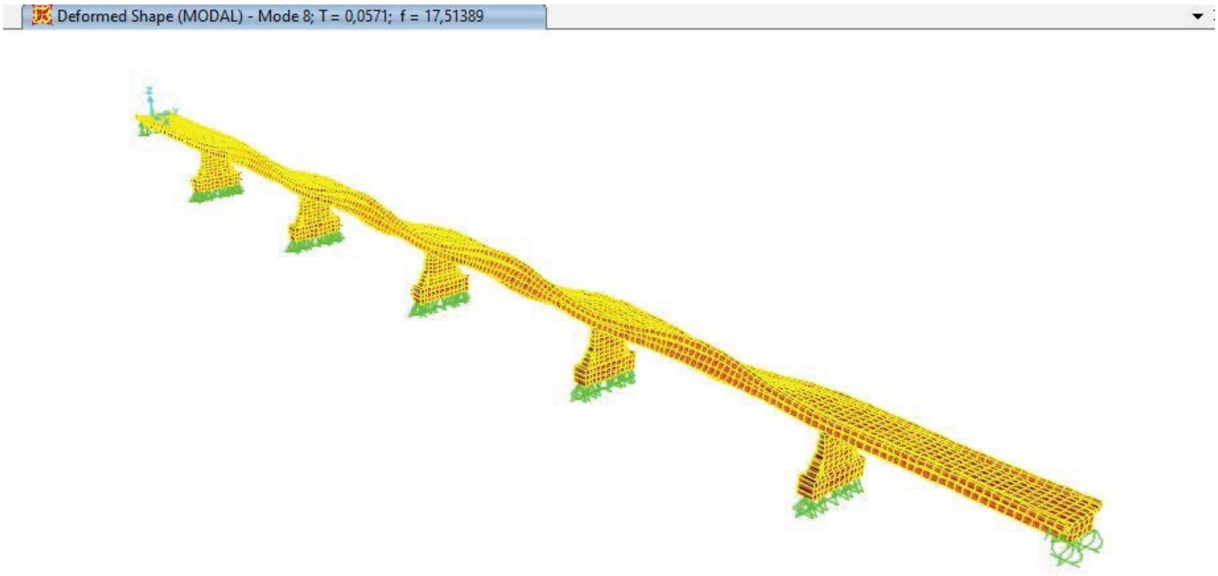

Deformed Shape (MODAL) - Mode 8; T = 0,0571; f = 17,51389

Figure G.18: Modeshape no.8, eigenfrequency 17.51 Hz.

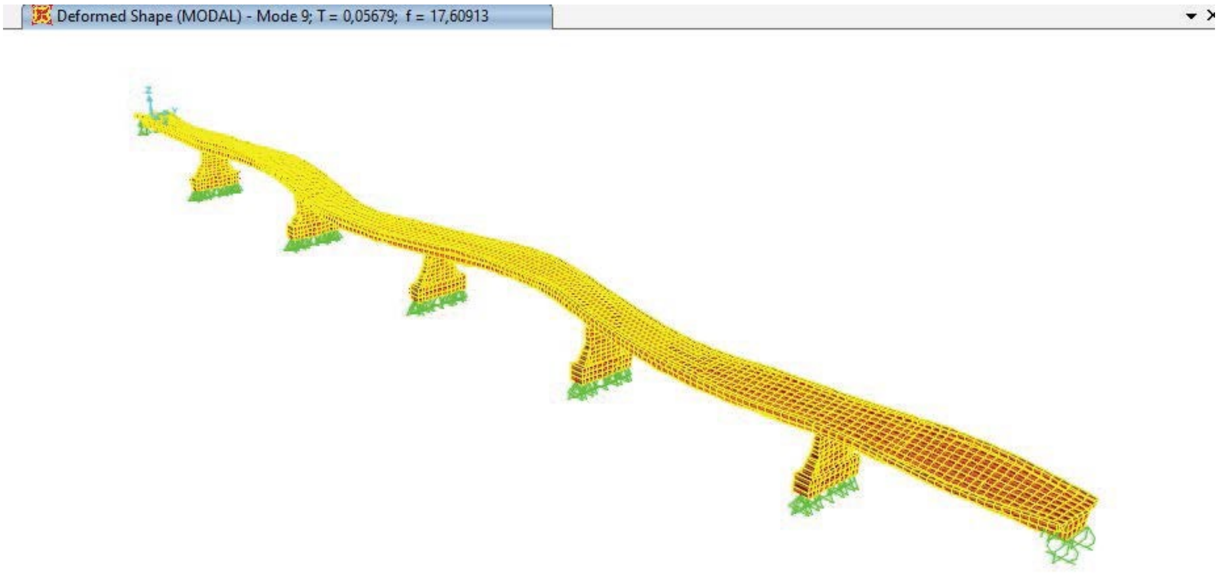

Figure G.19: Modeshape no.9, eigenfrequency 17.61 Hz.

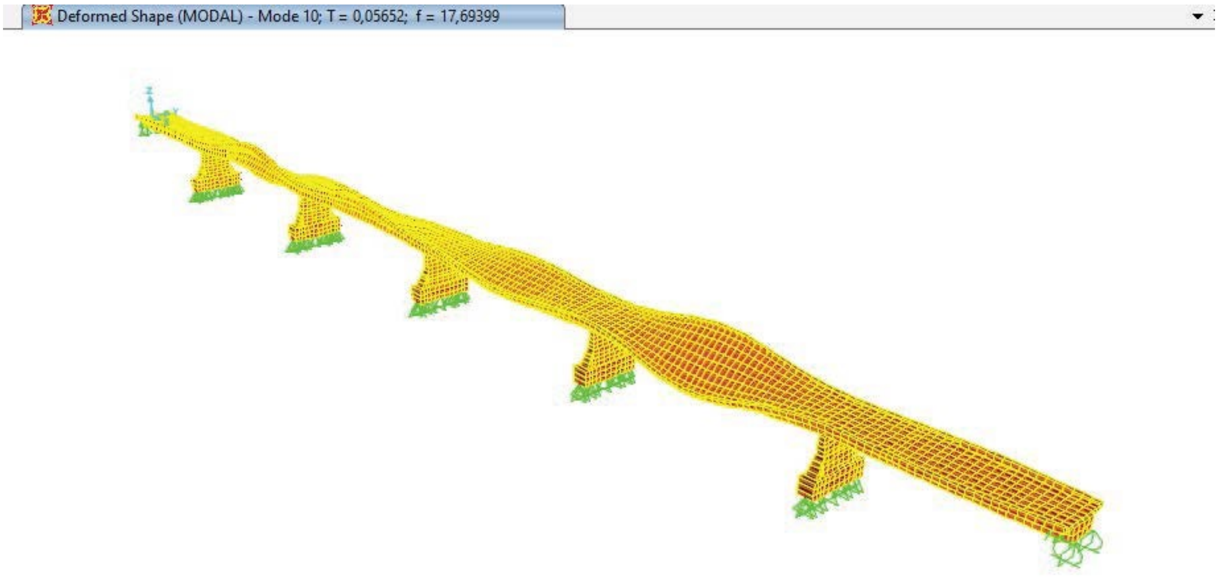

Figure G.20: Modeshape no.10, eigenfrequency 17.69 Hz.

H Results from analysis of static load cases

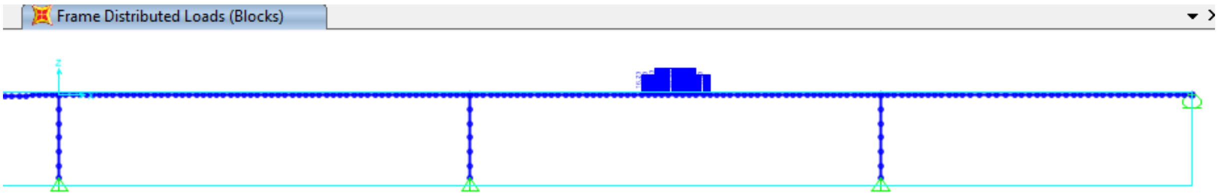

(a) Static loading of six concrete blocks.

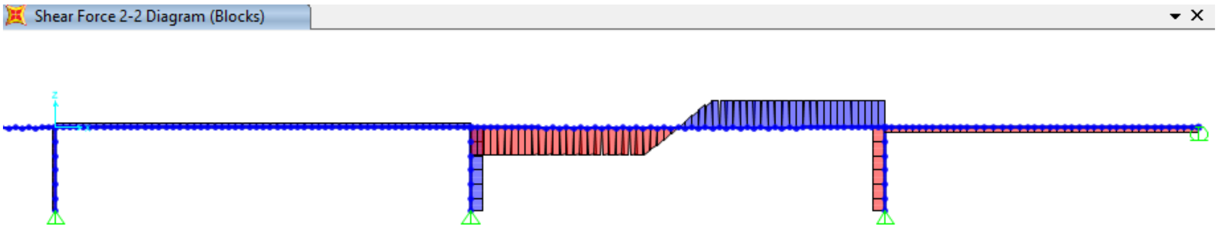

(b) Shear force distribution with V_{max} = 31 kN

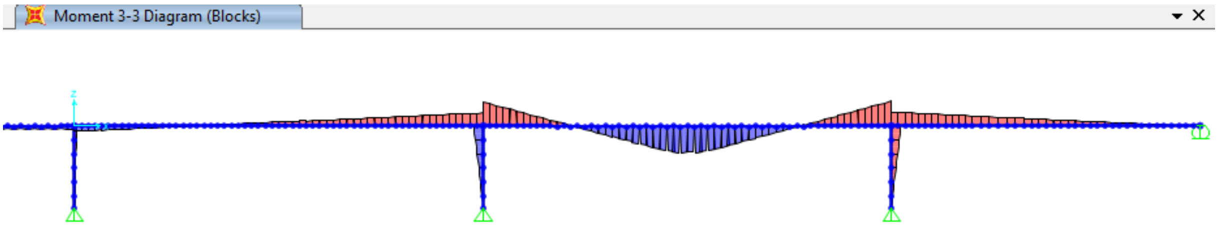

(c) Moment distribution with M_{center} = 121 kNm and maximum bending stress of 0.8 MPa.

Figure H.1: Diagrams from static load analysis for the 6 concrete blocks.

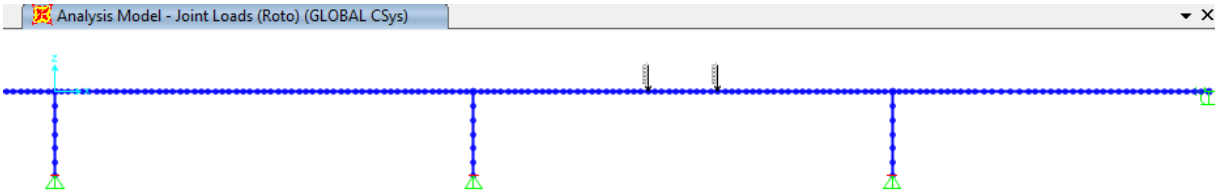

(a) Static loading of a Roto Truck.

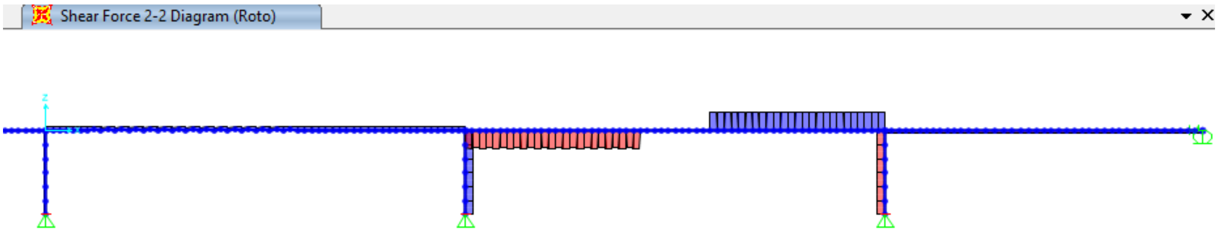

(b) Shear force distribution with V_{max} = 80 kN.

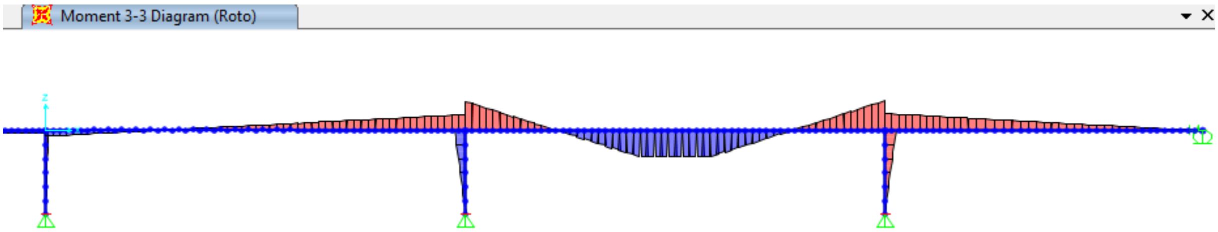

(c) Moment distribution with M_{center} = 291 kNm and maximum bending stress of 2 MPa.

Figure H.2: Diagrams from static load analysis for the Roto Merlo truck.

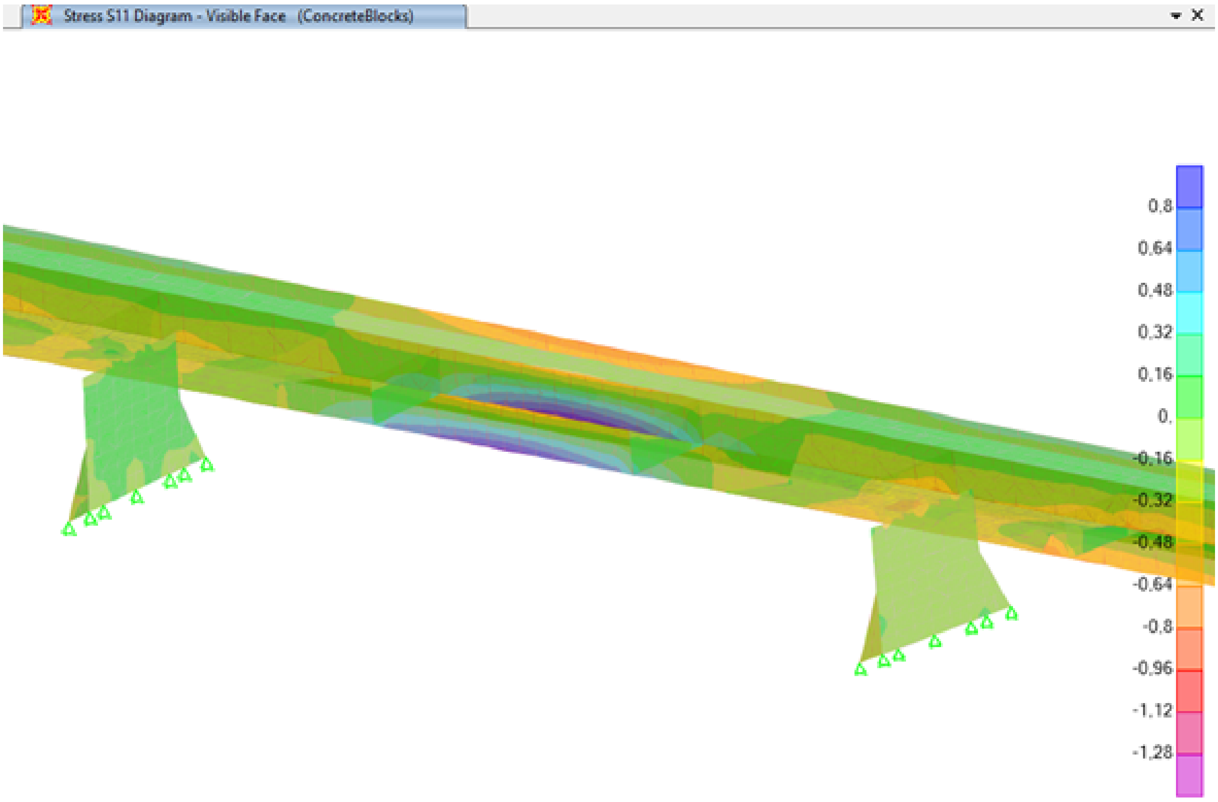

(a) The 6 tonn Concrete blocks.

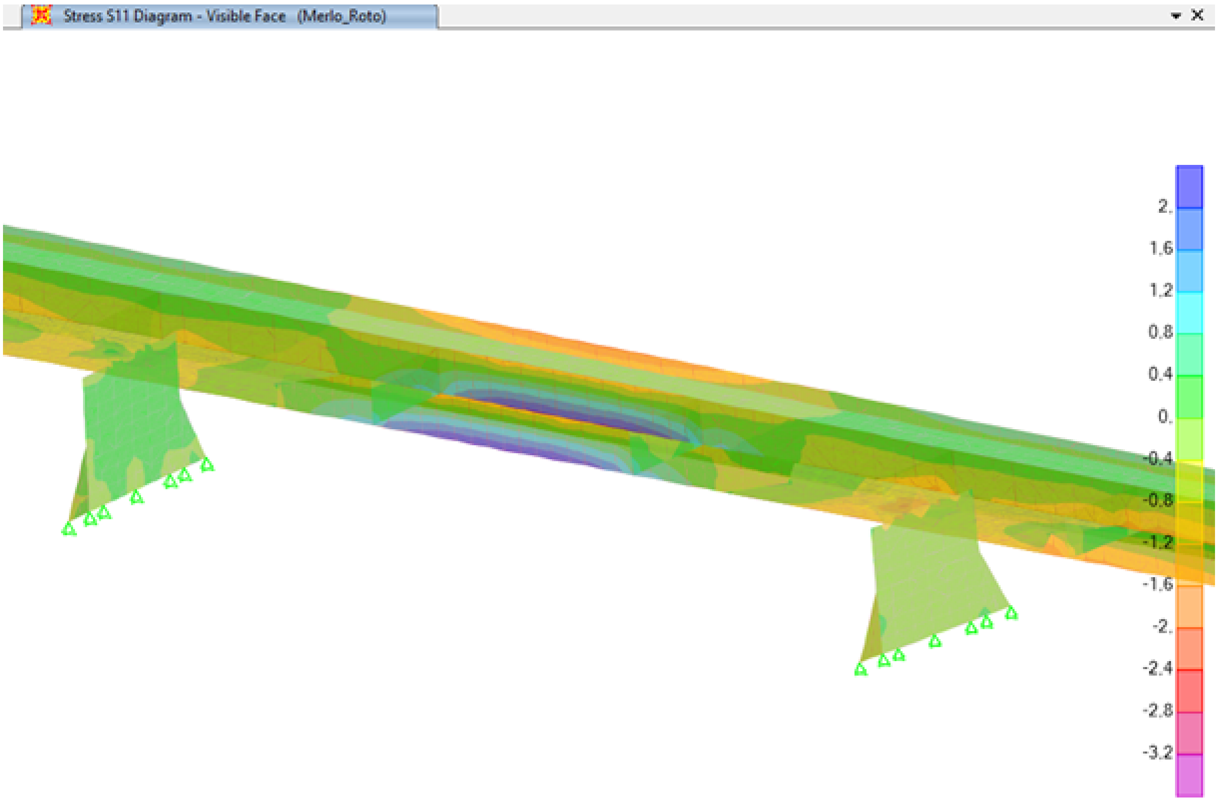

(b) The 16 tonn Merlo Roto truck.

Figure H.3: Plot of the bending stresses (S11) from the shell model for the two static load cases. The units of the stress is MPa.

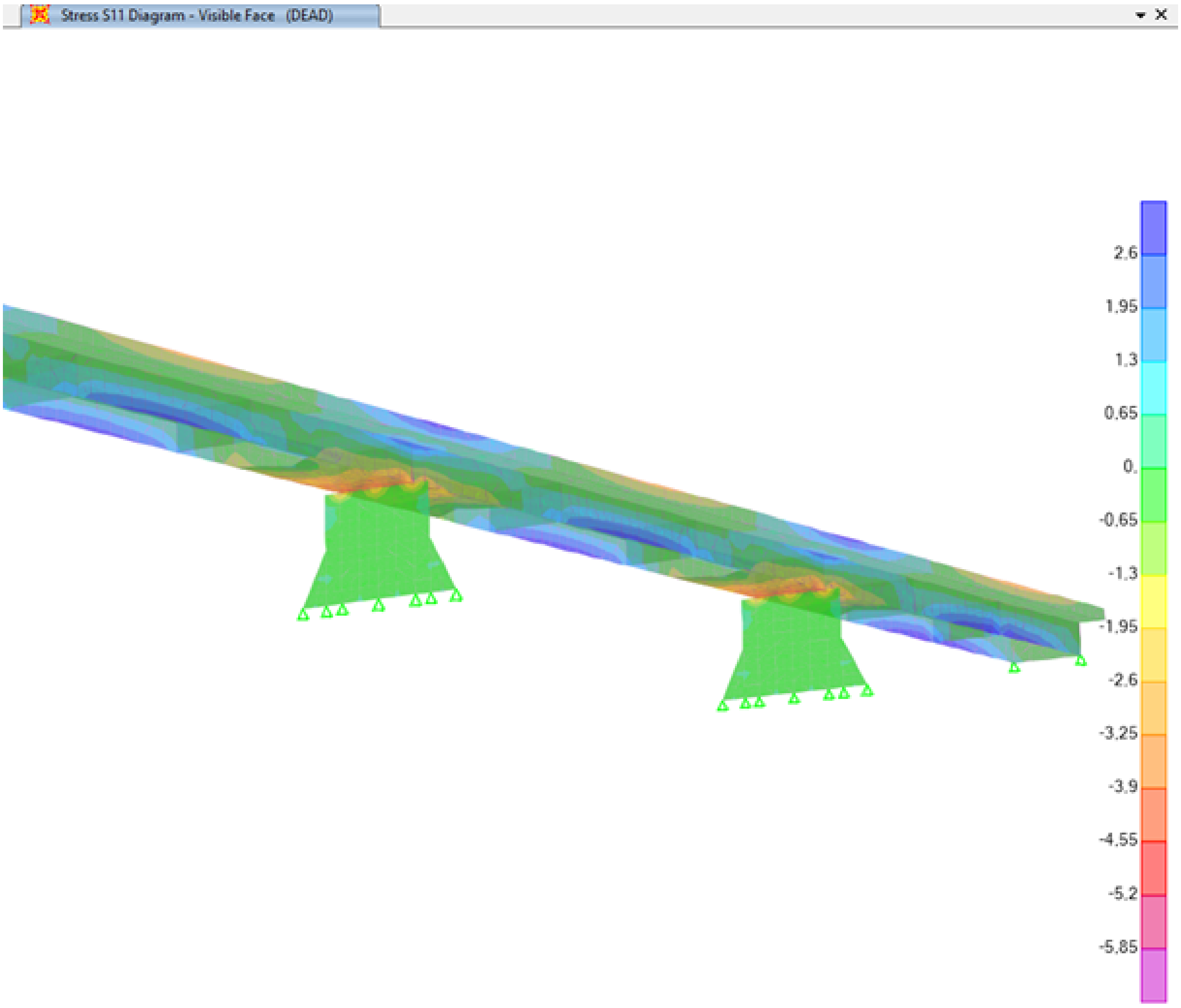

Figure H.4: Plot of the bending stress (S11) distribution in the Shell-element model due to the dead-weight of the bridge. The stress is in units of MPa.